Cation Diffusion and Related Degradation Phenomena in $La_2NiO_{4+\delta}$ for Oxygen Separation Membranes

Nebojša Čebašek

Dissertation for the Degree of Philosophiae Doctor

Department of Chemistry

Faculty of Mathematics and Natural Sciences

University of Oslo

Group for Solid-State Electrochemistry (FASE)
Functional Energy Related Materials in Oslo (FERMiO)
Centre for Materials Science and Nanotechnology (SMN)

2012

Series of dissertations submitted to the
Faculty of Mathematics and Natural Sciences, University of Oslo
No. 1192

ISSN 1501-7710

Cover: Inger Sandved Anfinsen.
Printed in Norway: AIT Oslo AS.

Produced in co-operation with Unipub.
The thesis is produced by Unipub merely in connection with the
thesis defence. Kindly direct all inquiries regarding the thesis to the copyright
holder or the unit which grants the doctorate.

Preface

This thesis is the result of practical work for the degree of Doctor of Philosophy (Philosophiae Doctor, PhD) at the Department of Chemistry (KI), Faculty of Mathematics and Natural Sciences, University of Oslo (UiO) in Oslo, Norway. The work was performed within the top-tier initiative Functional Energy Related Materials in Oslo (FERMiO), which is part of the Centre for Materials Science and Nanotechnology (SMN). The scholarship for this PhD degree was funded under the project "162316 Demonstration of AZEP Reactor Module" by the Research Council of Norway (RCN) and Statoil during the period from January 2007 to June 2011 and under the supervision of Professor Truls Norby and Associate Professor Reidar Haugsrud.

First of all I would like to express my gratitude and appreciation to my supervisor Professor Truls Norby for excellent guidance, understanding and encouragement during the most critical moments of my work and my stay here in Norway. I would also like to thank my co-supervisor Associate Professor Reidar Haugsrud for invaluable suggestions and contributions to my work. After spending some great years as a member of this group, I can only say that I am honoured to know you both.

I would like to express particular gratitude to my office-mate Dr. Zuoan Li – firstly, for his continuing support and for believing in me. I know I was impossible sometimes, so thank you very much for your patience – your support meant a lot. Thank you also for all your scientific advices and proof-readings. It has been a tremendous pleasure sharing office space with you all these years.

I am also deeply grateful to my friend Dr. Jovan Milošević for all his help and support, particularly in the early days of my work, and for fruitful discussions not only about science.

I wish to give special thanks to Ingvild Lorentzen from NorECs Norwegian Electro Ceramics AS, for providing me with the opportunity to work and learn more in the most crucial period of my stay in Norway. Thank you very much for understanding.

I would also like to thank Dr. Jens Bragdø Smith from Statoil for his support and interest in my work.

Furthermore, I am deeply thankful to Muriel Marie Laure Erambert at the Department of Geosciences, UiO for her help with Electron Probe Micro Analysis; Dr. Lasse Vines at the MiNa-Lab, Physics institute, UiO for help with Secondary Ion Mass Spectrometry analysis; Dr. Anna Magrasó, FERMiO, SMN, UiO for her help with Electron Backscattered Diffraction; and to Martin F. Sunding at Structural Physics group, FERMiO, SMN, UiO for help with X-ray photoelectron spectroscopy. I am also thankful to my colleagues from the Solid State Electrochemistry group at FERMiO, UiO for their help and advices during experimental work.

I also wish to thank all my friends, here and in Serbia, for giving me support, particularly over the last several months. Thank you all for listening to me.

I acknowledge the Research Council of Norway (RCN) and Statoil for the financial support.

Last, but not least, I want to express my eternal gratitude to my parents and my brother for giving me strength and support, not only during the work on my PhD thesis, but throughout my education. Without you I would not have been able to come this far in all aspects of my life. Your love and care has provided motivation and inspiration for everything I have done, and so I dedicate this thesis to you.

Nebojša Čebašek

Oslo, April 2012

Table of contents

Summary

Oxides with layered perovskite-like K_2NiF_4-type structure have attracted significant attention since the discovery of high temperature superconductivity in $La_2CuO_{4+\delta}$ based systems. Further investigation of this type of oxides has shown that their mixed ion and electron conductivity makes them interesting candidates for high temperature applications, such as cathode material for Solid Oxide Fuel Cells (SOFCs) or as membrane material for gas separation. Besides their electrical features, these oxide materials have to have other suitable characteristics, such as thermal expansion, chemical stability, etc. Furthermore, when these materials are exposed to harsh working conditions, i.e., high temperature and large oxygen potential gradient, it induces cation transport towards the side with higher partial pressure of oxygen (pO_2) which has significant influence on the lifetime of the material. Cation diffusion may cause kinetic demixing and kinetic decomposition due to the different diffusivities of different cations, and morphological instability (membrane walk-out) due to the high diffusivities of the cations. The main topic of this thesis is the determination of the cation diffusion and degradation phenomena in oxides with K_2NiF_4-type structure (general formula A_2BO_4), notably lanthanum nickelate, $La_2NiO_{4+\delta}$ (LNO).

Structure and transport properties of the undoped and doped LNO have been the subject of extensive research. Although cation diffusion is one of the properties of fundamental interest for the durability of components serving under chemical potential gradients, data on cation transport and degradation processes is generally scarce, particularly for materials with K_2NiF_4-type structure. To date there is no data reported on cation diffusion in LNO-based systems.

This thesis comprises studies of A- and B-site cation diffusion in the LNO system, utilising inter-diffusion, chemical tracer diffusion and solid state reaction (SSR) methods. The study of the degradation of the LNO membrane under the gradient of pO_2 is also included in this

work. Diffusion couples between $La_2NiO_{4+\delta}$ and $Nd_2NiO_{4+\delta}$ and between $La_2NiO_{4+\delta}$ and $La_2CuO_{4+\delta}$ were used in the inter-diffusion method for the estimation of A- and B-site inter-diffusion coefficients, respectively. The chemical tracer diffusion method employed Pr, Nd and Co as impurity tracers for the study of A- and B-site cation diffusion, respectively. The self-diffusion coefficient of the fastest moving cation was determined by SSR between the binary oxides NiO and La_2O_3. The samples were analysed extensively using Scanning Electron Microscopy (SEM) and its additional features (Energy-dispersive X-ray spectroscopy (EDX) and Electron backscatter diffraction (EBSD)). Secondary Ion Mass Spectrometry (SIMS), Electron Probe Micro Analysis (EPMA), X-ray Diffraction (XRD) and X-ray Photoelectron Spectroscopy (XPS) were the methods of instrumental analysis used in this work.

The inter-diffusion experiment showed that the A-site cation diffuses mainly through bulk, while the B-site cation is faster due to enhanced grain boundary diffusion. The diffusion paths of the A- and B-site cations were visualised by EPMA element mapping of the cross-section of the diffusion couples. The obtained activation energies for diffusion are 275 ±12 kJ/mol for the A-site cation (La) bulk, 450 ±20 kJ/mol for the B-site cation (Ni) bulk, and 125 ±24 kJ/mol for the grain boundary.

The chemical tracer experiment revealed kinetics of diffusion of the Pr, Nd and Co chemical (impurity) tracers in LNO. By means of analyses of the SIMS data it is shown that the A-site cation (Pr and Nd) diffuses mainly through bulk, meaning that according to Harrison's classification of diffusion kinetics it belongs to the "A"-type, and that the B-site cation (Co) has enhanced diffusion along grain boundaries and exhibits "B"-type diffusion kinetics. The average apparent activation energies for the diffusion of chemical (impurity) tracers are evaluated as 165±15 kJ/mol for Pr and Nd in bulk, 295±15 kJ/mol for Co in bulk, and 380 ±20 kJ/mol for Co in grain boundaries. The unexpectedly high activation energy of the fast Co grain boundary diffusion in comparison to bulk is also discussed.

Through the use of inert platinum markers, the SSR confirmed that the fastest moving cation in LNO is Ni. The growth of the reaction layer between NiO and La_2O_3 was parabolic, as given by Wagner's parabolic rate law. The obtained self-diffusion coefficient of Ni shows Arrhenius behaviour at higher experimental temperatures (1100-1450 °C), with activation energy of 243 ±21 kJ/mol. At lower experimental temperatures (950-1100 °C) the self-diffusion coefficient deviates from Arrhenius behaviour by bending downward

and attaining apparently higher activation energies. Some suggestions for this rather unusual behaviour are given in this thesis. In addition, the measurement shows that the Ni self-diffusion coefficient at the higher temperatures is independent of the surrounding pO_2, indicating that the thin product layer formed between the NiO and La_2O_3 reactants cannot equilibrate fast enough with the surrounding atmosphere at these temperatures.

When an LNO membrane was exposed to a gradient in pO_2 for 800 h at 1000 °C, the high pO_2 side of the membrane became decorated by precipitations of NiO. This was expected because the results from the inter-diffusion, chemical tracer and SSR experiments had shown that the B-site cation (Ni) exhibited enhanced diffusion over the A-site cation (La). This decomposition experiment also showed signs of "walk-out" toward the side with higher pO_2. At the membrane's low pO_2 side porosity and etched-away structure developed, reflecting the loss of material from this side of the membrane.

The different data for cation diffusion in LNO obtained by the above mentioned methods agrees, showing similar cation diffusion within anticipated uncertainties. Anyhow, LNO exhibits rather high diffusion values for both A- and B-site cations, even when compared with the data for cation diffusion of related perovskite compounds. It is demonstrated here that long-term utilisation in a gradient of pO_2 can severely degrade and perhaps eventually break the membrane due to "walk-out" and decomposition.

1. Introduction

1.1 Project background

Oxygen is one of the most abundant elements on Earth and the second largest constituent of air (air = approximately 78% of nitrogen, 21% of oxygen and 0.9% of argon). Besides its essential importance for life in general, it is of extraordinary importance for technological applications. A rough estimate of oxygen utilisation is given in Figure 1.1. As it is obvious from the chart, the largest amount of oxygen is used in the metallurgical industry, particularly in the steel industry for the removal of impurities. Among its remaining applications it is important to mention its utilisation in medicine, e.g. in the treatment of certain chronic pulmonary diseases, in hyperbaric chambers, etc. The increasing consumption of energy generates great demand to search for new energy sources. In this case, oxygen plays an important role as the catalyst for partial oxidation of light hydrocarbons by forming synthesis gas, i.e., through better use of fossil energy sources. “Better” in this respect means more efficient as well as more climate- and environment-friendly. All these processes usually require relatively pure oxygen, 95-99%. To date, the major conventional methods of oxygen production can be classified into two techniques: cryogenic and non-cryogenic. In the cryogenic technique oxygen is obtained by fractional distillation from previously purified, compressed and liquefied air. Using this method oxygen purity can reach 99.9 %. In the non-cryogenic technique oxygen production is based on the removal of nitrogen and other gaseous impurities by pressure swing adsorption (PSA) technologies, relying on the use of molecular sieves (zeolites) with preferential adsorption. Oxygen produced in this way can be >95% pure [1, 2, 3, 4, 5].

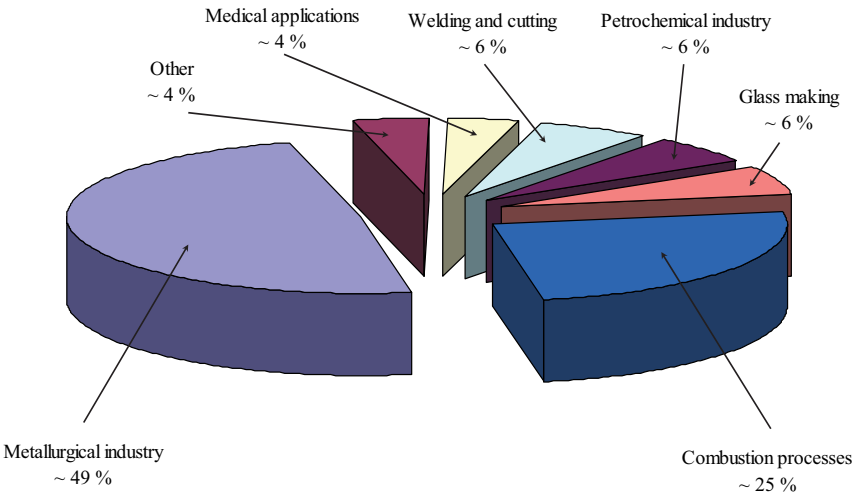

Figure 1.1. Estimated utilisation of oxygen [2].

Newly developed techniques for oxygen production use dense ceramic materials (membranes). The advantage of ceramic membranes is long-term 100% stable selectivity for certain species, in this case oxygen. In addition, these materials can be utilised at high temperatures, under harsh chemical and mechanical conditions. Ceramic membranes can be classified into two categories: pure ionic conducting membranes (IC) and mixed ionic and electron conducting membranes (MIEC). An example of IC membranes is yttrium doped ("stabilised") zirconia (ZrO_2, YSZ) which can also be used as an electrolyte in Solid Oxide Fuel Cells (SOFCs). An example of a MIEC membrane is $La_2NiO_{4+\delta}$ (LNO), which is the focus of this work. Besides their application as a separation membrane, MIEC oxides can also be used as cathodes in SOFCs. Dense oxygen separation membranes rely on the simultaneous transport of ions and electrons, i.e., oxygen ions and electrons. Mobile species are defects in the crystalline lattices of the solids – oxygen vacancies or interstitials, defect electrons and electron holes. It has been suggested that for a ceramic material to be commercially utilised as an oxygen separation membrane, it should have an oxygen flux of around 10 ml cm^{-2} min^{-1} when operated in the temperature range of 800-1000 °C. In addition to the high permeability and preferential selectivity of the material, the key scientific and technological challenge is its long-term stability (up to 100,000 h) [4, 6, 7, 8, 9].

Candidate materials for gas separation membranes have been widely investigated because of their importance in power technologies. The functionality of such membranes in general arises from their ability to separate oxygen from air and hydrogen from reformed fossil fuels. The example in Figure 1.2 shows the process of utilisation of an oxygen separation membrane together with a hydrogen separation membrane in the reactor. The reactor fed by natural gas (methane, CH_4) and air at different sides of the membrane, first oxidises the methane by the oxygen in an oxygen permeable membrane. Further down the reactor, the hydrogen from the oxidised methane is extracted through a hydrogen permeable membrane tube, using the nitrogen left from the first stage as sweep gas. The end products are hydrogen diluted by nitrogen (a suitable fuel for gas turbines and fuel cells) and CO_2. The following example is where the separation of oxygen from air enables the processing – partial oxidation – of natural gas into synthesis gas ($CO + H_2$) without introducing nitrogen from air into the product. This increases the value of synthesis gas for e.g. the Fischer-Tropsch synthesis of methanol, but more importantly facilitates the sequestration of CO_2 when fuelling a power plant [8, 9, 10, 11, 12].

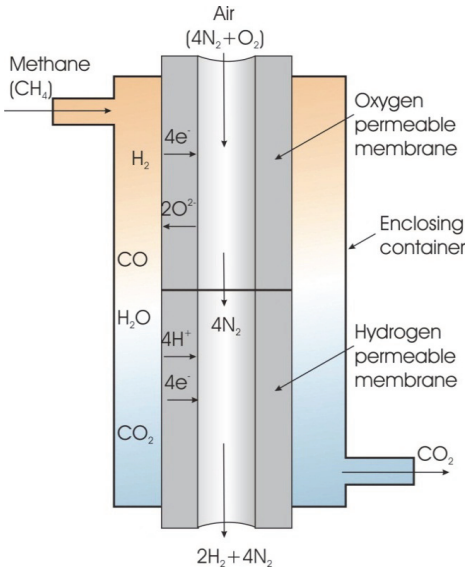

Figure 1.2. A reactor where an oxygen separation membrane is used for hydrogen production [12].

Inorganic membranes face competition from other membrane types and technologies and they have their strengths and weaknesses. In the case of oxygen permeable membranes this technology competes with liquefaction and distillation of air (the cryogenic technique). For

example, recent modelling of the oxy-fuel process with integrated MIEC membranes exhibits lower energy losses compared to the separation technology based on cryogenic air [2]. However, inorganic membranes for oxygen separation are 100% selective and operate at high temperatures and can thus be closely integrated with other power technology components (oxidation, heat exchange, turbines and fuel cells). This technology is mature and close to implementation. The Norwegian oil company Statoil (formerly Statoil and Norsk Hydro) has taken a strong interest in it, and conducted its own research and development in cooperation with universities and institutes (University of Oslo (UiO), Norwegian University of Science and Technology (NTNU), SINTEF). In the case of oxygen permeable inorganic membranes, our research group at UiO is currently addressing problems related to defects and surface kinetics [7, 8, 9, 13, 14].

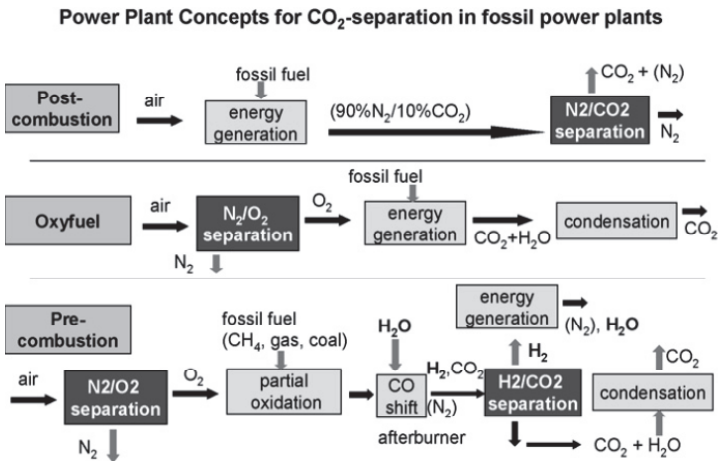

Figure 1.3. The concepts for CO_2 capturing [9].

Furthermore, membranes should be engineered to be productive and to suit different gas streams, as listed [9]:

- Post-combustion (CO_2/N_2 separation)
- Pre-combustion (H_2/CO_2 separation)
- Oxy-fuel combustion (O_2/N_2 separation)

where the major goal is zero-emission of CO_2. Schematic representations of these three concepts are presented in Figure 1.3. Each concept focuses on membrane design for specific applications, i.e., polymeric membranes in post-combustion processes, micro-

porous ceramic membranes in pre-combustion and dense ceramic membranes for oxy-fuel processes [9].

Advanced Zero Emission Power (AZEP) developed by Norsk Hydro, now Statoil, uses the above listed concepts, integrating a MIEC membrane with the combustion chamber (Figure 1.4). The ceramic membrane is mounted into the combustion chamber as a CMT (Ceramic Monolith based Technologies) module (Figure 1.5). Before entering into the MIEC reactor feed side, the air is compressed and some oxygen is permeated through the membrane where it encounters a counter flow of natural gas and combustion takes place. During combustion heat is generated, raising the temperature to the required working level of the MIEC membrane. After combustion the exhaust gas contains mainly CO_2 and water and is transported through the HRSG (heating recovery steam generator) and then forwarded to the plants, where the water is condensed and the CO_2 can be transported onwards for the final disposal [8, 9, 15, 16, 17].

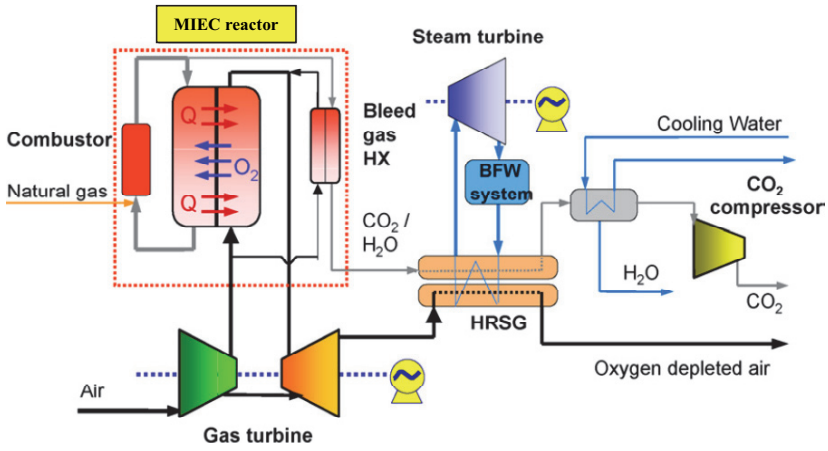

Figure 1.4. The AZEP (Advanced Zero Emission Power) process [17].

The module stack of the MIEC reactor (Figure 1.5) creates three "zones" – the zone up to 450 °C, the 900-1100 °C zone (combustion zone) and the zone up to 1300 °C. These "zones" are actually different modules connected into one stack. The middle one, where oxygen is transported through the oxygen MIEC membrane, is made of the material which is the topic of this work – lanthanum nickelate, $La_2NiO_{4+\delta}$ [17].

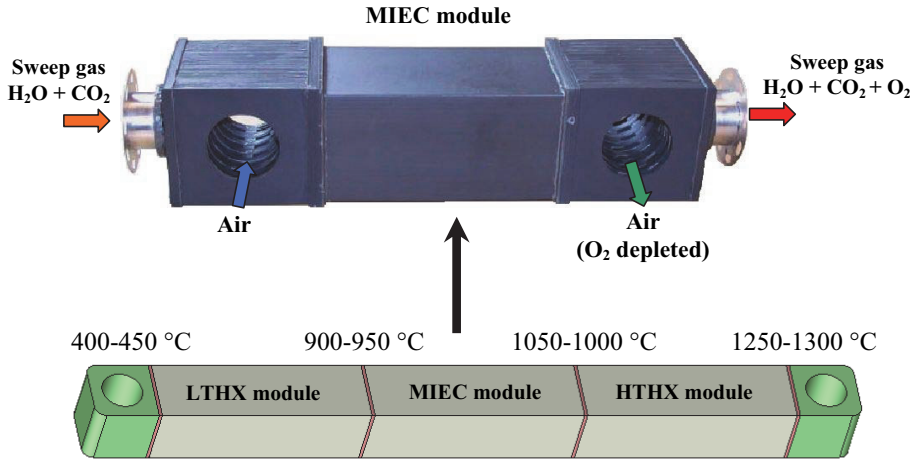

Figure 1.5. Directions of gaseous species flow in the MIEC module [17]. LTHX-low temperature heat exchanger, HTHX-high temperature heat exchanger.

1.2 The work in progress

Statoil (formerly Norsk Hydro) has identified and patented LNO as a mixed conductor for oxygen separation membranes. These membranes can be used to separate O_2 from N_2 in air. As such they can be integrated in various schemes for the production of O_2 and for integration in power plants for the utilisation of fossil fuels with CO_2 capture (cf. Figure 1.4). The material is permeable to oxygen by way of mixed oxide ion-electron transport. The oxygen ions are mobile as oxygen interstitials, while the electronic current is conveyed by electron holes. Both types of defects come about due to the excess of oxygen which the material possesses due to the tendency of Ni^{2+} to be partially oxidised to Ni^{3+}. LNO has a high electronic conductivity and a relatively high – yet rate limiting – oxygen ion conductivity. It exhibits relatively fast surface kinetics. The chemical expansion due to oxygen stoichiometry changes is favourably small. The material is now under investigation world-wide as a membrane material, but also as an electrode for SOFCs, electrolyser cells (SOECs) and catalysis [16, 18, 19, 20].

However, there are some challenges aimed at improving this material for higher efficiency in power plant devices as well as in SOFCs and catalysis. Transport properties, thermodynamic stability, component evaporation, surface kinetics and mechanical properties are some of the important issues highlighted for possible improvement. As

obvious for separation membranes, it is desirable to increase the oxygen ion diffusivity and surface kinetics further in order to increase the overall efficiency of a given membrane area at a given temperature and gradient. Long-term exposure to thermodynamic potential gradient – in this case the chemical potential of oxygen – causes important stability issues. Actually, the lifetime of the membrane is limited by the slow diffusion of cations, which produces material flow towards the high pO_2 side and demixing due to the difference in the diffusivity of the two cations (Figure 1.6).

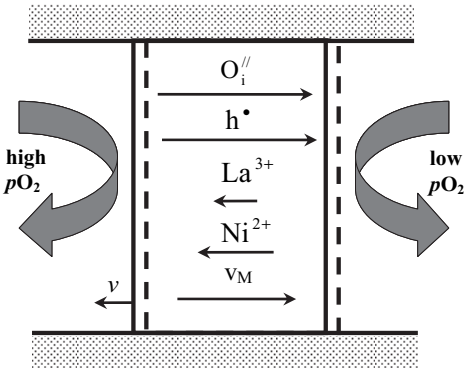

Figure 1.6. LNO membrane exposed to a gradient of pO_2, the flux of the mobile species and the shift of the LNO membrane due to cation diffusion (dash lines represent original position of the membrane).

It is desirable to reduce cation diffusion to prolong membrane life. In general, the above requires an understanding of thermodynamics and the mobility of defects in the material. The thermodynamic stability of the compound determines the temperature-pO_2-window the material can operate in and its tolerance to CO_2 (forming $La_2O_2CO_3$) and SO_3 (forming $La_2(SO_4)_3$), seal and manifold materials, etc. The stability also determines whether or not demixing will lead to eventual decomposition of the material in the pO_2 gradient. Finally, the volatility of one or more cation components is another indicator of chemical stability. It is generally desirable to improve overall chemical stability, although this must be judged based on what reaction products it is measured against. Besides, thermal and chemical expansion, thermal cyclability, sinterability, toxicity, cost, and recyclability are all further indicators of the quality of a membrane material [16, 17, 21].

The long-term goal of the current project is to improve the overall performance of the membrane material with respect to the above parameters. As part of the bigger project, the work in this thesis is focused on cation diffusion in nominally pure, undoped LNO under a

gradient in pO_2. This thesis will provide data on activation energies for diffusion coefficients of the La and Ni cations. It will also provide insight about the fastest moving cation, including the effects of microstructure (grain size, density, distribution of cations) and the micro-structural location of transport paths and rate limitations (bulk, grain boundaries, surface). The diffusion kinetics for La and Ni cations is also suggested based on Harrison's classification [22]. The LNO material was shown to be a material with relatively high cation diffusion, which should not be neglected as it influences long-term stability, as shown when an LNO membrane was exposed for an extended period of time to a gradient in pO_2.

As diffusion in general is a rather complex phenomenon, particularly diffusion in solids, the second chapter of this thesis will deal with the theoretical background of diffusion in solids. Wagner's law of parabolic growth and various solutions of Fick's second law (the solution for thin-film source and Whipple-Le Claire's equation) are derived/presented in this chapter. These mathematical models serve as the theoretical basis for the analysis of the data obtained by different techniques used for the determination of cation diffusion. The third chapter will introduce the ternary oxide LNO and its physical-chemical properties.

The fourth chapter will focus on experimental methods and the presentation of the selected results obtained by each technique. This work employs some commonly used techniques to determine cation diffusion: solid state reaction, (chemical) tracer diffusion, and inter-diffusion. Depending on the technique, various instrumental methods were used to analyse the samples, such as Scanning Electron Microscopy (SEM) with Energy-dispersive X-ray Spectroscopy (EDX) and Electron Backscatter Diffraction (EBSD), Secondary Ion Mass Spectrometry (SIMS), Electron Probe Micro Analysis (EPMA), X-ray Diffraction (XRD) and X-ray Photoelectron Spectroscopy (XPS).

The fifth chapter contains the papers published or under publication:

1. Determination of Inter-Diffusion Coefficients for the A- and B-site in the $A_2BO_{4+\delta}$ (A = La, Nd and B = Ni, Cu) System.
2. Determination of Chemical Tracer Diffusion Coefficients for the La- and Ni-site in $La_2NiO_{4+\delta}$ Studied by SIMS.

3. Determination of the Self-Diffusion Coefficient of Ni^{2+} in $La_2NiO_{4+\delta}$ by the Solid State Reaction Method.
4. Kinetic Decomposition of a $La_2NiO_{4+\delta}$ Membrane under an Oxygen Potential Gradient.

The sixth chapter will summarise the results and tackle some of the unanswered questions. The final chapter will conclude the Thesis and give some proposals for application of this material.

As a logical approach to improve LNO properties and stability, the substitution of cations would certainly be a strategy. Some experiments were performed in this direction by introducing dopants (Sr and Cu) on La and Ni sites. They are however not included in this thesis and are still being worked on. The preliminary results of LNO doping showed that the dopants actually destabilise the material by increasing the cation diffusivity of both sites.

1.3 References:

[1] Wikipedia, http://en.wikipedia.org/wiki/Atmosphere_of_Earth.

[2] M.-A. Dragan, *"Defect chemistry, transport properties and thermodynamic stability of acceptor doped and undoped layered La_2NiO_4"*, Ph. D. Thesis (2006), Fakultät für Mathematik, Informatik und Naturwissenschaften der Rheinisch-Westfälischen Technischen Hochschule Aachen, Germany.

[3] Encyclopaedia Britannica, www.britannica.com/bps/search?query=oxygen+in+medicine.

[4] J. B. Smith, *"Mixed oxygen ion/electron conductors for oxygen separation processes: Surface kinetics and cation diffusion"*, Ph. D. Thesis (2005), Faculty of Mathematics and Natural Sciences. University of Oslo, Norway.

[5] E.N. Naumovich, M.V. Patrakeev, V.V. Kharton, A.A. Yaremchenko, D.I. Logvinovich, F.M.B. Marques, *"Oxygen nonstoichiometry in $La_2Ni(M)O_{4+\delta}$ (M = Cu, Co) under oxidizing conditions"*, *Solid state Sciences*, 2005, 7, 1353-1362.

[6] M. Kilo, M. A. Taylor, Ch. Argirusis, G. Borchardt, B. Lesage, S. Weber, S. Scherrer, H. Scherrer, M. Schroeder, M. Martin, *"Cation self-diffusion of ^{44}Ca, ^{88}Y, and ^{96}Zr in single-crystalline calcia- and yttria-doped zirconia"*, *Journal of Applied Physics*, 2003, vol. 94, no. 12, 7547-7552.

[7] Z. Li, R. Haugsrud, J. B. Smith, T. Norby, *"Steady-State Permeation of Oxygen through $La_{1.9}Sr_{0.1}NiO_{4+\delta}$"*, *Journal of the Electrochemical Society*, 2009, 159(9), B1039-B1044.

[8] M.–L. Fontaine, Y. Larring, T. Norby, T. Grande, R. Bredesen, *"Dense ceramic membranes based on ion conducting oxides"*, *Annales de Chimie* (Cachan, France), 2007, 32(2), 197-212.

[9] M. Czyperek, P. Zapp, H.J.M. Bouwmeester, M. Modigell, K. Ebert, I. Voigt, W.A. Meulenberg, L. Singheiser, D. Stöver, *"Gas separation membranes for zero-emission fossil power plants: MEM-BRAIN"*, *Journal of Membrane Science*, 2010, 359, 149–159.

[10] A. Holt, T. Norby, "*Some considerations of materials with high oxygen deficiency for use in oxygen permeable membranes*", proc. IEA workshop on SOFC: Materials and Mechanisms, Wadahl, Norway, January 1999, K. Nisancioglu, ed., 123-35.

[11] C. Masters, *"The Fischer-Tropsch reaction"*, *Advances in Organometallic Chemistry*, 1979, 17, 61-103.

[12] T. Norby, R. Haugsrud, "*Dense Ceramic Membranes for Hydrogen Separation*" in *"Nonporous Inorganic Membranes"*, A. F. Sammells, M.V. Mundsschau, Eds., (WILLEY-VCH Verlag GmbH&Co. KGaA Weinheim 2006).

[13] Z. Li, R. Haugsrud, J. B. Smith, T. Norby, *"Transport properties and defect analysis of $La_{1.9}Sr_{0.1}NiO_{4+\delta}$"*, *Solid State Ionics*, 2009, 180, 1433-1441.

[14] J. B. Smith, T. Norby, *"On the steady-state oxygen permeation through $La_2NiO_{4+\delta}$ membranes"*, *Journal of the Electrochemical Society*, 2006, 153(2), A233-A238.

[15] R. Bredesen, K. Jordal, O. Bolland, *"High-temperature membranes in power generation with CO_2 capture"*, *Chemical Engineering and Processing,* 2004, 43, 1129–1158.

[16] S. G. Sundkvist, S. Julsrud, B. Vigeland, T. Naas, M. Budd, H. Leistner, D. Winkler, "*Development and testing of AZEP reactor components*", *International journal of green house gas control I*, 2007, 180-187.

[17] B. Vigeland, Project meeting, *"Demonstration of AZEP Reactor Module, CMT (Ceramic Monolith based Technologies")*, 2007, Porsgrunn.

[18] S. J. Skinner, J. A. Kilner, *"Oxygen diffusion and surface exchange in $La_{2-x}Sr_xNiO_{4+\delta}$"*, *Solid State Ionics*, 2000, 135, 709-712.

[19] E. Boehm, J. M. Bassat, M .C. Steil, P. Dordor, F. Mauvy, J. C. Grenier, *"Oxygen transport properties of $La_2Ni_{1-x}Cu_xO_{4+\delta}$ mixed conducting oxides"*, *Solid State Science*, 2003, 5, 973-981.

[20] W. Paulus, A. Cousson, G. Dhalenne, J. Berthon, A. Revcolevschi, S. Hosoya, W. Treutmann, G. Heger, R. Le Toquin, *"Neutron diffraction studies of stoichiometric and oxygen intercalated La_2NiO_4 single crystals"*, *Solid State Science*, 2002, 4, 565-573.

[21] M. Martin, *"Materials in thermodynamic potential gradients"*, *The Journal of Chemical Thermodynamics*, 2003, 35, 1291-1308.

[22] L.G. Harrison, *"Influence of dislocations on diffusion kinetics in solids with particular reference to the alkali halides"*, *Transactions of the Faraday Society*, 1961, 57, 1191-1199.

2. Theory

2.1 Diffusion in solids

Diffusion in solids describes the way particles (molecules, atoms, ions) move through solid matter from one point to another. Many chemical reactions also rely on diffusion through solids. If solid matter has a crystalline structure, diffusion takes place due to the presence of imperfections in the crystal lattice, i.e., point or higher dimensional defects. Vacancies and interstitial ions are examples of point defects and example of higher dimensional defect is dislocation. Solid state diffusion can take place through the material's volume, i.e., lattice or bulk diffusion and along line and surface defects, i.e., grain boundaries, dislocations, etc. Generally, diffusion along line and surface defects, is faster than that through bulk material and is often called short-circuit diffusion. As both paths (bulk and diffusion along line defects) contribute during diffusion through solid state, their contribution ratio depends on many factors, such as: temperature, partial pressures or activities of constituents of compounds, microstructure, grain size, porosity, etc.

The following terms can be found in literature to describe diffusion and diffusion-controlled reactions or processes under different experimental conditions: self-, tracer and inter-diffusion of atoms and ions, diffusion of defects, chemical diffusion, ambipolar diffusion, etc. It is therefore important to present the diffusion mechanisms before any further discussion of diffusion in solids. Different types of defects result in different mechanisms of diffusion. The following diffusion mechanisms can be distinguished (Figure 2.1) [1, 2, 3, 4, 5, 6]

- Ring mechanism
- Vacancy mechanism

- Divacancy mechanism
- Interstitial mechanism
- Interstitialcy mechanism
- Crowdion

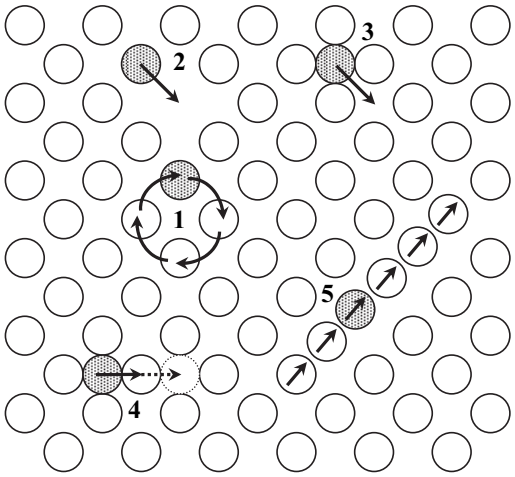

Figure 2.1. The schematics of principal diffusion mechanisms: 1. ring mechanism, 2. vacancy mechanism, 3. interstitial mechanism, 4. interstitialcy mechanism, 5. crowdion.

Ring mechanism involves a rotation of 3 (or more) atoms as a group by one atom distance. This mechanism has been proposed for diffusion in metals, but because of its complexity due to collective atomic motion, this mechanism is improbable in oxides. The ring mechanism does not involve lattice defects and cannot satisfactorily explain observations on different rates of self-diffusion of atoms, so this approach to diffusion mechanisms has been abandoned for cases relevant to this thesis [1].

The *vacancy mechanism* involves an atom jumping from its normal lattice position into an adjacent unoccupied lattice position (vacancy). Atoms move through a lattice by a series of exchanges with vacancies that are in its vicinity. In thermal equilibrium, the site fraction of vacancies in a mono-atomic crystal lattice is given by the following equation [1]

$$C_{\mathrm{v}}^{\mathrm{eq}} = \exp\left(-\frac{\Delta G_{\mathrm{v}}^{\circ}}{k_{\mathrm{B}}T}\right) = \exp\left(\frac{\Delta S_{\mathrm{v}}^{\circ}}{k_{\mathrm{B}}}\right)\exp\left(-\frac{\Delta H_{\mathrm{v}}^{\circ}}{k_{\mathrm{B}}T}\right) \quad \textbf{2.1}$$

where ΔG_v° is the Gibbs free energy of vacancy formation, ΔS_v° is the formation entropy, ΔH_v° is the formation enthalpy, T is the absolute temperature and k_B is the Boltzmann constant. Eq. 2.2 below, gives the exchange jump rate Γ of vacancy-mediated jump of a matrix atom to a particular neighbouring site [1]

$$\Gamma = \omega_v C_v^{eq} = v^\circ \exp\left(\frac{\Delta S_v^\circ + \Delta S_{m,v}}{k_B}\right)\exp\left(-\frac{\Delta H_v^\circ + \Delta H_{m,v}}{k_B T}\right) \quad \textbf{2.2}$$

where ω_V is the exchange rate between an atom and a vacancy, v° is the pertinent attempt frequency, and $\Delta H_{m,v}$ and $\Delta S_{m,v}$ are the enthalpy and entropy of vacancy migration, respectively. By inserting a lattice parameter (a) and geometry factor (γ) into Eq. 2.2 one can obtain the equation for the diffusivity of vacancies [1]

$$D_v = \gamma a^2 v^\circ \exp\left(\frac{\Delta S_v^\circ + \Delta S_{m,v}}{k_B}\right)\exp\left(-\frac{\Delta H_v^\circ + \Delta H_{m,v}}{k_B T}\right) \quad \textbf{2.3}$$

The vacancy diffusion coefficient (D_v) is related to the self-diffusion coefficient of atoms (D_a) through the following relation

$$D_a N_a = D_v C_v \quad \textbf{2.4}$$

where N_a is the fraction of sites occupied by atoms, normally approximated to be 1. Eq. 2.4 can be generalised as $D_a N_a = D_d C_d$ and with good approximation used for any type of defects d.

As the vacancy mechanism is the dominant mechanism of self-diffusion in a number of ionic crystal and ceramic materials, particularly for cations, this transport via vacancies is supposed to be the main mechanism for cation diffusion in the subject material of this thesis, $La_2NiO_{4+\delta}$ (LNO). The above equations are, as already mentioned, given for the simplest example of mono-atomic crystal lattice and as such is not valid for the case of LNO. The appropriate diffusion coefficient for the LNO system is derived, with regard to its dominating defect structure (oxygen interstitials and electron holes) and can be written as

$$D_{Ni} = 16^{7/9}\gamma a^2 v p{O_2}^{2/9}\exp\left(\frac{\Delta S_m}{R} + \frac{\Delta S_S^\circ}{3R} - \frac{4\Delta S_{AF}^\circ}{3R} + \frac{4\Delta S_{Ox}^\circ}{9R}\right)\exp\left(-\frac{\Delta H_m}{RT} - \frac{\Delta H_S^\circ}{3RT} + \frac{4\Delta H_{AF}^\circ}{3RT} - \frac{4\Delta H_{Ox}^\circ}{9RT}\right) \quad \textbf{2.5}$$

where ΔS_m and ΔH_m are the entropy and enthalpy of migration of Ni vacancies and ΔS_S°, ΔS_{AF}° and ΔS_{Ox}° are the standard entropies and ΔH_S°, ΔH_{AF}° and ΔH_{Ox}° the standard enthalpies of formation of Schottky defects, anti-Frenkel defects, and oxygen interstitials and electron holes, respectively, and R is the gas constant (a detailed derivation of the expression is presented in Appendix I).

At this point one may add that beside "simple" vacancy mechanisms (i.e., direct jump to the neighbouring vacancy), in their atomistic calculation on migration paths of cation defects in $LaMnO_3$ (ABO_3 perovskite) De Souza *et al.* [7] suggested a more complex mechanism. They calculated that the most favourable diffusion path of Mn is curved and goes through an La vacant site, i.e., the A-site vacancy facilitates the diffusion of B-site cations.

The *divacancy mechanism* comes into play when two monovacancies agglomerate in a cluster and diffusion occurs via exchange with these aggregates. It is important to emphasise that the concentration of divacancies rises significantly at high temperatures (at temperatures below 2/3 of the melting point, diffusion via monovacancies is dominant, as explained above).

When the considerably smaller solute atoms are incorporated in the interstitial positions of the host solvent lattice it forms an interstitial solid solution. If these solute atoms jump from their initial interstitial sites to neighbouring interstitial positions, they diffuse by an *interstitial mechanism*. In this mechanism, the interstitial moves from its equilibrium position to the saddle-point configuration (considerable lattice distortion) and then returns to the equilibrium position on the neighbouring interstitial site. This mechanism is also called *direct interstitial mechanism*, as it is conceptually the simplest mechanism of diffusion. The diffusion coefficient of particles diffusing by this mechanism tends to be quite high. This mechanism is significant for the diffusion of light solute atoms, e.g. H, C, N and O in metals and other materials. In LNO oxygen diffuses via an interstitial mechanism [8, 9].

The *interstitialcy mechanism* occurs when an interstitial atom is almost equal in size to the lattice atoms and the distortion of the lattice becomes too large to make the interstitial mechanism probable. This mechanism is a collective mechanism, as at least two atoms are moving simultaneously. One variant of the interstitialcy mechanism is the *crowdion*. The

crowdion mechanism postulates that an extra atom lines up with other atoms and displaces several of them from their equilibrium positions along the line.

The mathematical treatment and the conditions for the general and special cases of cation diffusion phenomena in LNO are given in further text.

2.2 Fick's laws

The mathematical relationships which relate the diffusion rate with the concentration gradient required for the net mass transport are normally referred to as the laws of diffusion. The laws of diffusion are empirical, describing the phenomenology of the physical effect of diffusion. Adolf Fick was the first who recognized the analogy between the transfer of heat (discovered earlier by Jean Baptiste Fourier) and random molecular motions. He was the first to give the quantitative basis of diffusion, by adopting the mathematical equation of heat transfer. Therefore, the mathematical theory of diffusion in isotropic substances is based on the hypothesis that *the rate of transfer of diffusion substances through unit area of a section is proportional to the concentration gradient measured normal to the section* [10]. This is one way of interpreting Fick's first law of diffusion and flux in one dimension (x) can be represented thus:

$$j = -D\frac{\partial C}{\partial x} \qquad \textbf{2.6}$$

or as a general formula in three dimensions

$$\vec{j} = -D\nabla C \qquad \textbf{2.7}$$

where j and $\vec{j}$ are the flux density of particles, i.e., the rate of transfer per unit area of section, D is a proportionality factor known as diffusion coefficient, $\partial C/\partial x$ is the concentration gradient in the x-direction and ∇C is the concentration gradient vector. The nabla operator (∇) acts on the scalar concentration field $C(x, y, z, t)$ and produces the concentration gradient field ∇C [1]. The negative sign in Eqs. 2.6 and 2.7 is due to the opposite direction of diffusion to that of increasing concentration, i.e., diffusion occurs "downhill" from high to low concentration. Eq. 2.6 is applicable for isotropic materials but in general constitutes an approximation in the case of anisotropic materials in which the diffusion properties depend on the direction [10, 11, 12].

2.2.1 Fick's second law

When the fundamental differential equation of diffusion is derived from Eq. 2.6 for an isotropic medium and D is independent of C, one can write the equation for Fick's second law, also called *the linear diffusion equation* [1, 3, 10]

$$\frac{\partial C}{\partial t} = D\frac{\partial^2 C}{\partial x^2} \qquad \textbf{2.8}$$

Eq. 2.8, represents from a mathematical point of view a second-order partial differential equation [1, 10]. As Eq. 2.8 represents a general case we can solve it by formulating boundary (and initial) conditions. The solution of Fick's second law with thin-film source has been used for the analysis of the experimental data in some of the papers yet to be published.

2.2.2 Fick's second law – solution for thin-film source

The solution of Fick's second law for a thin-film source is also known as the solution for *instantaneous planar source*. This solution is usually used for the determination of diffusivities by tracer diffusion methods.

When the diffusing substance M is initially deposited at the time $t = 0$ onto the plane surface $x = 0$, the solution of Fick's second law for thin-film source is

$$C(x,t) = \frac{M}{2\sqrt{\pi Dt}}\exp\left(-\frac{x^2}{4Dt}\right) \qquad \textbf{2.9}$$

where M is the number of diffusing particles per unit area. The quantity $2\sqrt{Dt}$ represents a characteristic diffusion length, frequently occurring in diffusion problems, e.g. used for determination of the type of diffusion kinetics by the Harrison's classification. This solution can also be termed as the Gaussian solution.

2.2.3 Limitations of Fick's law

Fick's law is ideally valid only for continuous materials and cannot properly handle discontinuous structures. Some limiting cases for Fick's law include ordering or clustering

in solids and relaxation and resonance phenomena directly connected to sensitivity to atomic jumps [2].

2.3 The various diffusion coefficients

A diffusion coefficient is a quantitative term that describes the rate of the diffusion process. It can be defined as *the rate of transfer of the diffusion substance across unit area of a section, divided by the space gradient of concentration at the section*, with the restriction to one dimension only [10]. In SI units a diffusion coefficient has the unit of m^2 s^{-1}, while in practical cases it is more common to use cm^2 s^{-1}. The following is an elaboration on the different diffusion coefficients [1].

2.3.1 Self- and tracer diffusion coefficient

If the atom A diffuses in a pure solid crystal of the same composition A, under no driving force (concentration gradient, etc) then this process is called *self-diffusion* and its measure is determined by the self-diffusion coefficient [1, 4]. In such case, the atom has the same random movement probability in any direction. As it is not possible to follow the movement of one atom inside the crystal, "labelled" atoms – tracers – are used in experiments, which enable a very good approximation of the self-diffusion. Tracers are usually isotopes A^* of the same elements, radioactive (radio tracers) or not. Typical experimental setups for tracer (self-diffusion) experiments are given in Figure 2.2.

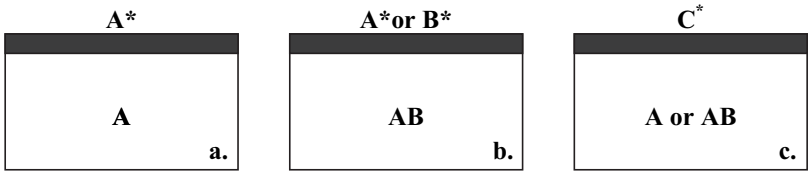

Figure 2.2. Various setups for diffusion studies: a. A* tracer (isotope) for determination of self-diffusion in pure crystal A, b. A* and B* isotope thin-films on AB alloy for determination of self-diffusion of alloy components, c. C* thin-film on pure component A or alloy AB for determination of impurity diffusion.

The connection between the tracer and the self-diffusion coefficient is given by

$$D_{\mathrm{A}}^{\mathrm{A}^*} = f\ D_{\mathrm{A}}^{\mathrm{A}} \quad \text{where} \quad D_{\mathrm{A}}^{\mathrm{A}} = \frac{d^2}{6\bar{\tau}} \qquad \textbf{2.10}$$

The latter is called the Einstein-Smoluchowski relation, where d is the jump length and $\bar{\tau}$ is the mean residence time of an atom on a particular site of the crystal at any arbitrary chosen site and f is the tracer correlation factor, smaller than or equal to unity, which depends on the mechanism of diffusion and the structure [1]. For cubic structures only, the factor f is independent of temperature, due to the equal probability of jumps (isotropy) towards the nearest neighbouring sites [2].

When using a foreign component C* as a tracer, it yields an impurity diffusion coefficient, $D_{\mathrm{AorAB}}^{\mathrm{C}^*}$ which is sometimes referred to as the foreign diffusion coefficient. The determination of impurity diffusion coefficients is often used as an approximation of self-diffusion coefficients for safety or economical reasons connected to isotopes.

2.3.2 Chemical diffusion and inter-diffusion coefficients

Diffusion due to a gradient in the chemical composition, i.e., concentration gradient, is referred to as *chemical diffusion* or *inter-diffusion* [1, 2, 13]. Generally, the diffusion flux is proportional to the gradient of the chemical potential [1] and is proportional to the concentration gradient only for diluted systems of ideal solutions of neutral non-interacting particles. As a consequence, one can argue that chemical diffusion is diffusion only in the gradient of chemical potential in the compounds which deviates from the compounds' stoichiometric composition (where, as described above, the equalisation of the gradients in chemical potential and concentration are a rather special case). However, in principle chemical diffusion and inter-diffusion are used as synonyms in literature [1, 2, 3, 10, 13].

Inter-diffusion was theoretically analysed by Lawrence S. Darken in 1948. In his work he described inter-diffusion using intrinsic diffusivities in binary substitutional alloys. From a series of mathematical derivations the following equation for the inter-diffusion coefficient is given [1]:

$$\widetilde{D}_{\mathrm{Darken}} = (N_{\mathrm{A}} D_{\mathrm{B}}^{*} + N_{\mathrm{B}} D_{\mathrm{A}}^{*})\Phi \qquad \textbf{2.11}$$

where D_{A}^{*} and D_{B}^{*} are the intrinsic diffusion coefficients of the components A and B, N_{A} and N_{B} are the molar fractions of the same components and Φ is the thermodynamic factor ($\Phi \equiv \partial \ln a_{\mathrm{i}} / \partial \ln N_{\mathrm{i}}$, where a_{i} is the thermodynamic activity and N_{i} the molar fraction of the component i). The derivations ending with Eq. 2.11 are called the *Darken equations* or the

Darken-Dehlinger equations. They are widely used for substitutional binary alloys due to their simplicity. There are two methods of extracting diffusivities from concentration-depth profiles: the *Boltzmann-Matano method* and the related approach proposed by *Sauer and Freise* [1, 2, 10]. The Boltzmann-Matano method is applicable for determination of the concentration-dependent diffusivity ($\widetilde{D}(C)$) when the diffusion couple volume is unchanged during inter-diffusion [1]. A problem with this method is that a special reference plane, the so called Matano plane, has to be defined accurately, otherwise the method can induce large diffusion coefficient errors. The Sauer-Freise approach is applicable when the diffusion couple volume changes during inter-diffusion. In this method the need for determination of the Matano plane is avoided and the error associated with it is diminished [1].

2.4 Electrochemical transport and Wagner's parabolic rate law

In ionic solids such as the oxide dealt with in this thesis, charged particles are simultaneously exposed to chemical and electrical potential gradients, i.e., electrochemical potential gradients. This constitutes the foundation for the description of all electrical and mass transport processes that involve charged species in ionic solids.

2.4.1. Derivation of the general electrochemical transport equations

If the particles i are considered to flow across a plane due to the driving force F, then their flux density is determined by the product of their volume concentration c_i and the average migration or drift velocity v_i

$$j_i = c_i v_i \qquad \textbf{2.12}$$

For uncorrelated movements, the migration velocity v_i of the particle i is proportional to the driving force F_i

$$v_i = B_i F_i \qquad \textbf{2.13}$$

where B_i is the proportionality factor and is defined as the average migration velocity of the particle per unit driving force. It is referred to as mechanical mobility (Beweglichkeit).

The driving force F_i is given as the negative value of the potential gradient normal to the cross-sectional area in the plane

$$F_i = -\frac{dP_i}{dx} = -\frac{d\mu_i}{dx} \quad \textbf{2.14}$$

where P_i is the potential, here written for uncharged particles equal to the chemical potential μ_i.

By combining Eqs. 2.12, 2.13 and 2.14, we can write the equation for flux density, expressed with regard to the chemical potential of the particles i

$$j_i = -c_i B_i \frac{d\mu_i}{dx} \quad \textbf{2.15}$$

The mechanical mobility of the particles i is connected with the diffusion coefficient (D_i) through the expression

$$D_i = B_i k_B T \quad \textbf{2.16}$$

By combining Eqs. 2.15 and 2.16, the expression for flux density obtains the following form

$$j_i = -\frac{D_i c_i}{k_B T} \frac{d\mu_i}{dx} \quad \textbf{2.17}$$

In ionic compounds, chemical and electrical potentials act together and simultaneously [14] and for the charged particles *i*, we can write

$$\eta_i = \mu_i + z_i e \varphi \quad \textbf{2.18}$$

where η_i is the electrochemical potential, μ_i the chemical potential, z_i the number of charges, e the elementary charge, and φ the electrical potential. According to Eq. 2.18, the electrochemical potential gradient for a one-dimension can be expressed as

$$\frac{d\eta_i}{dx} = \frac{d\mu_i}{dx} + z_i e \frac{d\varphi}{dx} \quad \textbf{2.19}$$

Eq. 2.19 represents the fundamentals for the theory derived by Carl Wagner to describe the oxidation of metals. It can be used for all transport processes in ionic materials in electrochemical gradients. By combining Eqs. 2.17 and 2.19 we can obtain the Wagner-type flux expression for the flux density of each particle i [14].

$$j_\mathrm{i} = -\frac{D_\mathrm{i} c_\mathrm{i}}{k_\mathrm{B} T}\frac{\mathrm{d}\eta_\mathrm{i}}{\mathrm{d}x} = -\frac{D_\mathrm{i} c_\mathrm{i}}{k_\mathrm{B} T}\left(\frac{\mathrm{d}\mu_\mathrm{i}}{\mathrm{d}x} + z_\mathrm{i} e \frac{\mathrm{d}\varphi}{\mathrm{d}x}\right) \qquad \textbf{2.20}$$

By using the Nernst-Einstein equation [1] conductivity (σ) can substitute diffusivity and an alternative expression for flux density is obtained

$$j_\mathrm{i} = -\frac{\sigma_\mathrm{i}}{(z_\mathrm{i} e)^2}\left(\frac{\mathrm{d}\mu_\mathrm{i}}{\mathrm{d}x} + z_\mathrm{i} e \frac{\mathrm{d}\varphi}{\mathrm{d}x}\right) \qquad \textbf{2.21}$$

We can also write the expression for partial current density i_i

$$i_\mathrm{i} = z_\mathrm{i} e j_\mathrm{i} = -\frac{\sigma_\mathrm{i}}{z_\mathrm{i} e}\left(\frac{\mathrm{d}\mu_\mathrm{i}}{\mathrm{d}x} + z_\mathrm{i} e \frac{\mathrm{d}\varphi}{\mathrm{d}x}\right) \qquad \textbf{2.22}$$

If we take the sum of all partial current densities i_i-s of all species k, the net current density in the sample is

$$i_\mathrm{tot} = \Sigma_\mathrm{k} z_\mathrm{k} e j_\mathrm{k} = -\Sigma_\mathrm{k} \frac{\sigma_\mathrm{k}}{z_\mathrm{k} e}\left(\frac{\mathrm{d}\mu_\mathrm{k}}{\mathrm{d}x} + z_\mathrm{k} e \frac{\mathrm{d}\varphi}{\mathrm{d}x}\right) \qquad \textbf{2.23}$$

Using the definitions for total conductivity and for transport number[1] (t) we can relate the electrical potential gradient to the net (total, external) current density, the total conductivity, the transport number and the chemical potential gradient of all charge carriers [14]:

$$\frac{\mathrm{d}\varphi}{\mathrm{d}x} = -\frac{i_\mathrm{tot}}{\sigma_\mathrm{tot}} - \Sigma_\mathrm{k} \frac{t_\mathrm{k}}{z_\mathrm{k} e}\frac{\mathrm{d}\mu_\mathrm{k}}{\mathrm{d}x} \qquad \textbf{2.24}$$

If Eq.2.24 is inserted into Eq. 2.20, the following expression for the flux density of particles i is obtained.

[1] Total conductivity: $\sigma_\mathrm{tot} = \Sigma_\mathrm{k} \sigma_\mathrm{k}$; Transport number: $t_\mathrm{k} = \frac{\sigma_\mathrm{k}}{\sigma_\mathrm{tot}} = \frac{\sigma_\mathrm{k}}{\Sigma_\mathrm{k} \sigma_\mathrm{k}}$.

$$j_i = -\frac{D_i c_i}{k_B T}\frac{d\eta_i}{dx} = -\frac{D_i c_i}{k_B T}\left(\frac{d\mu_i}{dx} - \frac{i_{tot}}{\sigma_{tot}} - z_i \sum_k \frac{t_k}{z_k}\frac{d\mu_k}{dx}\right) \quad \textbf{2.25}$$

It is important to mention here that the net current is zero ($i_{tot} = 0$) for the case of the reaction product layer growth by the solid state reaction method (SSR), presented in further text, and Eq. 2.25 becomes

$$j_i = -\frac{D_i c_i}{k_B T}\frac{d\eta_i}{dx} = -\frac{D_i c_i}{k_B T}\left(\frac{d\mu_i}{dx} - z_i \sum_k \frac{t_k}{z_k}\frac{d\mu_k}{dx}\right) \quad \textbf{2.26}$$

2.4.2 Derivation of the parabolic rate constant for the reaction product layer growth by the solid state reaction method

When two solid phases A and B are in contact, react and form a new product phase C, this type of reaction is categorised as a heterogeneous solid state reaction. The A and B phases may be either compounds or chemical elements. The heterogeneous reactions begin with nucleation at the reactants contact points followed by further growth of the nucleus. The driving force for this type of SSRs is the difference in Gibbs energy between the reactants and the reaction product [15]. The characteristic aspect of the heterogeneous SSRs is the fact that the reaction layer C actually separates the reactants A and B and that the growth (the rate of reaction) of the reaction layer C occurs by transport of the reactants through the product layer [11, 15]. As the reaction layer grows (thickness), the reaction rate decreases with time. This was explained by Wagner [11, 15, 16] for the high temperature oxidation of metals and is known as *the Wagner oxidation theory* or *Wagner's parabolic rate law*. In general, the rate of growth of the thickness of reaction layer C (x) is inversely proportional to the thickness of reaction layer C:

$$\frac{dx}{dt} = k_p^* \frac{1}{x} \quad \textbf{2.27}$$

By integrating Eq. 2.11 we obtain the equation for the parabolic rate law

$$x^2 = 2k_p^* t + C_0 = k_p t + C_0 \quad \textbf{2.28}$$

where k_p is the rate constant and C_0 is the integration constant.

We can further derive the relationship between the parabolic rate constant and the self-diffusion coefficient used in this work for the determination of the fastest moving cation in

LNO by the SSR method. The fastest moving cation in LNO is Ni^{2+}, which is determined by using the inert Pt markers (details in Paper III). For further derivation, the chemical potential of the ions involved in mass transport in LNO can be expressed as follows:

$$\mathrm{d}\mu_{\mathrm{Ni}^{2+}} = \mathrm{d}\mu_{\mathrm{Ni}} - 2\mathrm{d}\mu_{\mathrm{e}^-} \quad \textbf{2.29}$$

$$\mathrm{d}\mu_{\mathrm{La}^{3+}} = \mathrm{d}\mu_{\mathrm{La}} - 3\mathrm{d}\mu_{\mathrm{e}^-} \quad \textbf{2.30}$$

$$\mathrm{d}\mu_{\mathrm{O}^{2-}} = \mathrm{d}\mu_{\mathrm{O}} + 2\mathrm{d}\mu_{\mathrm{e}^-} \quad \textbf{2.31}$$

If we insert Eqs. 2.29, 2.30 and 2.31 for chemical potentials into Eq. 2.26, after several calculation steps we can write the following equations for the flux density of the fastest moving cation, Ni^{2+}

$$j_{\mathrm{Ni}^{2+}} = -\frac{D_{\mathrm{Ni}^{2+}} c_{\mathrm{Ni}^{2+}}}{k_{\mathrm{B}} T} \frac{1}{\mathrm{d}x} (\mathrm{d}\mu_{\mathrm{Ni}} - t_{\mathrm{Ni}^{2+}} \mathrm{d}\mu_{\mathrm{Ni}} - t_{\mathrm{La}^{3+}} \mathrm{d}\mu_{\mathrm{La}} + t_{\mathrm{O}^{2-}} \mathrm{d}\mu_{\mathrm{O}} + 2\mathrm{d}\mu_{\mathrm{e}^-} (t_{\mathrm{Ni}^{2+}} + t_{\mathrm{La}^{3+}} + t_{\mathrm{O}^{2-}} + t_{\mathrm{e}^-} - 1)) \quad \textbf{2.32}$$

where the $t_{\mathrm{Ni}^{2+}} + t_{\mathrm{La}^{3+}} + t_{\mathrm{O}^{2-}} + t_{\mathrm{e}^-} - 1$ term is necessarily equal to zero, since the sum of all transport numbers is equal to 1. If the transport numbers of Ni, La and O are considered to be much smaller than 1, then the terms $t_{\mathrm{Ni}^{2+}} \mathrm{d}\mu_{Ni}$, $t_{\mathrm{La}^{3+}} \mathrm{d}\mu_{\mathrm{La}}$ and $t_{\mathrm{O}^{2-}} \mathrm{d}\mu_{\mathrm{O}}$ are cancelled and finally the expression for the flux density of Ni^{2+} can be expressed as

$$j_{\mathrm{Ni}^{2+}} = -\frac{D_{\mathrm{Ni}^{2+}} c_{\mathrm{Ni}^{2+}}}{k_{\mathrm{B}} T} \frac{\mathrm{d}\mu_{\mathrm{Ni}}}{\mathrm{d}x} \quad \textbf{2.33}$$

we can now integrate Eq. 2.33 by using the chemical potential of Ni at the phase boundaries between the reaction product layer and the reactants, as the boundary conditions and the expression obtained is:

$$j_{\mathrm{Ni}^{2+}} = -\frac{1}{k_{\mathrm{B}} T} c_{\mathrm{Ni}^{2+}} D_{\mathrm{Ni}^{2+}} \frac{\mathrm{d}\mu_{\mathrm{Ni}}}{\mathrm{d}x} = -\frac{1}{\Delta x} \frac{1}{k_{\mathrm{B}} T} \int_{\mu'_{\mathrm{Ni}}}^{\mu''_{\mathrm{Ni}}} c_{\mathrm{Ni}^{2+}} D_{\mathrm{Ni}^{2+}} \mathrm{d}\mu_{\mathrm{Ni}} = \frac{1}{\Delta x} k_{\mathrm{r}} \quad \textbf{2.34}$$

where k_{r} is the so-called rational reaction rate constant and Δx is the instantaneous thickness of the reaction product layer. Eq. 2.35 is used for describing the growth rate of the ternary compound as

$$\frac{\mathrm{d}\Delta x}{\mathrm{d}t} = j_{\mathrm{Ni}^{2+}} \frac{V_\mathrm{m}}{N_\mathrm{A}} V_\mathrm{m} = \frac{V_\mathrm{m} k_\mathrm{r}}{\Delta x} \qquad \textbf{2. 35}$$

where V_m is the molar volume as the result of the transport of one equivalent of ions through the reaction product and N_A is Avogadro's constant. Consequently the parabolic (reaction) rate constant k_p can be expressed as

$$k_\mathrm{p} = -\frac{V_\mathrm{m}}{RT} \int_{\mu_\mathrm{Ni}}^{\mu_\mathrm{Ni}''} c_{\mathrm{Ni}^{2+}} D_{\mathrm{Ni}^{2+}} \mathrm{d}\mu_\mathrm{Ni} \qquad \textbf{2.36}$$

where R is the gas constant obtained through the relation $R = N_\mathrm{A} k_\mathrm{B}$. In Paper III, which deals with the SSR method, the parabolic rate constant was further derived and integrated with regard to the activity of La_2O_3, i.e., the chemical potential of Ni was connected and expressed through the activity of La_2O_3. The self-diffusion coefficient is related to the parabolic rate constant as shown in Eq. 2.36. As the parabolic rate constant can be obtained experimentally, it is just a matter of mathematical derivation to express and calculate the self-diffusion coefficient from Eq. 2.36. The SSR method is used in this work to obtain the parabolic rate constant, and subsequently the self-diffusion coefficient of Ni^{2+} in LNO was calculated.

Schmalzried [15] derived these equations for the case of simultaneous and opposite diffusion of ions which is valid for any diffusion controlled reaction. Wagner's contribution is that the parabolic rate constant is expressed in terms of independently measurable properties and that the transport (diffusion) of the reactants (ions) through the (reaction) product layer is rate-determining for the overall reaction [10, 15, 16, 17].

2. 5 Whipple-Le Claire's equation

The mathematics of grain boundary diffusion represents one of the most difficult problems in the analysis of diffusion in ceramic and other polycrystalline solids. There are several analytical models dealing with this issue. The simplest analytical model (Fisher's model) assumes a grain boundary as a semi-infinite and isotropic slab with uniform width and high diffusivity embedded in a low-diffusivity semi-infinite perfect crystal (Figure 2.3). Two physical parameters describe the grain boundary: the grain boundary width w and the grain

boundary diffusivity D_{GB}. As implied above, the grain boundary diffusivity is usually much larger than that of bulk (lattice), $D_{GB}>>D_B$ [1, 18, 19].

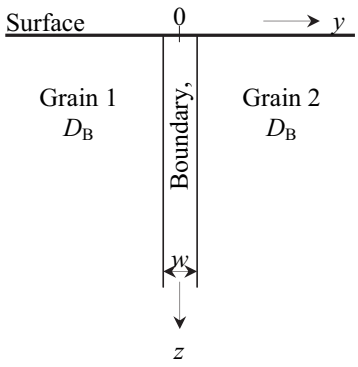

Figure 2.3. The simplest (Fisher's) model of an isolated grain boundary. D_{GB} is the grain boundary diffusivity, D_B is the bulk diffusivity, w is the grain boundary width and y and z are the coordinates.

As this model represents the simplest one, most of the mathematical treatments of grain boundary diffusion are based on Fisher's model [20]. In this model the basic physical assumptions are: during diffusion, annealing mass transport takes place through the lattice, i.e., bulk material as well as along grain boundaries. As a consequence of higher diffusivity along grain boundaries, the diffusant penetrates much deeper along this path than in the other alternatives (e.g. the lattice). Therefore, based on this, the mathematical derivation of the diffusion equation follows the next assumptions:

- Fick's laws are obeyed in the lattice and the grain boundary diffusions.
- The diffusion coefficients D_B and D_{GB} are isotropic and independent of concentration, position and time.
- The diffusant flow is continuous in the lattice and the grain boundary, meaning that the diffusant concentration and flux are continuous.
- The diffusant concentration variation in the grain boundary is negligible due to its small width.

After applying these assumptions, Fisher gave the first approximate mathematical solution of this problem:

$$\frac{\partial c_B}{\partial t} = D_{GB}\frac{\partial^2 c_B}{\partial z^2} + \frac{2D_B}{w}\frac{\partial c_B}{\partial y}\bigg|_{y=w/2} \quad \textbf{2.37}$$

Based on this approximate solution given by Fisher, many authors gave analytical solutions for various boundaries and initial conditions (e.g. Suzuoka, Whipple, Wood, etc). In this thesis, Le Claire's analysis (explained in more detail in the papers yet to be published), was used to interpret tracer diffusion experiments [18, 21]. Le Claire's analysis was based on Whipple's exact solution of wD_{GB} from the penetration depth measurement using a previously obtained value for the bulk diffusion coefficient, and in literature this is referred to as Whipple-Le Claire's equation. The following expressions are conveniently usable for the evaluation of wD_{GB}, i.e., grain boundary diffusivity

$$wD_{GB} = 2\sqrt{\frac{D_B}{t}}\left(-\frac{\partial \ln \bar{c}}{\partial z^{6/5}}\right)^{-5/3}(0.78)^{5/3} \quad \textbf{2.38}$$

$$wD_{GB} = 1.322\sqrt{\frac{D_B}{t}}\left(-\frac{\partial \ln \bar{c}}{\partial z^{6/5}}\right)^{-5/3} \quad \textbf{2.39}$$

$$wD_{GB} = 0.3292\sqrt{\frac{D_B}{t}}\left(-\frac{\partial \log \bar{c}}{\partial z^{6/5}}\right)^{-5/3} \quad \textbf{2.40}$$

where $\bar{c}$ represents the average concentration in a thin layer perpendicular to the grain boundary plane and other letters have their usual meanings.

2.6 The Kirkendall effect

The visualisation of diffusion in a binary A-B system can be represented by the respective intrinsic fluxes j_A and j_B, with respect to the position of inert markers, positioned along the anticipated diffusion zone:

$$j_A = -D_A\frac{\partial C_A}{\partial x},\ j_B = -D_B\frac{\partial C_B}{\partial x} \quad \textbf{2.41}$$

These intrinsic fluxes have opposite directions during diffusion and their sum is equal to the velocity of the inert markers, originally positioned on the contacting interface before diffusion:

$$v = -(V_B j_B + V_A j_A) = V_B (D_B - D_A) \frac{\partial C_B}{\partial x} \quad \textbf{2.42}$$

where V_A and V_B are the partial molar volumes of the A and B components. The inequality of these fluxes causes net mass transport during inter-diffusion [1] between the two phases. This mass transport is accompanied by the displacement of the contacting interface (the Kirkendall plane). When this mass transport is diffusion-controlled the inert markers move parabolically with respect to time with the following velocity (the Kirkendall velocity):

$$v_K = \frac{dx}{dt} = \frac{x_K - x_0}{2t} = \frac{x_K}{2t} \quad \textbf{2.43}$$

where x_K and x_0 (equal to 0) represent the positions of the Kirkendall plane at times t and 0, respectively. The phenomenon of the migration of the initial diffusion couple contact interface as the result of the inequality of the diffusion coefficients ($D_A \neq D_B$) is called *the Kirkendall effect* [22, 23, 24] (Figure 2.4).

This was first observed by Kirkendall in his experiment with copper and α-brass [22, 23], where it was shown that Zn atoms diffuse faster than Cu, causing the movement of the Mo wires used as inert markers. Further analysis and generalisation of the Kirkendall effect was performed by Darken [25, 26].

In his original experiment [22] Kirkendall discovered that the displacement of the original interface was accompanied by a pore formation, which confirmed his suggestion for a vacancy diffusion mechanism rather than an exchange mechanism [2]. As the result of further research on diffusion porosity it was concluded that it was essentially another phenomenon called *the Frenkel effect* [24]. Actually, the Kirkendall and Frenkel effects are competitive phenomena and they originate from different vacancy interactions with dislocations and micro-cavities, which are respectively responsible for these effects [24].

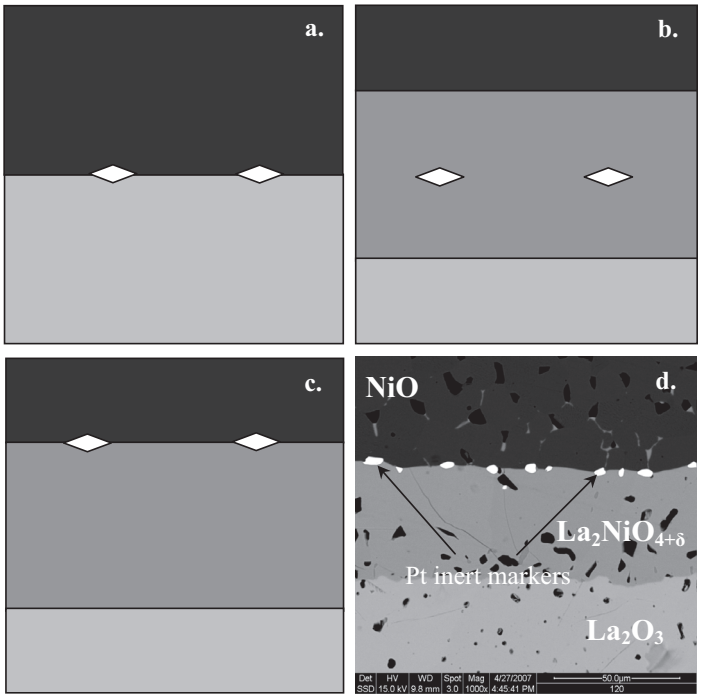

Figure 2.4. Illustration of the Kirkendall effect in a diffusion grown product layer: a. original position of inert markers (white rectangular) on diffusion couple contact interface, b. position of inert markers when both components have the same diffusion coefficients ($D_A = D_B$) and c. position of inert markers when diffusion coefficients are unequal ($D_A \neq D_B$). d. SEM micrograph of an actual diffusion grown product layer experiment and position of inert marker after 386 hours annealing at 1350 °C.

Some new peculiarities of the Kirkendall effect have recently been observed. In thin-films and nano-materials diffusion actually occurs mainly along free surfaces (the Sub-surface Kirkendall effect) and grain boundaries (the GB Kirkendall effect) that represent short-circuit diffusion paths and the sink or source of vacancies and dislocations [24, 27].

2.7 The Harrison's classification

Ceramics and metals are more abundant as polycrystalline solids than as cases of single crystal. Many solid state reactions, phase transformations and micro-structural changes in these polycrystalline materials are generally diffusion-controlled. The structure of these materials strongly influences diffusion processes. When diffusion occurs, the diffusant tries to diffuse along the paths with least resistance, which are marked as short-circuiting paths in polycrystalline solids. These short-circuiting paths may be grain boundaries, dislocations

and other 1-, 2-, or 3-dimensional crystal imperfections. Diffusion is also dependent on the mis-orientation of grains, meaning the angle of grain boundaries for the short-circuiting paths.

During diffusion along those paths the diffusant "leaks" through the walls of the boundaries or other imperfection into the bulk of the crystals. This greatly depends on the experimental temperature (determining the ratio of short-circuit to bulk diffusivity) and the annealing time. In this way, the "leakage" determines to what extent diffusion along the grain boundaries is influenced by bulk and kinetics for the given conditions and subsequent mathematical analysis. Due to the complexity of this phenomenon it is rarely possible to decouple diffusion along grain boundaries from bulk (volume) diffusion [18]. Based on the limiting cases with respect to the extent of the leakage several kinetic regimes can be recognized in polycrystalline materials. Several authors have dealt with this phenomenology and some of the most important kinetic models are: Harrison's model of parallel grain boundaries, Fisher's model for an isolated grain boundary, the cubic grain model of Suzuoka, Levine and MacCullum's general model of diffusion in isotropic polycrystal, etc [18, 21, 28]. Harrison classified diffusion kinetics into tree regimes – "A"-, "B"- and "C"-type kinetics [18, 21, 28]. These kinetics regimes according to Harrison's classification have been widely used in practice and they are schematically illustrated in Figure 2.5.

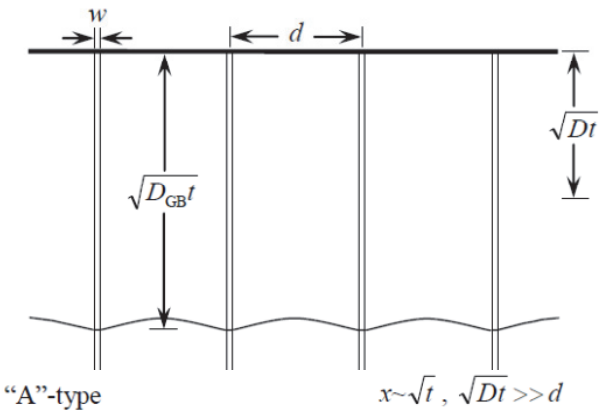

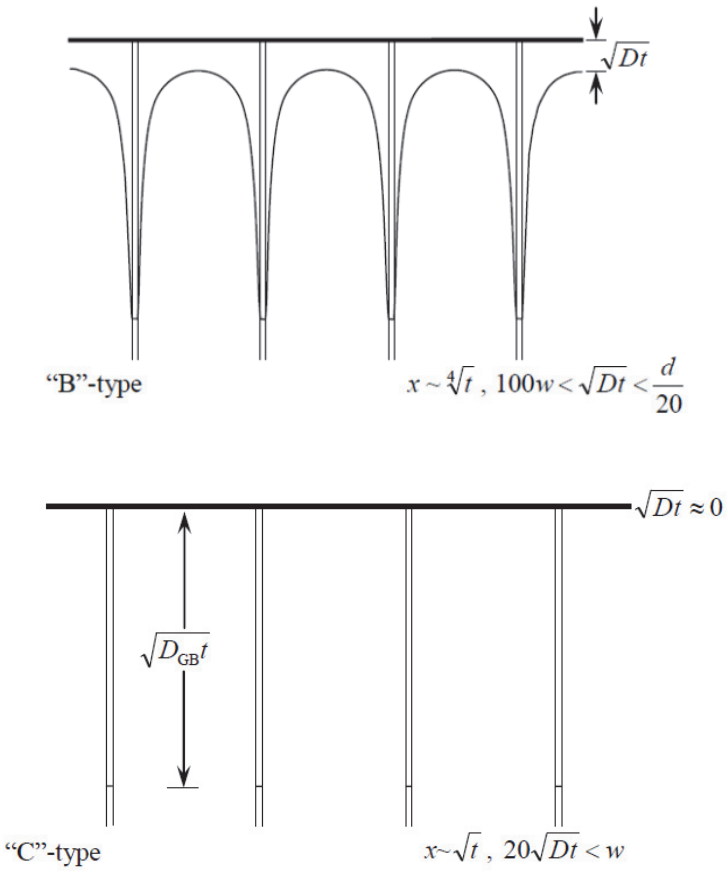

Figure 2.5. Schematic illustration of "A"-, "B"- and "C"-type kinetics in polycrystal, according to Harrison's model with parallel grain boundaries [17].

The "A"-type kinetics is actually the limiting case when the annealing time is long with small grain size, which means that the volume diffusion length is much larger than the grain diameter (d). Based on this condition we can write the following for "A"-type kinetics

$$\sqrt{D_B t} >> d \qquad \textbf{2.44}$$

In "A"-type kinetics the diffusant is not confined to any grain boundary, but the leakages from different grain boundaries extensively overlap with each other. During this extensive leakage from the grain boundaries into the bulk, the diffusant atoms move along numerous grain boundaries as well as trough the grain bulk. When observed macroscopically the

diffusion coefficient represents an average of the D_B and D_{GB} diffusion coefficients and the whole system appears to obey Fick's law for homogeneous systems. In this system diffusion is described with the effective diffusion coefficient (D_{eff}) and the penetration depth in this type of kinetics is proportional to $\sqrt{t}$. The effective diffusion coefficient is an apparent one and corresponds to all diffusing atoms, irrespective of their migration paths along the grain boundaries or the bulk crystal. The relation between the grain boundary and the bulk is given in Hart's equation [29]:

$$D_{eff} = gD_{GB} + (1-g)D_B \quad \textbf{2.45}$$

Where g is the fraction of atomic sites in the grain boundaries or dislocations and we can calculate it by following equation [30]:

$$g \approx 3\frac{w}{d} \quad \textbf{2.46}$$

w and d are the grain boundary width and the grain diameter, respectively. However, despite extensive work on modelling "A"-type kinetics [31, 32, 33, 34], there is still no convincing analytical model for this kinetic type [18].

The most commonly observed kinetic regime belongs to "B"-type kinetics. In this kinetic type diffusion occurs simultaneously along grain boundaries and through the bulk, but contrary to "A"-type kinetics, diffusion along grain boundaries can be considered isolated. In addition, the penetration depth of the diffusant is much longer than that of the bulk. The condition for "B"-type kinetics can be described as:

$$100w << \sqrt{D_B t} << \frac{d}{20} \quad \textbf{2.47}$$

where all factors have their usual meanings. Opposite to "A"-type kinetics, the effective diffusion coefficient is not an issue as the diffusing atoms have highly non-uniform mobility in grain boundaries and bulk. Due to this, diffusion profiles for "B"-type kinetics usually have two distinct regions – a steeper part close to the interface region, corresponding to bulk diffusion and a flatter part with low concentration of the diffusant, corresponding to grain boundary diffusion.

In “C”-type kinetics the bulk diffusion coefficient is negligibly small (or equal to zero) when compared to the grain boundary diffusion coefficient so that the bulk diffusion length is much smaller than that along the grain boundaries. The diffusion is characterised by only one apparent diffusion coefficient – the grain boundary diffusion coefficient. The condition for this kinetic type is:

$$\sqrt{D_{GB}t} < w \qquad \textbf{2.48}$$

“C”-type diffusion kinetics is very rarely obtained under the usual experimental conditions. In order to observe/obtain this limiting case of diffusion kinetics it is necessary that the diffusion annealing experiment is conducted at very low temperatures and/or for a very short annealing time. Only under these conditions is it possible to restrict the diffusion process along the grain boundaries. The first measuring of “C”-type kinetics was carried out by Atkinson *et al.* [35] using an extremely complicated measuring method for ^{63}Ni diffusion along grain boundaries in NiO at 500 °C.

2.8 Materials in a thermodynamic potential gradient

In many applications oxides are exposed to a thermodynamic potential gradient, which would lead to material’s inevitable degradation, usually manifested as a local change in their composition, structure or morphology [36, 37, 38, 39]. The thermodynamic potential gradient can be a gradient in chemical potential (of one or more elements), temperature, electrical potential or a pressure [36], which then acts as a driving force, inducing fluxes of mobile species in the material. The cations are mobile species that cause the following degradation phenomena [36, 40]:

- Kinetic demixing
- Kinetic decomposition
- Morphological instability

At this point one may emphasise that existing mathematical models [39, 41] for formal treatment of these phenomena are originally developed for a system where the oxygen lattice is regarded as immobile. However, LNO – the subject material of this Thesis - is a well known material for fast oxygen transport. According to [42] the existing mathematical models can also be applied to such materials and it was indeed applied to the case where

the material has fast oxygen transport. All in all, if the material has predominant electronic transport, the same mathematical models can be used for both cases.

The following is an example of a mathematical treatment of kinetic decomposition for a $La_2NiO_{4+\delta}$ membrane in an oxygen chemical potential gradient. If LNO is exposed to an oxygen potential gradient (Figure 2.6), the Gibbs-Duhem relation

$$x_{La}d\mu_{La} + x_{Ni}d\mu_{Ni} + x_{O}d\mu_{O} = 0 \qquad \textbf{2.49}$$

where x_{La}, x_{Ni} and x_O are the molar fractions of La, Ni and O, respectively, states that the gradient in chemical potential of oxygen induces opposite gradients in the chemical potentials of the La and Ni cations, These gradients in chemical potentials are the driving forces for the fluxes of cations toward the side with the higher pO_2.

As mentioned above, if two cations have different mobilities, the initially homogeneous oxide will become inhomogeneous (Figure 2.6). The faster cation, in this case Ni^{2+}, will move faster towards the higher pO_2 side and become enriched on the surface. Consequently, the lower pO_2 side will be enriched with the slower moving La cation.

The cation and vacancies reactions at the surfaces of the oxide cause the kinetic decomposition (Figure 2.6) [36, 37, 38, 39, 40].

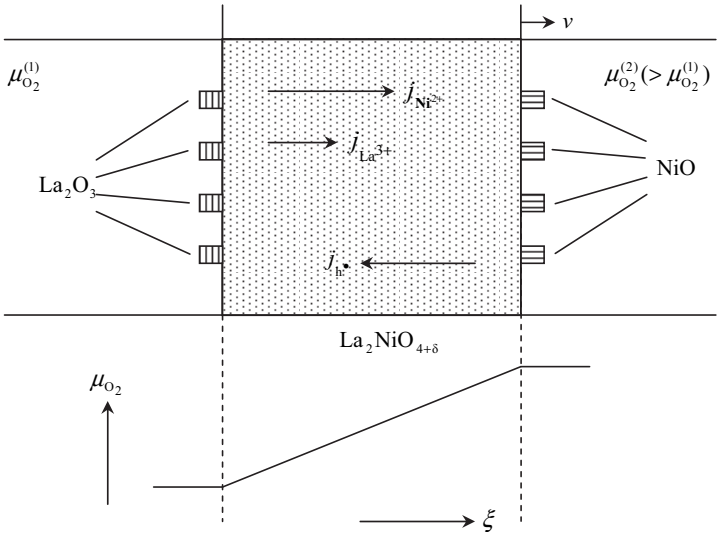

Figure 2.6. The scheme of kinetic decomposition of LNO exposed to an oxygen potential gradient due to different diffusivities of La and Ni cations. NiO and La_2O_3 are decomposition products [37].

The flux equations of the chemical components (cations) are as follows [37]

$$j_{Ni^{2+}} = -\frac{c_{Ni} D_{Ni}}{RT}\left(\nabla\mu_{NiO} - \frac{1}{2}\nabla\mu_{O_2}\right) \quad \textbf{2.50}$$

$$j_{La^{3+}} = -\frac{c_{La} D_{La}}{RT}\left(\frac{1}{2}\nabla\mu_{La_2O_3} - \frac{3}{4}\nabla\mu_{O_2}\right) \quad \textbf{2.51}$$

where c_{Ni} and c_{La} are the concentrations of the respective cations, D_{Ni} and D_{La} are their diffusion coefficients and μ_{NiO}, $\mu_{La_2O_3}$ and μ_{O_2} are the chemical potentials. Based on the integrated Gibbs-Duhem equation and taking into consideration the cation fluxes, for steady state conditions (Eq. 2.53 below), we obtain the equation for the steady state decomposition (Eq. 2.54 below)

$$\mu_{NiO} + \mu_{La_2O_3} \cong \mu_{La_2NiO_4}{}^{\circ} \quad \textbf{2.52}$$

$$\frac{j_{Ni}}{c_{Ni}} = \frac{j_{La}}{c_{La}} = v_S \quad \textbf{2.53}$$

$$\Delta\mu_{NiO} = \frac{1 - \frac{3}{2}\frac{D_{La}}{D_{Ni}}}{2 + \frac{D_{La}}{D_{Ni}}}\Delta\mu_{O_2} \quad \textbf{2.54}$$

This represents a chemical potential change for the component NiO induced by an oxygen chemical potential difference. If this $\Delta\mu_{NiO}$ surpasses the stability limit of the LNO (Gibbs energy of formation) the decomposition of the LNO into its components will occur. Therefore, through

$$\Delta\mu_{NiO(max)} = -\Delta G_{La_2NiO_4}{}^{\circ} \quad \textbf{2.55}$$

and combining it with Eqs. 2.54, we can calculate the critical oxygen potential difference across the LNO to initialise the kinetic decomposition

$$\ln\left(\frac{pO_2{}^{//}}{pO_2{}^{/}}\right)^{critical} = -\frac{2 + \frac{D_{La}}{D_{Ni}}}{1 - \frac{3}{2}\frac{D_{La}}{D_{Ni}}} \times \frac{\Delta G_{La_2NiO_4}{}^{\circ}}{RT} \quad \textbf{2.56}$$

$pO_2^{/}$ and $pO_2^{//}$ are oxygen partial pressure at low and high pO_2 sides, respectively, of the LNO membrane. If $D_{Ni} > 3/2\, D_{La}$ then NiO will be formed on the side with the higher oxygen potential, whereas if $D_{Ni} < 3/2\, D_{La}$, then NiO will be formed on the side with the lower oxygen potential. Consequently, La_2O_3 will be formed on the corresponding opposite side [37, 39, 43, 44]. According to literature and the above treatment of kinetic decomposition example of LNO membrane for oxygen separation, we can conclude that some of degradation mechanisms will occur in all semiconducting compounds that have different diffusivities of chemical components (cations) ($D_A \neq D_B$), regardless of anionic transport.

2.9 References

[1] H. Mehrer, *Diffusion in Solids; Fundamentals, Methods, Materials, Diffusion-Controlled Processes*, Springer-Verlag Berlin Heidelberg, 2007.

[2] J. Philibert, *Atom movements: Diffusion and mass transport in solids*, Les editions de physique, Les Ulis Cedex A, France, 1991.

[3] H. Schmalzried, *Chemical Kinetics of Solids*, *Solid State Reactions*, Chapter 4, Verlag Chemie, Weinheim/Bergstr., 1974.

[4] R. Tilley, *Understanding solids*, John Wiley & Sons, LTD, The Atrium, Southern Gate, Chichester, West Sussex PO19 8SQ, England, 2004.

[5] A. West, *Basic Solid State Chemistry, Second Edition*, John Wiley & Sons, LTD, Chichester, West Sussex PO19 8SQ, England, 2003.

[6] W. van Gool, *Fast ion transport in solids: Solid state batteries and devices*, North-Holland publishing company, Amsterdam – London, 1973.

[7] R. A. De Souza, M. S. Islam, W. Ivers-Triffée, "*Formation and migration of cation defects in the perovskite oxide $LaMnO_3$*", *Journal of Materials Chemistry*, 1999, 9, 1621-1627.

[8] J. B. Smith, T. Norby, "*On the steady-state oxygen permeation through $La_2NiO_{4+\delta}$ membranes*", *Journal of the Electrochemical Society*, 2006, 153(2), A233-A238.

[9] Z. Li, R. Haugsrud, J. B. Smith, T. Norby, "*Steady-State Permeation of Oxygen Through $La_{1.9}Sr_{0.1}NiO_{4+\delta}$*", *Journal of the Electrochemical Society*, 2009, 159(9), B1039-B1044.

[10] J. Crank, *Mathematics of Diffusion*, Oxford University Press, 1979.

[11] W. D. Kingery, H. K. Bowen, D. R. Uhlmann, *Introduction to Ceramics 2nd Edition*, John Wiley & Sons, INC., 1976.

[12] M. E. Glicksman, *Diffusion in Solids; Field Theory, Solid-State Principles and Applications*, John Wiley & Sons, INC., 2000.

[13] IUPAC Compendium of Chemical Technology, 2003, http://goldbook.iupac.org/.

[14] P. Kofstad, *Nonstoichiometry, Diffusion, and Electrical Conductivity in Binary Metal Oxides*, Chapter 6, John Wiley & Sons, Inc., New York, 1972.

[15] H. Schmalzried, *Chemical Kinetics of Solids, Solid State Reactions*, Chapter 6, Verlag Chemie, Weinheim/Bergstr., 1974.

[16] C. Wagner, "*The mechanism of formation of ionic compounds of higher order (double salts, spinels, silicates)*", *Zeitschrift für Physikalische Chemie*, 1936, Abt. B. 33-34, 309.

[17] C. Wagner, "*Theory of the tarnishing process*", Z. *Phys. Chem.*, 1933, Abt. B. 21, 25.

[18] I. Kaur, Y. Mishin, W. Gust, *Fundamentals of Grain and Interphase Boundary Diffusion*, John Wiley & Sons LTD, Chichester, 1995.

[19] A. D. Le Claire, A. Rabinovitch, "*A mathematical analysis of diffusion in dislocations. I. Application to concentration tails*", *Journal of Physics C: Solid State Physics.*, 1981, 14, 3863-3879.

[20] J. C. Fisher, "*Calculation of diffusion penetration curves for surface and grain-boundary diffusion*", *Journal of Applied Physics*, 1951, 22, 74.

[21] C. Herzig, Y. Mishin, *Diffusion in Condensed Matter, Methods, Materials, Models*, editors P. Heitjans, J, Kärger, Springer, Berlin, 2005, p. 337.

[22] A. D. Smigelskas, E. O. Kirkendall, "*Zinc diffusion in α brass*", *Transactions Of The American Institute Of Mining And Metallurgical Engineers Institute Of Metals Division, Metals Technology*, 1946, vol. 13, No. 7, Tech.

[23] E. O. Kirkendall, T. Thomassen, "*Rates of diffusion of copper and zinc in α-brass*", *Transactions Of The American Institute Of Mining And Metallurgical Engineers Institute Of Metals Division, Metals Technology*, 1938, vol. 967, 18 pp.

[24] L. N. Paritskaya, "*Kirkendall effect: dramatic history of discovery and developments*", *Defect and Diffusion Forum*, 2006, vol. 249. 73-80.

[25] A. A. Kodentsov, A. Paul, F. J. J. van Loo, "*The Kirkendall plane in binary inter-diffusion systems*", *Defect and Diffusion Forum*, 2004, vols. 233-234, 61-75.

[26] L. S. Darken, "*Diffusion, mobility, and their interrelation through free energy in binary metallic systems*", *Transactions Of The American Institute Of Mining And*

Metallurgical Engineers Institute Of Metals Division, Metals Technology, 1948, vol. 15, No. 1, Tech., 11 pp.

[27] B. Pieraggi, R. A. Rapp, F. J. J. van Loo, J. P. Hirth, "*Interfacial dynamics in diffusion-driven phase transformations*", *Acta Metallurgica et Materialia*, 1990, vol. 38, no. 9, 1781-1788.

[28] L.G. Harrison, "*Influence of dislocations on diffusion kinetics in solids with particular reference to the alkali halides*", *Transactions of the Faraday Society*, 1961, 57, 1191-1199.

[29] E. W. Hart, "*Role of dislocations in bulk diffusion*", *Acta Metallurgica et Materialia*, 1957, 5, 597.

[30] S. Miyoshi, M. Martin, "*B-Site cation diffusivity of Mn and Cr in perovskite-type LaMnO3 with cation-deficit nonstoichiometry*", *Physical Chemistry Chemical Physics*, 2009, 11, 3063-3070.

[31] I. V. Belova, G. E. Murch, "*Exploration of the transition from Harrison type-A to type-B kinetics regimes in grain boundary diffusion*", *Defect and Diffusion Forum*, 2008, Vols. 273-276, 425-430.

[32] I. V. Belova, G. E. Murch, T. Fiedler, "*The Harrison diffusion kinetics regimes in grain boundary diffusion: Lattice Monte Carlo Modelling of the effect of segregation*", *Defect and Diffusion Forum*, 2011, Vols. 309-310, 9-19.

[33] I. V. Belova, G. E. Murch, "*Investigation of Harrison type-A, B and intermediate AB kinetics regimes in grain boundary diffusion*", *Defect and Diffusion Forum*, 2009, Vols. 283-286, 697-704.

[34] I. V. Belova, "*Analysis of the Hart equation in fine-grained material*", *Defect and Diffusion Forum*, 2001, Vols. 194-199, 1223-1226.

[35] A. Atkinson, R. I. Taylor, "*The diffusion of nickel-63 along grain boundaries in nickel oxide*", *Philosophical Magazine*, 1981, A43, p. 979.

[36] M. Martin, "*Materials in thermodynamic potential gradients*", *The Journal of Chemical Thermodynamics*, 2003, 35, 1291-1308.

[37] H. Schmalzried, *Chemical Kinetics of Solids, Solid State Reactions*, Chapter 8, Verlag Chemie, Weinheim/Bergstr., 1974.

[38] O. Teller, M. Martin, "*Kinetic demixing of (Co,Ni)O in an electric field*", *Solid State Ionics*, 1997, 101-103, 475-478.

[39] H. Schmalzried, W. Laqua, P. L. Lin, "*Crystalline oxide solid solutions in oxygen potential gradients*", *Verlag der Zeitschrift für Naturforschung*, 1979, 34a, 192.

[40] H. J. M. Bouwmeester, A. J. Burggraaf, in: P. J. Gellings, H. J. M. Bouwmeester (Editors), *The CRC Handbook of Solid State Electrochemistry*, CRC Press, Boca Raton, 1996.

[41] H. Schmalzried, W. Laqua, "*Multicomponent oxides in oxygen potential gradients*", *Oxidation of Metals*, 1981, 15, 339-353.

[42] H.-I. Yoo, C.-E. Lee, R. A. De Souza, M. Martin, "*Equal mobility of constituent cations in* $BaTiO_3$", *Applied Physics Letters*, 2008, 92(25), 252103/1-252103/3.

[43] R. H. E. van Doorn, H. J. M. Bouwmeester, A. J. Burggraaf, "*Kinetic decomposition of* $La_{0.3}Sr_{0.7}CoO_{3-\delta}$ *perovskite membranes during oxygen permeation*", *Solid State Ionics*, 1998, 111, 263-272.

[44] H. L. Lein, K. Wiik, T. Grande, "*Kinetic demixing and decomposition of oxygen permeable membranes*", *Solid State Ionics*, 2006, 177, 1587-1590.

3. Lanthanum nickelate, $La_2NiO_{4+\delta}$

3.1 Application

The discovery of high temperature superconductivity in $La_2CuO_{4+\delta}$ based systems brought to attention oxides with a perovskite-like K_2NiF_4-type layered structure [1]. Since lanthanum nickelate, $La_2NiO_{4+\delta}$ (LNO) (general formula A_2BO_4) is the nickel analogue of the cuprate, the main investigation was focused on its magnetic and electronic properties in the low temperature region below 150 °C [2]. Further investigation of this family of oxides showed that their mixed ion electron conductivity actually makes them more interesting for high temperature applications, such as cathode material for Solid Oxide Fuel Cells (SOFC) for the intermediate temperature range, membrane material in processes for oxygen separation [3-6], and catalytic material for partial oxidation of hydrocarbons [7, 8].

When LNO is utilised as a gas separation membrane it exhibits high oxygen flux [9]. Through the membrane, the oxygen moves via an interstitial mechanism accompanied by the electron holes in same direction, causing cation migration in the opposite direction – the focus of this work.

3.2 Structure and defects

Stoichiometric lanthanum nickelate La_2NiO_4, is the first member of the Ruddlesden-Popper series – $A_{n+1}M_nO_{3n+1}$ (n=1, 2, 3 …) and a perovskite-related compound with K_2NiF_4-type structure [10, 11]. However, the structure of LNO has been the subject of much debate, as it is dependent on temperature and stoichiometry. It can have large non-stoichiometry with regard to oxygen as interstitial (up to $\delta = 0.25$), compensated by electron holes in the form of Ni^{3+} [10-15]. Neutron diffraction as the function of

temperature showed that LNO crystallises in an orthorhombic structure (*Fmmm* or *Bmab*) at low temperatures below 150 °C (Low Temperature Orthorhombic phase, LTO) in the absence of an oxidizing atmosphere. *F4/mmm* and *I4/mmm* tetragonal structures were observed at high temperatures (High Temperature Tetragonal phase, HTT) in an oxidizing atmosphere (Figure 3.1) [10-17].

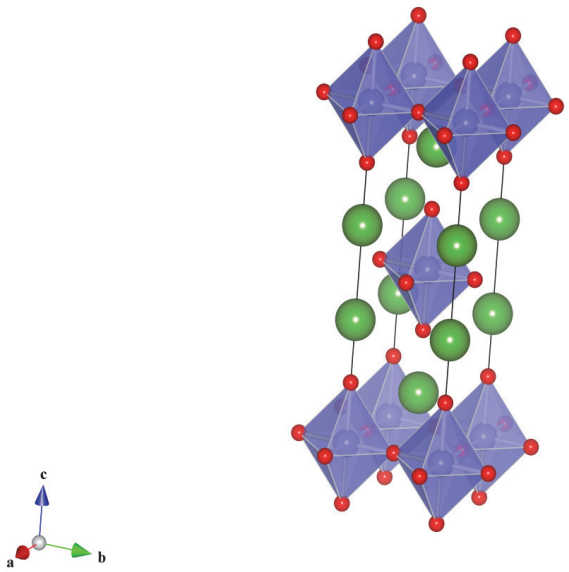

Figure 3.1. Schematic representation of the average tetragonal structure of LNO.

The structure of LNO can be seen as alternating perovskite, $LaNiO_3$ and rock salt, LaO layers along the *c*-axis, or alternate stacking of La_2O_2 double layers and NiO_2 sheets [16]. Based on the alternate stacking of layers, one can assume that charge is also separated between these layers ($La_2O_2^{2+}/NiO_2^{2-}$), where negatively charged defects are preferentially accommodated in the $La_2O_2^{2+}$ layers, while positively charged defects are in the NiO_2^{2-} layers [16]. Oxygen excess (interstitials), as negatively charged defects, are accommodated in the La_2O_2 rock salt layers, while the compensating positive electron holes are associated with a Ni site [18]. The oxygen interstitial crystallographic site in the La_2O_2 layer corresponds to a double tetrahedron formed by four apical oxygen ions and four La ions [11]. This interstitial oxygen stretches the La_2O_2 layer, additionally straining the already

elongated NiO_6 octahedra[1]. This strain can be released by the tilting of the NiO_6 octahedra, consequently leading to lower symmetry (orthorhombic), or by partial oxidation of Ni^{2+} into Ni^{3+} [11].

Stoichiometric LNO can be easily oxidised resulting in oxygen over-stoichiometric LNO (Figures 3.2 and 3.3).

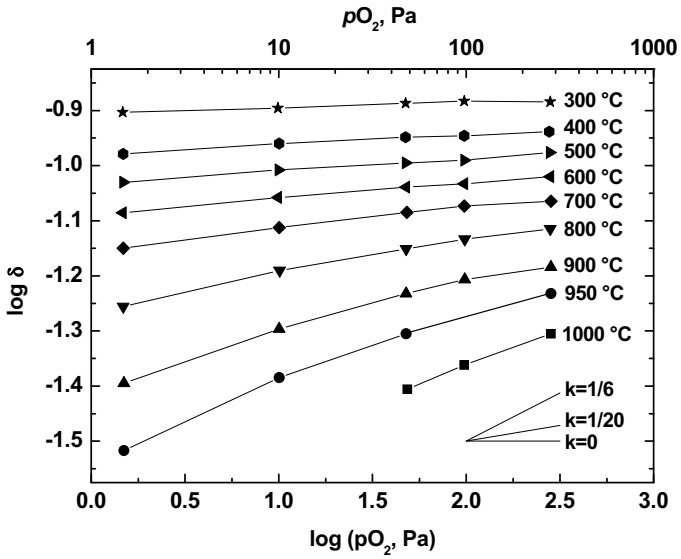

Figure 3.2. Dependencies of oxygen over-stoichiometry in LNO versus pO_2 at different temperatures, according to [5]

[1] Due to the electronic structure of Ni^{3+} $3d^7$, the Jahn-Teller effect tends to elongate NiO_6 octahedra along the *c* axis. In LNO with tetragonal structure distortion may be even more enhanced by the Lewis acid character of the rare-earth cation (La) in the Ni-O_{apical}-La dumbbell entity, which induces the shortening of the O_{apical}-La bond and the elongation of the opposite Ni-O_{apical} bond [12].

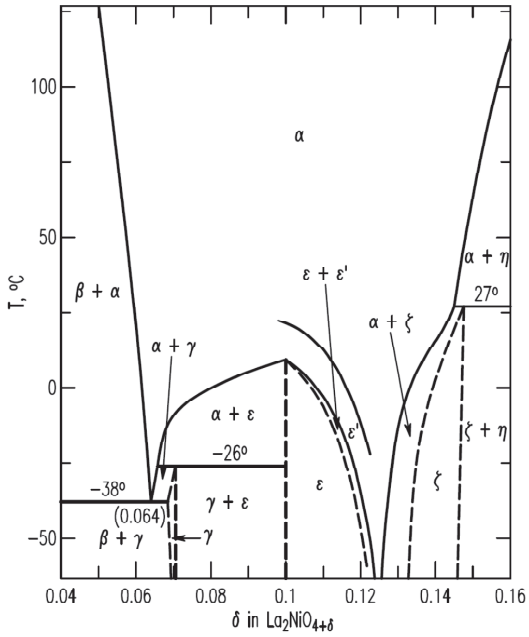

Figure 3.3. T-δ diagram of LNO. α denotes the high temperature phase with excess oxygen atoms in a disordered arrangement; β, γ, ε, are low temperature phases with ordered oxygen atoms.

We can write the LNO defect structure by the following defect reactions using the Kröger–Vink notation for the reaction of oxidation (intercalation of oxygen) (Eq. 3.1), the Schottky disorder (3.2) and the anti-Frenkel defect pairs (3.3)

$$\frac{1}{2}O_{2(g)} \leftrightarrow O_i^{//} + 2h^{\bullet} \qquad \textbf{3.1}$$

$$2La_{La}^{X} + Ni_{Ni}^{X} + 4O_O^{X} \leftrightarrow 2v_{La}^{///} + v_{Ni}^{//} + 4v_O^{\bullet\bullet} + La_2NiO_{4(s)} \qquad \textbf{3.2}$$

$$O_O^{X} + v_i^{X} \leftrightarrow O_i^{//} + v_O^{\bullet\bullet} \qquad \textbf{3.3}$$

where oxygen interstitials and electron holes are the majority defects in LNO and La, Ni and oxygen vacancies are the minority defects.

The corresponding simplified version of the total electroneutrality condition for Eqs. 3.1, 3.2 and 3.3, used in the papers for thermodynamic calculations, is

$$2[v_O^{\bullet\bullet}] + [h^{\bullet}] = 3[v_{La}^{///}] + 2[v_{Ni}^{//}] + 2[O_i^{//}] \qquad \textbf{3.4}$$

3.3 The Brouwer diagram and the diagram of the temperature dependences of defects

Brouwer diagrams are commonly used for schematic representation of defect concentration behaviour under simplified limiting cases of dominating defects. This means that the different defects will dominate at different pO_2s and temperatures, and defects can be expressed as a function of the chosen defects, one negative and one positive, i.e., we can anticipate the defect's behaviour at different pO_2s. The majority defects in LNO are plotted in the following Brouwer diagram (Figure 3.4). It can be seen how defect concentration in LNO changes with the change in pO_2. The anti-Frenkel defect pairs [16], together with electron holes, are presented as majority defects. The electroneutrality conditions are $n = 2[v_O^{\bullet\bullet}]$ for region **i**, $[O_i^{//}] = [v_O^{\bullet\bullet}]$ for region **ii**, and $2[O_i^{//}] = p$ for region **iii**.

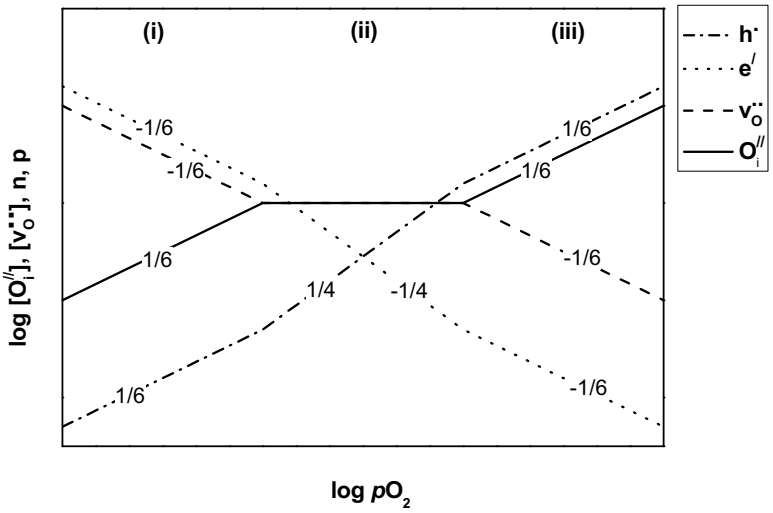

Figure 3.4. The Brouwer diagram for LNO with anti-Frenkel defect pair and electronic defects [19].

Defect concentration also depends on temperature. Based on Eqs. 3.1, 3.2 and 3.3 and the electroneutrality conditions Eq. 3.4 and the thermodynamics parameters of these defect reactions, the concentrations of majority and minority defects were expressed through Eqs. 3.5, 3.6, 3.7 and 3.8 below. The concentration of oxygen interstitials, electron holes, oxygen and Ni vacancies can be calculated using the standard entropy and enthalpy values of the respective reactions, from the literature [3, 18, 20]. The calculated concentrations of oxygen interstitials and electron holes as majority and vacancies of oxygen, Ni and La as minority defects are presented in Figure 3.5 as a function of temperature.

$$[O_i''] = (\frac{1}{4})^{1/3} p{O_2}^{1/6} \exp(\frac{\Delta S_{Ox}^\circ}{3R}) \exp(-\frac{\Delta H_{Ox}^\circ}{3RT}) \quad \textbf{3.5}$$

$$p = 2^{1/3} p{O_2}^{1/6} \exp(\frac{\Delta S_{Ox}^\circ}{3R}) \exp(-\frac{\Delta H_{Ox}^\circ}{3RT}) \quad \textbf{3.6}$$

$$[v_O^{\bullet\bullet}] = (\frac{1}{4})^{-1/3} p{O_2}^{-1/6} \exp(\frac{\Delta S_{AF}^\circ}{R} - \frac{\Delta S_{Ox}^\circ}{3R}) \exp(-\frac{\Delta H_{AF}^\circ}{RT} + \frac{\Delta H_{Ox}^\circ}{3RT}) \quad \textbf{3.7}$$

$$[v_{Ni}''] = 16^{7/9} p{O_2}^{2/9} \exp(\frac{\Delta S_S^\circ}{3R} - \frac{4\Delta S_{AF}^\circ}{3R} + \frac{4\Delta S_{Ox}^\circ}{9R}) \exp(-\frac{\Delta H_S^\circ}{3RT} + \frac{4\Delta H_{AF}^\circ}{3RT} - \frac{4\Delta H_{Ox}^\circ}{9RT}) \quad \textbf{3.8}$$

where ΔS_S°, ΔH_S°, ΔS_{AF}°, ΔH_{AF}°, ΔS_{Ox}°, ΔH_{Ox}° are the standard entropies and enthalpies of the reaction of creation of cation defects (the Schottky disorder), of the reaction of creation of oxygen defects (the anti-Frenkel disorder), and of the reaction of intercalation of oxygen i.e., oxidation, respectively. R and T have their usual meanings. Detailed derivations of the expressions for the calculation of vacancy concentration can be found in Appendix I. The concentration of La vacancies does not differ significantly from that of Ni, except for the simple numerical factor, as displayed in Appendix I. According to the calculations using Eqs. 3.5, 3.6, 3.7 and 3.8, the concentrations of cation defects are in the ppb range.

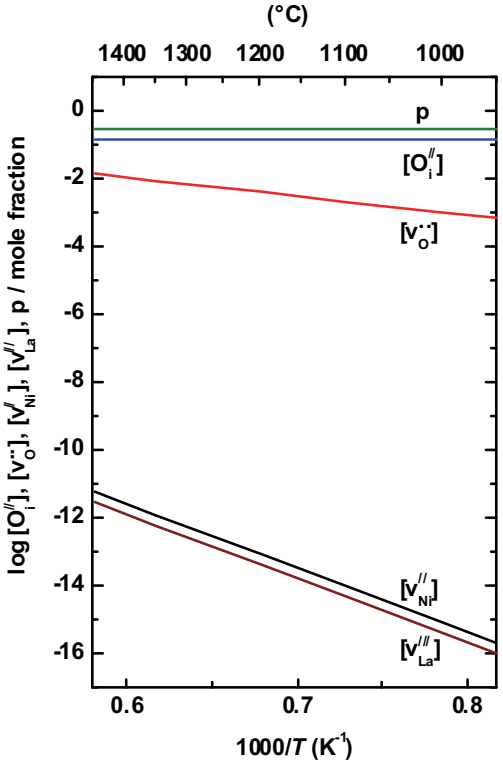

Figure 3.5. Temperature dependencies of the concentrations of majority O_i'' and p and minority $V_O^{\bullet\bullet}$, V_{Ni}'' and V_{La}''' defects in air, calculated based on the thermodynamic models of the Schottky defects, anti-Frenkel disorder and oxidation reaction.

3.3 Transport properties

Intercalation of oxygen into LNO begins with adsorption, charge transfer, and dissociation of ionised oxygen molecules. The incorporation of the adsorbed oxygen goes through the reaction Eq. 3.1, creating oxygen interstitials and compensating electron holes.

Through atomistic simulations and experimental studies of single crystal of LNO, Skinner [21] showed that in LNO oxygen diffuses much faster along the *ab*-plane than in the *c*-direction (anisotropic diffusion). Bassat *et al.* [10] came to the same conclusion for anisotropic diffusion, as a general case for the ionic transport in LNO. The discovered

strong anisotropic oxygen diffusion [10] is due to partial charge separation between the $La_2O_2^{2+}$ double layers and the NiO_2^{2-} sheets [16] with a large Coulomb potential. Besides, this anisotropy increases with temperature [10] as the average size of the perovskite-type NiO_2 sheets decreases with the increasing concentration of oxygen vacancies at higher temperatures.

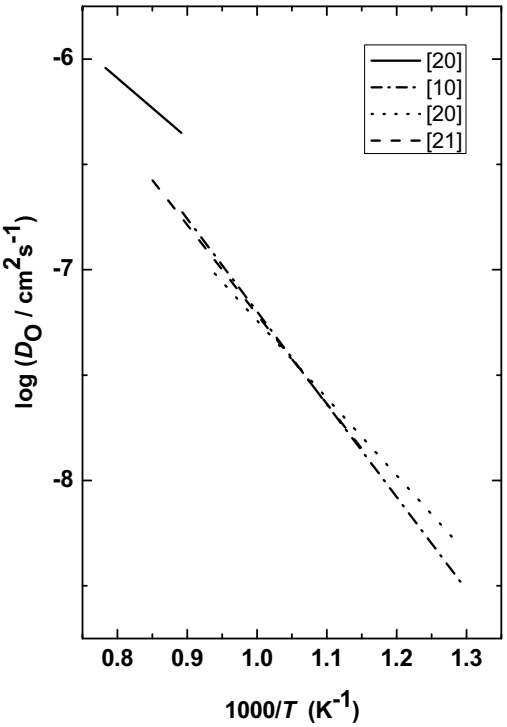

Figure 3.6. Arrhenius plot of oxygen self-diffusion coefficients.

Reported values for the activation energy of oxygen self-diffusion in LNO are in the range from ~50 to ~100 kJ/mol [7-11, 14, 22]. It is important to mention that for diffusion in the *c*-direction the reported activation energy is about four times less than that observed in the *ab*-plane [10]. However, we can presume that reported values for the self-diffusion of oxygen in ceramic polycrystalline samples reflect the average in the *ab*-plane and the *c*-direction [22]. At this point we can bring up the contribution of the grain boundaries to the diffusion of oxygen through polycrystalline LNO, which is particularly important for diffusion at lower temperatures [10]. It is interesting to note that the activation energy for

surface exchange (oxygen intercalation) is approximately double that of the oxygen diffusion [23]. The Arrhenius plot of the reported self-diffusion coefficients of oxygen is presented in Figure 3.6.

Oxygen diffusion has been extensively studied, but up until now there have been no reports on cation diffusion in LNO. Work on the determination of the diffusion coefficients of the cations in LNO is elaborated in detail in the following papers. However, when comparing oxygen with cation diffusion in LNO, the difference of several orders of magnitude is evident. Oxide ions are orders of magnitude faster than cations, in accord with their lower activation energies (reported as 50-100 versus 150-450 kJ/mol [25, 26, 27]). Cations in LNO will be shown to be faster than in most other perovskite-related oxides.

Besides oxygen ion conduction, LNO is also a p-type electronic conductor, thus exhibiting mixed oxide ion and electronic conduction. Its electronic conductivity is in the order of 100 S/cm while its oxide ion conductivity is in the order of 0.01 S/cm at 800 °C [9]. The electrical – dominantly p-type electronic - conductivity is presented in Figure 3.7 [28].

The conductivity curve (Figure 3.7) is at a maximum at ~450 °C. Above this temperature, the conductivity decreases with the increasing temperature because the concentration of electron holes decreases. Below this temperature, the conductivity increases as the temperature increases, since the mobility of holes dominates.

Introducing dopants on the A- and/or B-site in different concentration is one way of trying to improve the desired transport properties of LNO and at the same time increase the stability of the material. The substitution of one or both cations in LNO has been extensively investigated [29-33]. The most commonly chosen substituents are Sr for the A-site and Cu or Co for the B-site. However, investigations showed that oxygen permeation remains highest for nominally pure LNO [9], and conductivity increases with the Sr substitution of La, while oxygen permeation decreases due to the decrease in the concentration of oxygen interstitials. Cu substitution decreases the sintering temperature as well as oxygen permeation [29], due to a decrease in the concentration of oxygen interstitials.

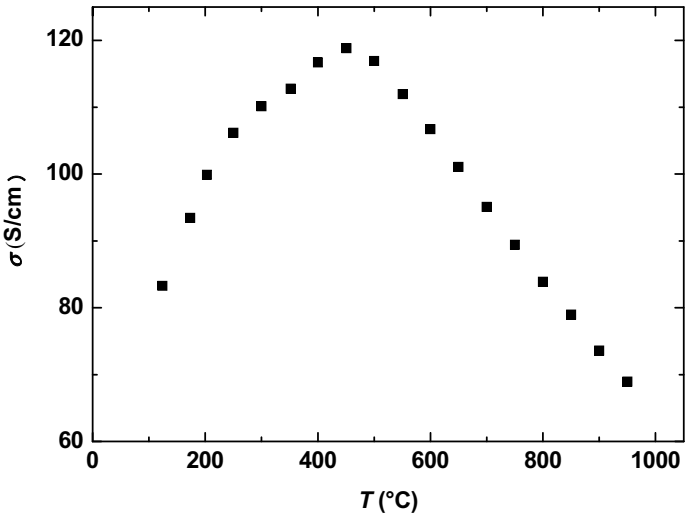

Figure 3.7. Measured electric conductivity in air based on [28].

3.5 References:

[1] J.G. Bednorz, K.A. Müller, "*Possible high Tc superconductivity in the barium-lanthanum-copper-oxygen system*", *Zeitschrift für Physik B: Condensed Matter*, 1986, 64, 189-193

[2] M. Matsuda, M. Fujita, K. Yamada, R. J. Birgeneau, M. A. Kastner, H. Hiraka, Y. Endoh, S. Wakimoto, G. Shirane, "*Static and dynamic spin correlations in the spin-glass phase of slightly doped $La_{2-x}Sr_xCuO_4$*", *Physical Review B*, 2000, 62(13), 9148.

[3] E.N. Naumovich, M.V. Patrakeev, V.V. Kharton, A.A. Yaremchenko, D.I. Logvinovich, F.M.B. Marques, "*Oxygen nonstoichiometry in $La_2Ni(M)O_{4+\delta}$ (M = Cu, Co) under oxidizing conditions*", *Solid state Sciences*, 2005, 7, 1353-1362.

[4] V. V. Kharton, A. P. Viskup, A. V. Kovalevsky, E. N. Naumovich, F. M. B. Marques, "*Ionic transport in oxygen-hyperstoichiometric phases with K_2NiF_4-type structure*", *Solid State Ionics*, 2001, 143(3,4), 337-353.

[5] V. V. Vashook, I. I. Yushkevich, L. V. Kokhanovsky, L. V. Makhnach, S. P. Tolochko, I. F. Kononyuk, H. Ullmann, H. Altenburg, "*Composition and conductivity of some nickelates*", *Solid State Ionics*, 1999, 119, 23-30.

[6] V. V. Kharton, A. P. Viskup, E. N. Naumovich, F. M. B. Marques, "*Oxygen ion transport in La_2NiO_4-based ceramics* ", *Journal of Materials Chemistry*, 1999, 9, 2623-2629.

[7] A. Aguadero, M. Pérez, J. A. Alonso, L. Daza, "*Neutron powder diffraction study of the influence of high oxygen pressure treatments on $La_2NiO_{4+\delta}$ and structural analysis of $La_2Ni_{1-x}Cu_xO_{4+\delta}$ $(0 \leq x \leq 1)$*", *Journal of Power Sources*, 2005, 151, 52-56.

[8] E. Boehm, J.M. Bassat, M. C. Steil, P. Dordor, F. Mauvy, J. C. Grenier, "*Oxygen transport properties of $La_2Ni_{1-x}Cu_xO_{4+\delta}$ mixed conducting oxides*", *Solid State Sciences*, 2003, 5, 973-981.

[9] J. B. Smith, T. Norby, "*On the steady-state oxygen permeation through $La_2NiO_{4+\delta}$ membranes*", *Journal of the Electrochemical Society*, 2006, 153(2), A233-A238.

[10] J. M. Bassat, P. Odier, A. Villesuzanne, C. Marin, M. Pouchard, "*Anisotropic ionic transport properties in $La_2NiO_{4+\delta}$ single crystals*", *Solid State Ionics*, 2004, 167, 341-347.

[11] C. Frayret, A. Villesuzanne, M. Pouchard, "*Application of Density Functional Theory to the Modelling of the Mixed Ionic and Electronic Conductor $La_2NiO_{4+\delta}$: Lattice Relaxation, Oxygen Mobility, and Energetics of Frenkel Defects*", *Chemistry of Materials*, 2005, 17, 6538-6544.

[12] W. Paulus, A. Cousson, G. Dhalenne, J. Berthon, A. Revcolevschi, S. Hosoya, W. Treutmann, G. Heger, R. Le Toquin, "*Neutron diffraction studies of stoichiometric and oxygen intercalated La_2NiO_4 single crystals*", *Solid State Sciences*, 2002, 4, 565-573.

[13] J. D. Jorgensen, B. Dabrowski, S. Pei, D. R. Richards, D. G. Hinks, "*Structure of the interstitial oxygen defect in lanthanum nickel oxide ($La_2NiO_{4+\delta}$)*", *Physical Review B*, 1989, 40, 2187-2199.

[14] L. Minervini, R. W. Grimes, J. A. Kilner, K. E. Sickafus, "*Oxygen migration in $La_2NiO_{4+\delta}$*", *Journal of Materials Chemistry*, 2000, 10, 2349-2354.

[15] S. J. Skinner, "*Characterisation of $La_2NiO_{4+\delta}$ using in-situ high temperature neutron powder diffraction*", *Solid State Science*, 2003, 5, 419-426.

[16] M. Schroeder, M.-A. Dragan, "*Oxygen transport in $La_{2-x}Sr_xNiO_{4+\delta}$: membrane permeation and defect chemical modelling*", *Journal of Materials Science*, 2007, 42, 1972-1983.

[17] A. Aguadero, J. A. Alonso, M. J. Martinez-Lope, M. T. Fernández-Diaz, M. J. Escudero, L. Daza, "*In-situ high temperature neutron powder diffraction study of oxygen-rich $La_2NiO_{4+\delta}$ in air: correlation with the electrical behaviour*", *Journal of Materials Science*, 2006, 16, 3402-3408.

[18] M. S. D. Read, M. S. Islam, F. King, F. E. Hancock, "*Defect Chemistry of $La_2Ni_{1-x}M_xO_4$ (M = Mn, Fe, Co, Cu): Relevance to Catalytic Behaviour*", *Journal of Physical Chemistry B*, 1999, 103, 1558-1562.

[19] J. B. Smith, *"Mixed oxygen ion/electron conductors for oxygen separation processes: Surface kinetics and cation diffusion"*, Ph. D. Thesis (2005), Faculty of Mathematics and Natural Sciences, University of Oslo, Norway.

[20] Z. Li, R. Haugsrud, J. B. Smith, T. Norby, "*Transport properties and defect analysis of $La_{1.9}Sr_{0.1}NiO_{4+\delta}$*", *Solid State Ionics*, 2009, 180, 1433-1441.

[21] S. J. Skinner, "*Diffusion and defects in oxides with the K_2NiF_4 structure type*", *Advances in Science and Technology*, 2006, Vol. 46, 174-179.

[22] J. A. Kilner, C. K. M. Shaw, "*Mass transport in $La_2Ni_{1-x}Co_xO_{4+\delta}$ oxides with the K_2NiF_4 structure*", *Solid State Ionics*, 2002, 154-155, 523-527.

[23] S. J. Skinner, J. A. Kilner, "*Oxygen diffusion and surface exchange in $La_{2-x}Sr_xNiO_{4+\delta}$*", *Solid State Ionics*, 2000, 135, 709-712.

[24] H. Schmalzried, *Chemical Kinetics of Solids, Solid State Reactions*, Chapter 6, Verlag Chemie, Weinheim/Bergstr., 1974.

[25] N. Čebašek, R. Haugsrud, Z. Li, J. Milošević, J. B. Smith, A. Magrasó, T. Norby, "*Determination of the self-diffusion coefficient of Ni^{2+} in $La_2NiO_{4+\delta}$ by the solid state reaction method*", *Journal of the Electrochemical Society*, 2012, 159 (6) B702-B708.

[26] N. Čebašek, "*Determination of Chemical Tracer Diffusion Coefficients for the La- and Ni-site in $La_2NiO_{4+\delta}$ Studied by SIMS*", *to be submitted.*

[27] N. Čebašek, R. Haugsrud, T. Norby, "*Determination of inter-diffusion coefficients for the A- and B-site in the $A_2BO_{4+\delta}$ (A = La, Nd and B = Ni, Cu) system*", *submitted to Solid State Ionics*.

[28] Z. Li, unpublished data.

[29] F. Mauvy, E. Boehm, J. M. Bassat, J. C. Grenier, J. Fouletier, "*Oxygen permeation fluxes through $La_2Cu_{0.5}Ni_{0.5}O_{4+\delta}$ dense ceramics: Comparison with oxygen diffusion coefficients*", *Solid State Ionics*, 2007, 178, 1200-1204.

[30] P. J. Heaney, A. Mehta, G. Sarosi, V. E. Lamberti, A. Navrotsky, "*Structural effects of Sr substitution in $La_{2-x}Sr_xNiO_{4+\delta}$*", *Physical Review B*, 1998, 57, 10370-10378.

[31] V.V. Kharton, E. V. Tsipis, A. A. Yaremchenko, J. R. Frade, "*Surface-limited oxygen transport and electrode properties of $La_2Ni_{0.8}Cu_{0.2}O_{4+\delta}$*", *Solid State Ionics*, 2004, 166, 327-337.

[32] Z. Li, R. Haugsrud, J. B. Smith, T. Norby, "*Steady-State Permeation of Oxygen Through $La_{1.9}Sr_{0.1}NiO_{4+\delta}$*", *Journal of the Electrochemical Society*, 2009, 156, B1039-B1044.

[33] T. Nakamura, K. Yashiro, K. Sato, J. Mizusaki, "*Electronic state of oxygen nonstoichiometric $La_{2-x}Sr_xNiO_{4+\delta}$ at high temperatures*", *Physical Chemistry Chemical Physics*, 2009, 11, 3055-3062.

4. Methodology and selected results

During the investigation of cation diffusion in $La_2NiO_{4+\delta}$ (LNO) the experimental work involved synthesis, fabrication of samples, annealing experiments, and later instrumental analyses. A wet chemical (citric acid) route was used to synthesise compounds and is described in more detail in the papers yet to be published. The details of the fabrication of the samples, including the preparation of powders, pressing tablets, sintering and polishing, as well as experimental setups are also explained in the papers yet to be published.

The sample analyses involved the use of heavy instrumentation as required by the experimental techniques, such as Scanning Electron Microscopy (SEM) with Energy-dispersive X-ray spectroscopy (EDX) for the solid state reaction experiment, Secondary Ion Mass Spectrometry (SIMS) for the tracer experiment, and Electron Probe Micro Analysis (EPMA) for the inter-diffusion experiment. Besides these "major" instruments/techniques, some other supplemental techniques were used: for the determination of the grain size and microstructure of the samples (Electron Backscatter Diffraction (EBSD)), for compound identification after synthesis (X-ray diffraction (XRD)) and the determination of composition at the surface after the decomposition experiment (X-ray photoelectron spectroscopy (XPS)).

4.1 Solid state reaction

In the solid state reaction technique (SSR) for the determination of the self-diffusion coefficient of the fastest moving species, two sintered polished samples of NiO and La_2O_3 were pressed together in a spring load (Figure 4.1) and subsequently annealed at different temperatures for various annealing times. After annealing, the diffusion couples were mounted in epoxy resin, cut perpendicular to the samples surface, and the thickness of the reaction product layer was measured.

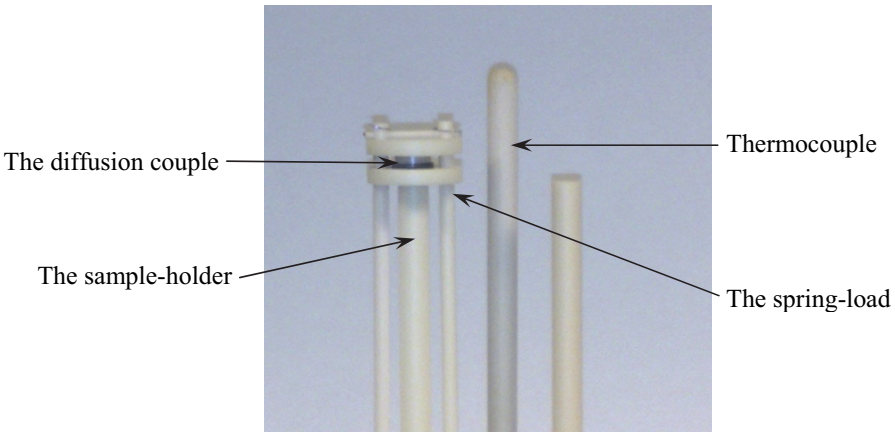

Figure 4.1. Diffusion couple between NiO and La_2O_3, mounted in spring load.

4.1.1 Scanning electron microscopy and energy-dispersive X-ray spectroscopy

Scanning electron microscopy is a type of electron microscopy which uses a high energy beam (1-30 keV) of electrons in a raster scan[1] pattern for scanning the sample surface in order to obtain its enlarged image [1]. The high energy beam of electrons "lightens" the surface of the sample and interacts with its atoms which create signals containing information about surface topography, composition and some other properties, e.g. electrical conductivity.

When electrons strike the sample surface through the interaction as mentioned above, three types of signals are produced: X-rays, electrons (secondary and backscattered electrons) and photons [3]. The main detector system (the Everhart-Thornley detector) picks up the secondary electrons (SE), then amplifies them and finally converts them into electrical voltage before sending them to the terminal screen. In this manner SEM can produce images with very high resolution in a digital format, achieving magnifications of over 100000 ×s. The principle of SEM imaging is schematically shown in Figure 4.2.

[1] A **raster scan**, or **raster scanning**, is the rectangular pattern of image capture and reconstruction at the screen [2].

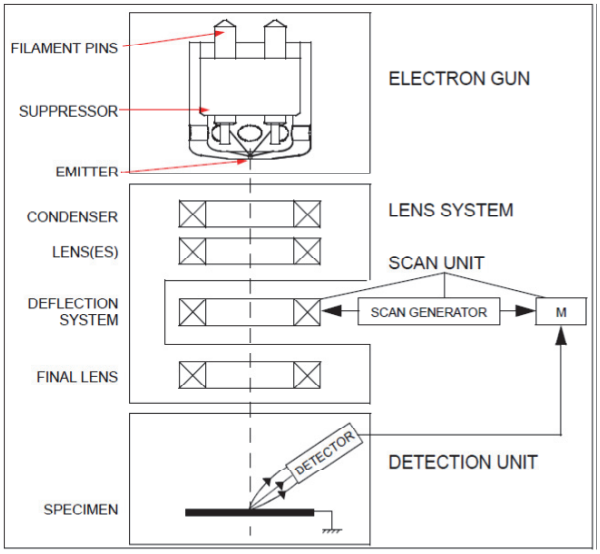

Figure 4.2. SEM schematic overview, according to [3]

Backscattered electrons (BSE) are produced by elastic scattering of electrons from the sample surface [1]. A qualitative image of the distribution of different phases (the chemical composition) can be obtained by using BSE, as BSE signal intensity is strongly related to the atomic number (Z) of the given element.

The scanning electron microscope (SEM) used in this work is a Quanta FEG 200, FEI. The Energy-dispersive X-ray spectroscopy (EDX or EDS) system is an auxiliary feature of the SEM instruments and an analytical technique used for semi-quantitative chemical characterisation of a sample [4, 5]. The SEM is equipped with an Ametek EDAX EDX system with GENESIS Spectrum Ver. 5.11 software for spectrum collection, peak identification and quantitative analysis, line scanning, and mapping.

The quantification feature of the EDX system can perform standardless quantification, quantification using standards or quantification using quantification options based on sample characteristics. The most commonly used is the standardless quantification, providing a fast quantification of the analysed sample with automatic background subtraction, matrix correction, and normalisation to 100% for all of the elements in the peak identification list. The samples analyses for the quantification of composition in this work used the standardless quantification.

The software package of the Quanta FEG 200 microscope also contains XT Docu 3.2 (Build 607), (FEI Company) software. This software has numerous possibilities, such as the measurement of horizontal, vertical and random distances, calculation of the required area, etc. The measurement distance feature of this software was used for the determination of the reaction layer product in the SSR experiment.

Our Quanta FEG 200 also has other features, such as electron backscatter diffraction (EBSD). This feature will be explained in more detail in further text.

4.1.2 Examples and measurement results

After examining the diffusion couples between NiO and La_2O_3 in SEM typical images were obtained as shown in Figure 4.3.

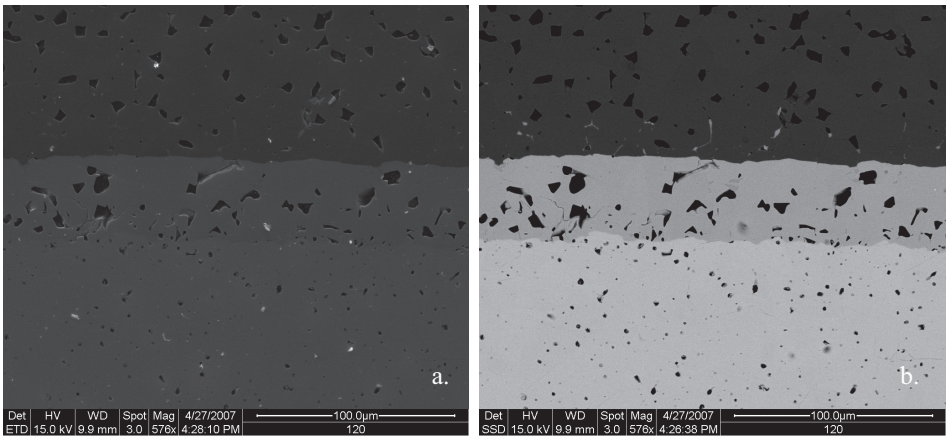

Figure 4.3. Typical SEM images of the diffusion couples between NiO (top) and La_2O_3 (bottom) and the reaction layer of LNO between them. The Everhart-Thornley for SE (a) and Soli State detector for BSE (right). High contrast in the BSE image (b) indicates different phases, i.e., different chemical composition.

The composition of the reaction product was checked (confirmed) by EDX and its spectrum is shown in Figure 4.4. The single phase product was confirmed. The ratio between La and Ni determined by the EDX quantification software also verified the composition of LNO.

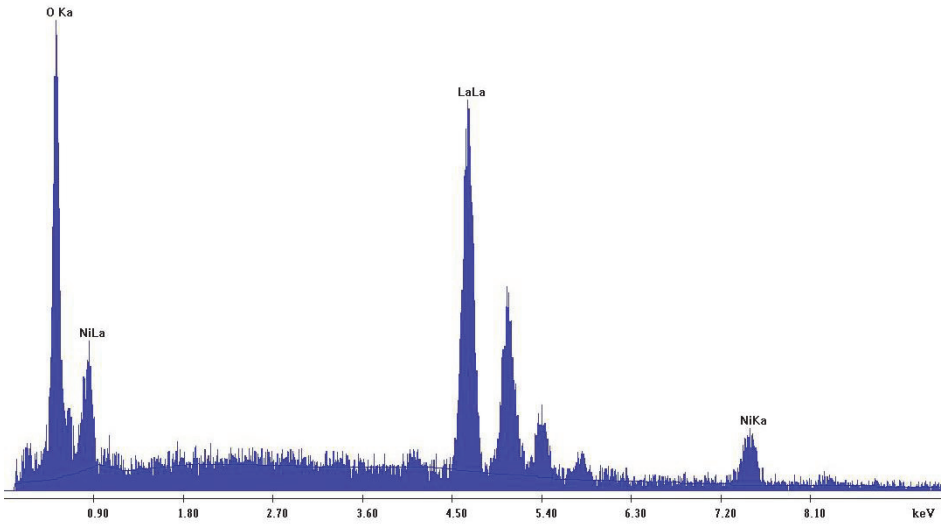

Figure 4.4. EDX spectrum, showing all abundant elements (La, Ni and O) in the LNO reaction product.

4.2 Chemical tracer diffusion

Using the chemical tracer diffusion technique we can obtain the chemical tracer diffusion coefficient related to the self-diffusion coefficient through the Einstein-Smoluchowski relation as explained above (Eq. 2.10). The experimental performance of this technique involves applying the tracer on the polished surface sintered samples of the examined material and subsequent annealing at various temperatures for different periods. Annealed samples were then analysed by means of SIMS for the chemical tracer diffusion depth (depth profiles). In this work, Pr, Nd and Co were used as chemical tracers rather than stable or radioactive isotopes of La and Ni considering safety and price.

4.2.1 Secondary ion mass spectrometry

Secondary ion mass spectrometry is an analytical method used for the determination of elements present in solid materials, particularly on surfaces or thin-films, with sensitivity in the trace range (ppb level) and high spatial resolution [6, 7, 8]. SIMS uses a focused primary ion beam for sputtering atoms and a small fraction of ions from the surface, where only the latter (secondary ions – SI) are analysed by the mass spectrometer. A scheme of the sputtering process is given in Figure 4.5.

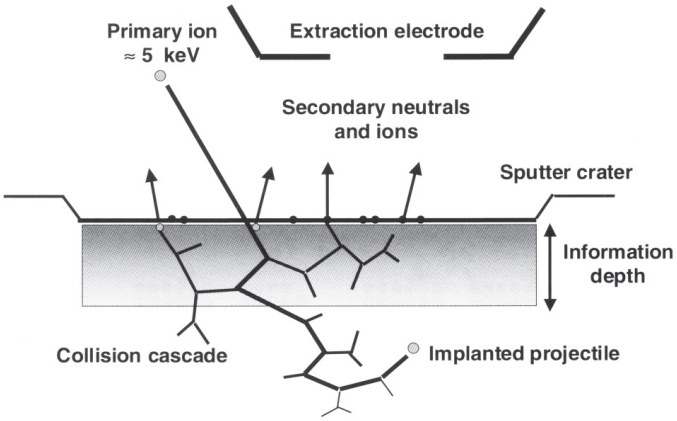

Figure 4.5. The sputtering process scheme, according to [7].

The primary ion beam can have an energy of 0.25 to 30 keV. Most SIMS instruments use the primary ions of Cs^+, O_2^+, Ar^+, Xe^+ and Ga^+ and recently also the Bi and Au cluster ions (Au_n^{z+}, Bi_n^{z+}) and C_{60}^+ [6]. When the primary ions impact the solid material they transfer their kinetic energy through collision to the atoms of the target and displace them from their original position. The displaced atoms will eventually collide in a collision cascade until some of them reach the surface and further eject from the top two or three monolayers. As mentioned above, most of the emitted particles are neutral, but some of them are charged (secondary ions). Those emitted (created) secondary ions move scattered in all directions from the sample surface. They are collected from the sample surface by the imposed electrical bias of several kV between the sample surface and the extraction electrode [7]. After extraction, the SI are transported via a series of electrostatic and magnetic lenses to the mass spectrometer. The mass spectrometers are equipped with either quadrupole filters or electric and magnetic sector fields. Schematic representation of the SIMS instrument is given in Figure 4.6.

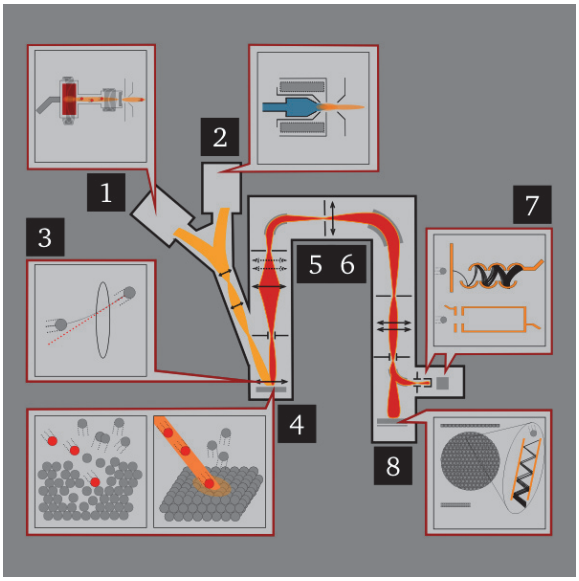

Figure 4.6. A scheme of the SIMS instrument, according to [8]. Primary high energy ions are produced in the ion gun (1 or 2) and focused onto the sample surface (3), where sputtering occurs and atoms and secondary ions are produced. After and during the sputtering SI are collected by ion lenses (5) and filtered according to atomic mass (6), projected on to an electron multiplier (7 top), a Faraday cup (7 bottom), or to the CCD screen (8).

The quantification process of converting SI intensity into a concentration can be described with the following equation

$$i_{\mathrm{A}}^{\mathrm{s}} = I^{\mathrm{p}} Y \alpha_{\mathrm{A}} \eta_{\mathrm{A}} \theta_{\mathrm{A}} x_{\mathrm{A}} \qquad \textbf{4.1}$$

where $i_{\mathrm{A}}^{\mathrm{s}}$ is the measured secondary ion intensity, I^{p} is the primary ion intensity (ions/s), Y is the sputter yield (removed target atoms per incident primary ion), α_{A} is the ionisation probability, η_{A} is the combined transmission efficiency of the extraction optics, the mass spectrometer and the detector, θ_{A} is the isotopic abundance, and x_{A} is the atomic fraction of element A [6].

Nowadays some SIMS instruments use Time-of-flight (TOF) spectrometers (TOF-SIMS instruments) which combine high lateral resolution (< 60 nm) with high depth resolution (<1 nm). The TOF-SIMS technique is widely used for the surface characterisation of solids [7].

The SIMS instrument used in this work was CAMECA ims 7f.

4.2.2 Examples and measurement results

After the analyses of a series of annealed samples with the chemical (impurity) tracers of Pr, Nd and Co, the example of depth profile's evolution with time is presented in Figure 4.7.

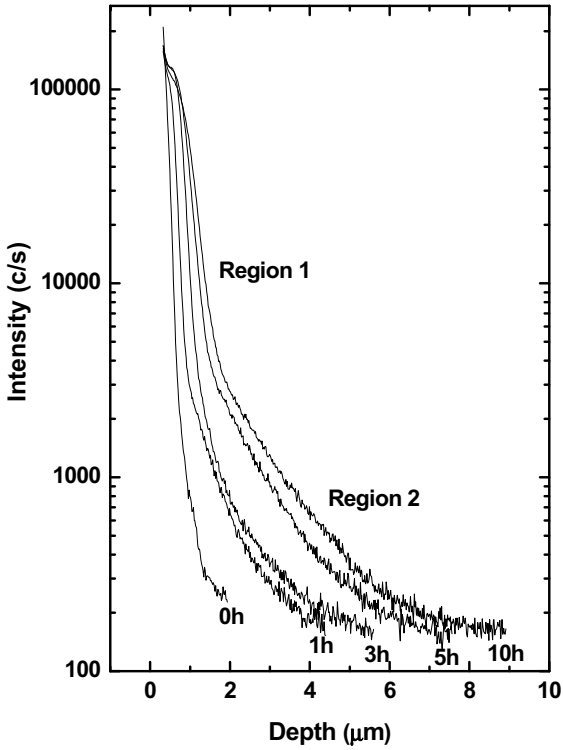

Figure 4.7. Typical series of depth profiles of Co chemical tracers into LNO. Samples were annealed for 0, 1, 3, 5 and 10 hours at 1100 °C.

During the sputtering process the primary ion beam erodes and creates a crater at the surface of the sample. The instrument used to determine the depth profile of the craters was Dektak 8 stylus. The SEM image and its profile are presented in Figure 4.8 (a and b).

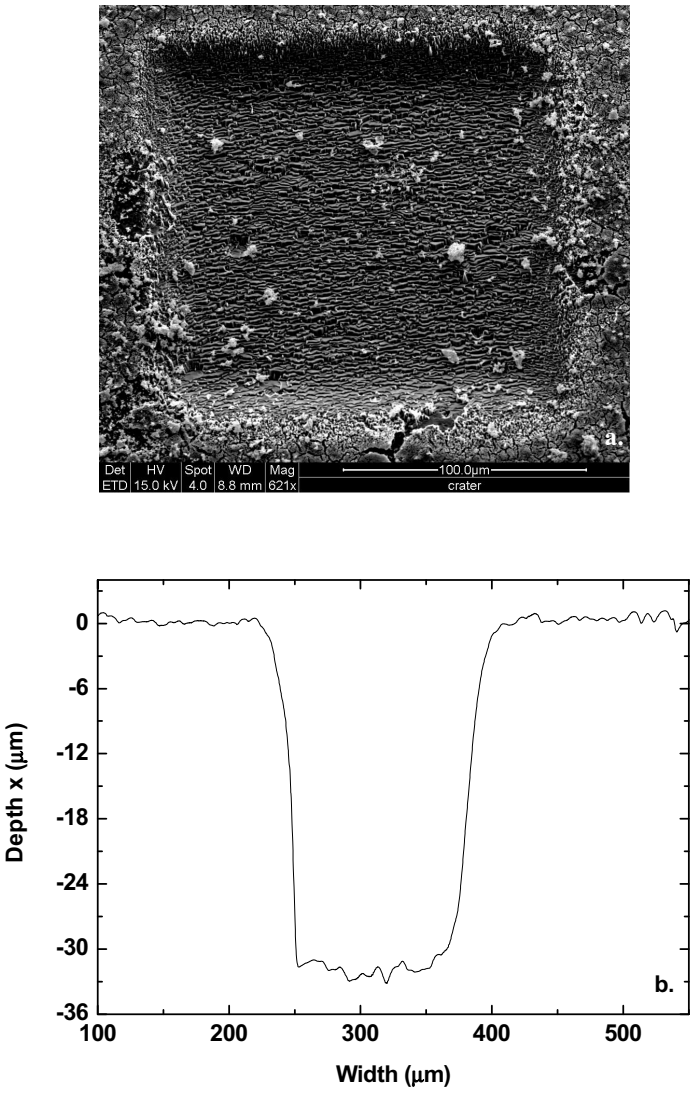

Figure 4.8. a. SEM image of the crater in the 5% Sr doped LNO with a visible Pr chemical (impurity) tracer layer and b. its depth profile.

4.3 Inter-diffusion

Chemical diffusion (inter-diffusion) coefficients are obtained by inter-diffusion measurement. Inter-diffusion was experimentally performed by pressing sintered and polished samples with spring load into a diffusion couple and subsequently annealing it at

various temperatures for different annealing times. After annealing, the diffusion couples were mounted in epoxy resin (Figure 4.9), cut parallel to the direction of diffusion and analysed by the EPMA instrument.

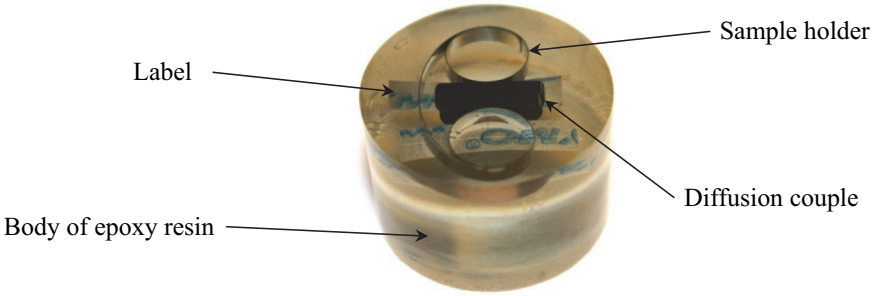

Figure 4.9. Inter-diffusion couple mounted and cut parallel to the direction of diffusion.

Cation diffusion in undoped and doped LNO was investigated by inter-diffusion couples.

4.3.1 Electron probe micro analysis

The inter-diffusion technique is a direct analytical method used for the determination of the chemical composition of a small volume of solid material and is a frequently used technique for the determination of the chemical diffusion (inter-diffusion) coefficient [7, 9]. The ability to determine the chemical composition results from the unique relationship between the wavelength of the characteristic X-rays (λ) and the atomic number (Z) and it was first observed by Moseley in 1913. He showed that for K radiation there is a simple relation given by [7]

$$Z \propto \frac{1}{\sqrt{\lambda}} \qquad \textbf{4.2}$$

Based on this relation, the EPMA instrument analyses the wavelengths of X-rays emitted from the sample after being bombarded by the electron beam. The X-rays' radiation is detected and characterised either by means of the Energy-dispersive X-ray spectrometer (EDX) or the crystal diffraction spectrometer – Wavelength-dispersive spectrometer (WDX). The sample chamber, electron gun, magnetic lenses and various detectors are maintained under high vacuum. Schematic representation of the EPMA instrument is given in Figure 4.10.

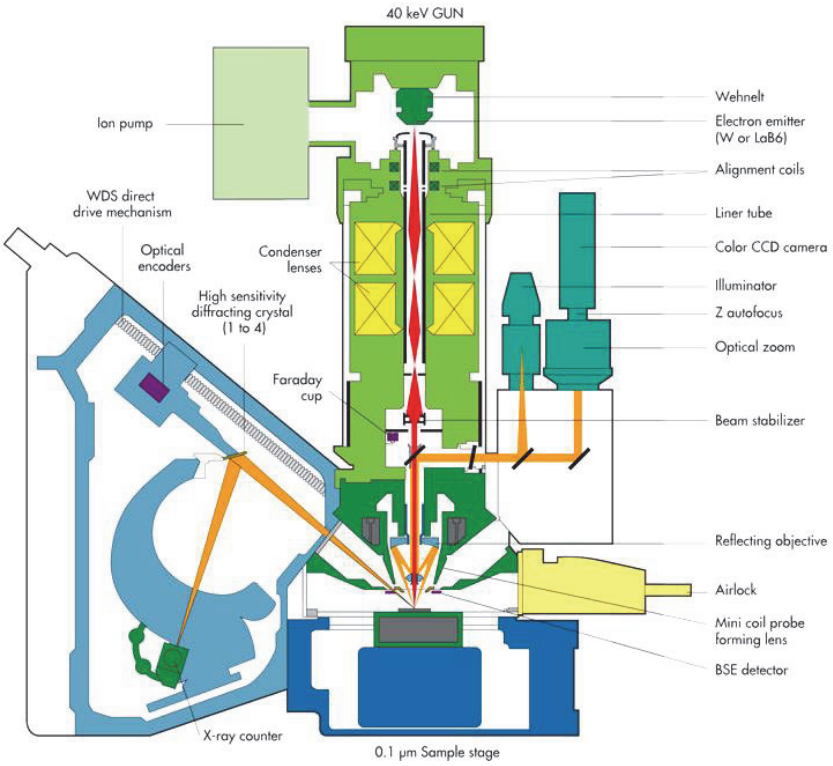

Figure 4.10. EPMA schematic overview, from [10].

The detection limits of the EMPA instrument used in this work, the Cameca SX 100, is about 10^{-3} to 10^{-4} in terms of atomic fractions, depending on the selected elements. For the analysis of inter-diffusion depth profiles, error functions and the Boltzmann-Matano method are usually employed [7].

The calibration standards for the examined elements by EPMA, are given in the following papers yet to be published.

4.3.4 Examples and measurement results

Inter-diffusion couples for the evaluation of cation diffusion in LNO were line scanned in order to obtain the diffusion profile of the examined cations and mapped in order to determine the distribution of the corresponding cations (Figure 4.11 and 4.12).

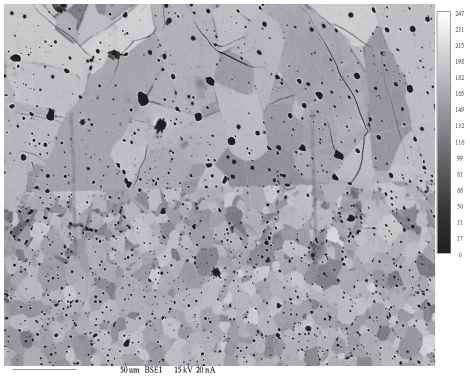

Figure 4.11. BSE image of the inter-diffusion couples between LNO and $La_2CuO_{4+\delta}$ with the visible marks after the line scanning.

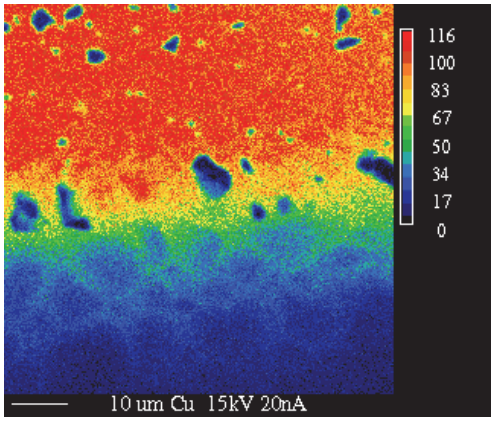

Figure 4.12. Mapping of the area around the contact surface of the LNO and $La_2CuO_{4+\delta}$ samples, showing the distribution of Cu ions into the LNO, indicating grain boundary diffusion.

4.4 Complementary techniques

In addition to the main techniques used for SSR – the chemical tracer diffusion and inter-diffusion experiments – there were some complementary techniques employed for their characterisation and surface analysis. The composition of all synthesised compounds used in this work was examined by means of XRD. Grain size was determined in some of the samples. For this purpose, the special feature of SEM – EBSD – was used. After the LNO membrane was exposed to the gradient of pO_2 (described in the Paper IV), both surfaces were examined by means of XPS, in addition to the analyses by SEM, XRD and EPMA.

4.4.1 X-ray diffraction

X-ray diffraction is an analytical technique that gives information on chemical composition, crystallographic structure, etc, by observing the intensity of a scattered X-ray beam after it hits the examined sample surface. The intensity of the scattered X-ray beam is a function of incident and scattered angle, polarization, and wavelength or energy [11, 12]. When a sample is bombarded with an X-ray, it is diffracted from the arrays of atoms in the crystal due to Bragg's law. The diffracted beam is detected and gives characteristic so called XRD patterns. Based on these patterns it is possible to determine cell parameters. The XRD instrument used in this work is the Simens D-5000.

Figures 4.13 and 4.14 show the XRD patterns of $Nd_2NiO_{4+\delta}$ and $La_2CuO_{4+\delta}$, used in the inter-diffusion experiment. Based on these patterns, it can be seen that single phase products were obtained, as for all other synthesised compounds used in this thesis.

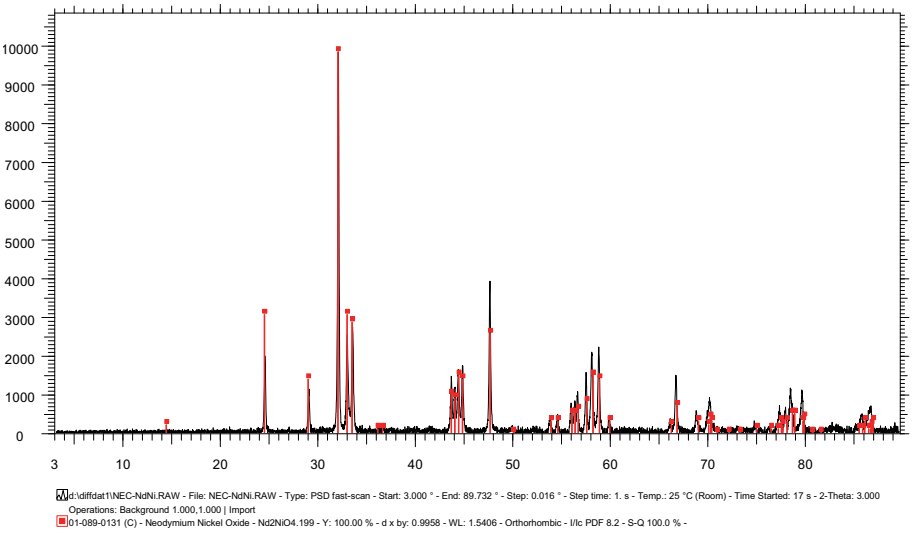

Figure 4.13. The XRD pattern of $Nd_2NiO_{4+\delta}$.

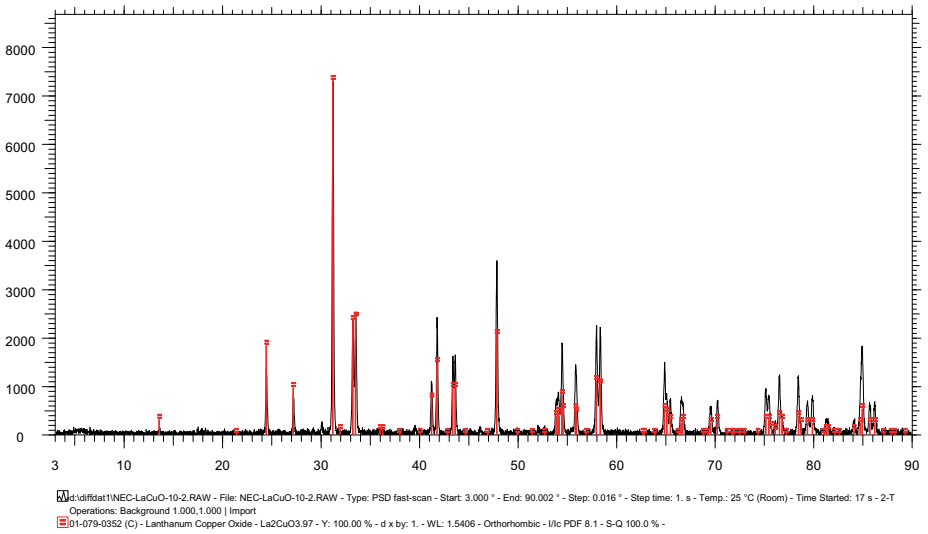

Figure 4.14. The XRD pattern of $La_2CuO_{4+\delta}$.

4.4.2 Electron backscatter diffraction

Electron backscatter diffraction is another auxiliary feature of SEM and it is a characterisation technique that can provide information about individual grain orientations, local textures, point-to-point orientation correlations, and phase identification and distribution. EBSD employs the backscatter diffraction of a stationary beam of high energy electrons from a volume of crystal material approximately 20 nm deep in the specimen to obtain the so called backscattered Kikuchi (or EBSD) (BKP) patterns [13]. The BKP have a characteristic regular arrangement of parallel bright bands on a steep continuous background, as shown in Figure 4.15.

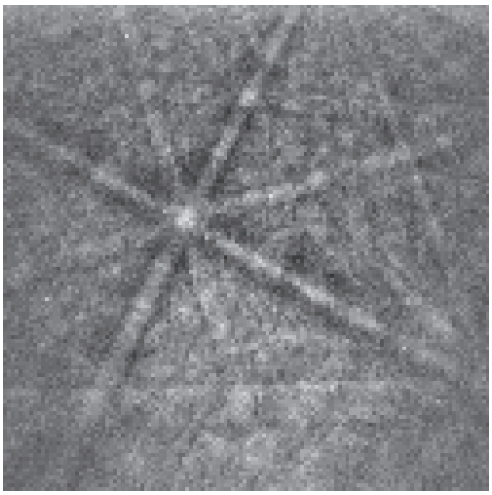

Figure 4.15. Backscatter Kikuchi pattern from LNO, after background subtraction.

The quality of the BKP depends largely on the quality of the sample surface, i.e., its preparation (polishing). The examined samples in this work were polished using a diamond abrasive down to 1/4 of a micrometer (Struers, DP-spray P, Struers, Denmark). This Kikuchi pattern is generated on a phosphorus screen and it can be said that it represents the gnomonic projection of the crystal lattice [13]. In order to detect the bands in the BKP an image processing algorithm (Hough Transform) is used. The pattern can be indexed by comparing the angles between the detected bands to the theoretical look-up-table [14]. It can generate the so called Image Quality (IQ) which gives information on the microstructure and the Inverse Pole Figure (IPF) which gives information on the grain's orientation. IQ and IPF images in Figure 4.16 provide information about the phases, grain size and grain orientation of the cross-section of the diffusion couple used in the SSR experiment. Another example in Figure 4.17 is the EBSD micrograph of the polished surface of the sintered LNO sample. Figure 4.17a shows the grain orientation and 4.17b shows the grain size distribution of the scanned area. The values obtained by EBSD scanning were averaged and corrected for flat plane observation multiplying by 1.35.

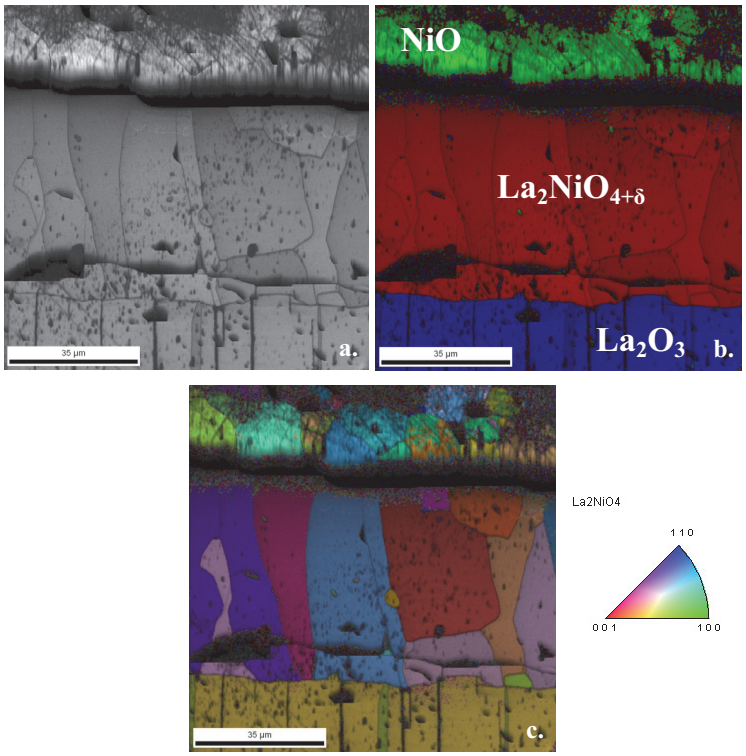

Figure 4.16. EBSD maps of the NiO and La_2O_3 diffusion couple cross-section with the reaction product layer LNO in between; a. is the IQ map of the diffusion couple showing the microstructure, b. is the combination of the IQ and phase map and c. is the combination of the IQ and IPF maps, showing the orientation of the grains.

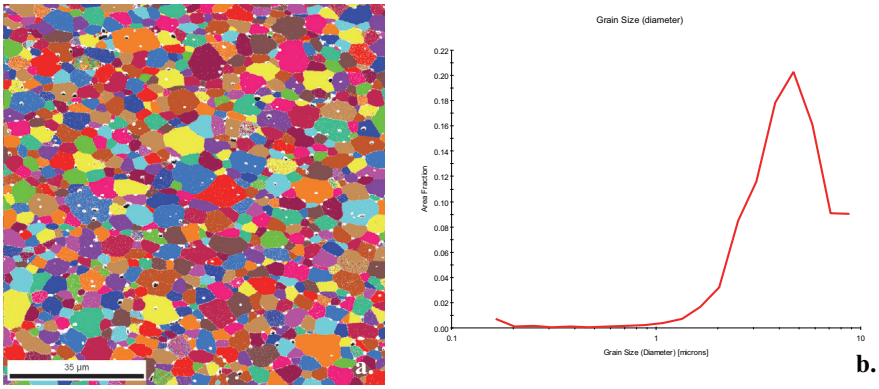

Figure 4.17. EBSD micrograph of the polished surface of sintered LNO. a. The combination of IQ and IPF maps, revealing the grain orientation, b. grain size graph showing grain size distribution versus area fraction, according to the map from a.

SEM (Quanta FEG 200) used in this investigation is equipped with the EBSD camera CD-200 Nordiff and the analysing software is EDAX, Orientation Imaging Microscopy v5 Analysis 5.2.

4.4.3 X-ray photoelectron spectroscopy

X-ray photoelectron spectroscopy is a surface quantitative analysis technique. It provides atomic and molecular information from the material's surface, e.g. chemical composition, valence and atomic bonding. The phenomenon of XPS is based on the photoelectric effect, meaning that the sample surface is irradiated with X-rays and its energy is directly transferred to surface atoms which cause the emission of electrons. The emitted electron energy can later be measured and characterised due to its unique energy value for each atomic species [15]. XPS measures 1 to 10 nm of the material from the surface. XPS requires measurement in ultra high vacuum [16].

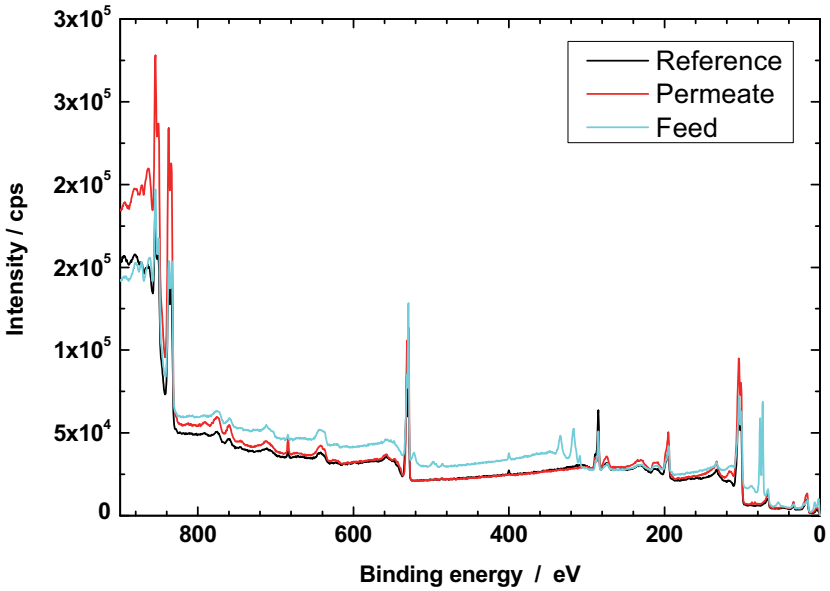

Figure 4.18. Survey scan spectrum of the LNO oxygen permeable membrane after exposure to the pO_2 gradient for 800 hours at 1000 °C.

XPS was used in this work to determine the composition on both sides (high and low pO_2) of the LNO membrane after being exposed to a pO_2 gradient at 1000 °C for 800 hours. The survey scan spectrum in Figure 4.18 shows that the membrane starts to walk-out (decompose) as the high pO_2 side of the membrane is enriched with Ni (this will be explained in more detail in the Paper IV). The instrument used for this analysis is the Kratos XPS/UPS Axis Ultra DDL.

4.5 Error calculations

Each experimental measurement has uncertainties due to the final precision of the measurement (e.g. errors due to instrumentation, methodology, the presence of confounding effects, etc). These uncertainties are determined by the combination of the represented variables in the demonstrated law. Based on the statistical probability distribution of the variables it is possible to derive the confidence limits of the measurement, which describe the region within which the true value of the variable should be found with a level of certainty [17, 18]. The uncertainties usually have two components, one related to accuracy and the other an unavoidable random variation that occurs when performing repeated measurement. As all measurements have uncertainties related to accuracy in addition to the random variations due to repeated measurement, those two factors are the bases for further calculation into the uncertainty of the derived quantity. In statistics uncertainty analysis is called the propagation of errors [19]. In the analysis of uncertainties numerous techniques can be used to determine the reliability of model predictions, accounting for various sources of uncertainty in model input and design.

As a general example for the given $X = f(A_1, A_2, A_3, ...)$ we can write the basic formula for the absolute error of independent observables for X^2

$$\Delta X^2 = \left|\frac{\partial f}{\partial A_1}\right|^2 \cdot \Delta A_1^2 + \left|\frac{\partial f}{\partial A_2}\right|^2 \cdot \Delta A_2^2 + \left|\frac{\partial f}{\partial A_3}\right|^2 \cdot \Delta A_3^2 + ... = \sum_{i=1}^{p} \left|\frac{\partial f}{\partial A_i}\right|^2 \cdot \Delta A_i \qquad \textbf{4.3}$$

where $\partial f / \partial A_i$ represents the partial derivatives of the function X with respect to one of the variables A which affects this function.

As an experimental example, the error calculation in the SSR experiment is explained in more depth in further text. In this experiment the sintered and polished samples of La_2O_3

and NiO were pressed together into a diffusion couple. During annealing LNO was formed as a reaction product layer. The diffusion couple is then cut perpendicular to its interfaces and the reaction product layer thickness was measured (Figure 4.19).

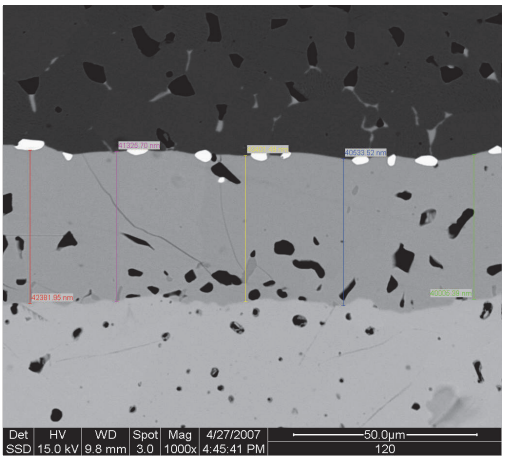

Figure 4.19. Example of measuring the thickness of the reaction product layer after annealing for 120 h at 1350 °C. The white spots are platinum markers.

The thickness of the reaction product layer is used to calculate the parabolic rate constant, and then the diffusion coefficient of the fastest species can be calculated using the Wagner's law of parabolic growth (Eq. 2.28). The thickness of the product layer was measured at 60-100 locations for each annealing and the average value was used for further calculation. The uncertainties of the measurements (error bars) were determined by taking into account the following contributors: the standard deviation (σ) for the mean product layer thickness, the error of visual determination (V) which depends on the microscope's image feature, and the error of magnification (I) of the microscope itself. The y-axis uncertainties were calculated by the following formula

$$\Delta = \sqrt{\sigma^2 + V^2 + I^2} \qquad \textbf{4.4}$$

The standard deviations are based on the fluctuation of the reaction product thickness from all measurements for each point, respectively. Visual errors are estimations based on the resolution of the measuring equipment software, depending on the magnification for each point, respectively. The error of the instrument is given by the manufacturer and is

maximum 1%. The *x*-axis error bars represent the uncertainty in the effective time of annealing (approximately ± 0.2 hours) at the nominal dwell temperature.

By fitting the experimental results of the reaction product layer thickness versus time, the parabolic rate constant (k_p) is obtained as a fit parameter together with its error. This error is used for further calculation of uncertainties. In this and the following steps, uncertainties (represented by the corresponding error bars) were calculated as the first partial derivative of the equation used for the calculation of the respective variable. When k_p errors are calculated they show the usual exponential growth (Figure 4.19). The respective error is obtained by each subsequent fitting. As mentioned above, this method in statistics is called the propagation of errors, as each error is adds up in the following fitting step, so the error increases.

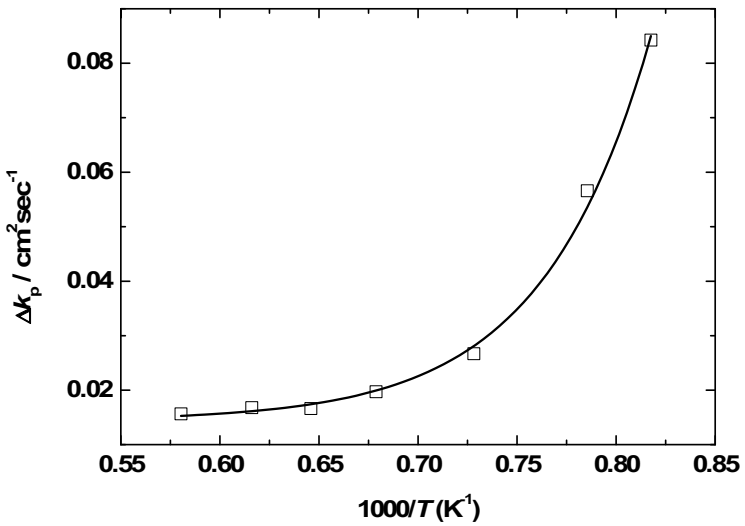

Figure 4.19. Exponential growth of the calculated errors for the k_p versus the inverse temperature for SSR between La_2O_3 and NiO.

In the following step, using the values for k_p, the diffusion coefficients at corresponding temperatures were calculated. The uncertainties of the diffusion coefficients were calculated as the first derivation of their expressions. The activation energy for the diffusion is obtained from the Arrhenius plots together with its errors. As the activation

energies are obtained from the slopes of the Arrhenius plot of the self-diffusion coefficient, the uncertainties of activation energy correspond to the errors of the fit parameters. However, as the value of $D_{Ni^{2+}}$ follows a strict linear dependence, the above mentioned uncertainties originate from the errors of the actual values corresponding to the uncertainties of k_p, activation energy (E_a), the standard Gibbs free energy change at the experimental temperature (ΔG_T°).

The calculation of errors in the SSR experiment represents the most complex procedure of all the experiments conducted in this work. All other experiments have simpler procedures for error calculation by calculating the first derivation of the applied equations for the respective techniques.

4.6 References:

[1] http://en.wikipedia.org/wiki/Scanning_electron_microscope.

[2] http://en.wikipedia.org/wiki/Raster_scan.

[3] FEI Company, *The Quanta FEG 200, 400, 600, User's Operation Manual*, 2003.

[4] EDAX, *Genesis Spectrum, User's Manual*, 2003.

[5] http://en.wikipedia.org/wiki/Energy-dispersive_X-ray_spectroscopy.

[6] R. A. De Souza, M. Martin, "*Secondary ion mass spectrometry (SIMS) - a powerful tool for studying mass transport over various length scales*", *Phys. Stat. sol.*, 2007, (c) 4, No. 6, 1785-1801.

[7] H. Mehrer, *Diffusion in Solids; Fundamentals, Methods, Materials, Diffusion-Controlled Processes*, Springer-Verlag Berlin Heidelberg, 2007.

[8] http://en.wikipedia.org/wiki/Secondary_ion_mass_spectrometry.

[9] http://en.wikipedia.org/wiki/Electron_microprobe.

[10] http://www.cameca.com/instruments-for-research/sx100.aspx.

[11] http://en.wikipedia.org/wiki/X-ray_crystallography.

[12] http://en.wikipedia.org/wiki/X-ray_scattering_techniques.

[13] A. J. Schwartz, M. Kumar, B. L. Adams, D. P. Field, *Electron Backscatter Diffraction in Materials Science*, Springer, New York, USA, 2000.

[14] EDAX, TSL, *TSL Operator's School*, *Course Manual*, "*A Systematic Study of Sample Preparation Techniques for EBSD*" by Ron Witt, 2005.

[15] H. R. Verma, *Atomic and Nuclear Analytical Methods, XRF, Mössbauer, XPS, NAA and B63 Ion-Beam Spectroscopic Techniques*, Springer-Verlag, Berlin, Heidelberg, 2007, Chapter 5.

[16] http://en.wikipedia.org/wiki/X-ray_photoelectron_spectroscopy.

[17] http://en.wikipedia.org/wiki/Propagation _of_uncertainity.

[18] http://en.wikipedia.org/wiki/Uncertainty_analysis

[19] http://en.wikipedia.org/wiki/Experimental_uncertainty_analysis.

5. Papers

List of Papers:

5.1 Paper I **Determination of Inter-Diffusion Coefficients for the A- and B-site in the $A_2BO_{4+\delta}$ (A = La, Nd and B = Ni, Cu) System**

Submitted to *Solid State Ionics*
Authors: *Nebojša Čebašek , Reidar Haugsrud, Truls Norby*

5.2 Paper II **Determination of Chemical Tracer Diffusion Coefficients for the La- and Ni-site in $La_2NiO_{4+\delta}$ Studied by SIMS**

Manuscript
Author: *Nebojša Čebašek*

5.3 Paper III **Determination of the Self-Diffusion Coefficient of Ni^{2+} in $La_2NiO_{4+\delta}$ by the Solid State Reaction Method**

Journal of the Electrochemical Society, 159 (6) B702-B708 (2012)
Authors: *Nebojša Čebašek, Reidar Haugsrud, Jovan Milošević, Zuoan Li, Jens B. Smith, Anna Magrasó, Truls Norby*

5.4 Paper IV **Kinetic Decomposition of $La_2NiO_{4+\delta}$ Membrane under an Oxygen Potential Gradient**

Accepted in the *Journal of the Electrochemical Society*
Authors: *Nebojša Čebašek, Truls Norby, Zuoan Li*

5.1 Paper I

Determination of Inter-Diffusion Coefficients for the A- and B-site in the $A_2BO_{4+\delta}$ (A = La, Nd and B = Ni, Cu) System

Authors: *Nebojša Čebašek , Reidar Haugsrud, Truls Norby*

Submitted to *Solid State Ionics*

Determination of Inter-Diffusion Coefficients for the A- and B-site in the $A_2BO_{4+\delta}$ (A = La, Nd and B = Ni, Cu) System

Nebojša Čebašek, Reidar Haugsrud, Truls Norby

University of Oslo, Department of Chemistry, Centre for Materials Science and Nanotechnology, FERMIO, Gaustadalleen 21, NO-0349 Oslo, Norway

Abstract

A- and B-site cation diffusion in the $La_2NiO_{4+\delta}$ system was investigated by, respectively, $La_2NiO_{4+\delta}$-$Nd_2NiO_{4+\delta}$ and $La_2NiO_{4+\delta}$-$La_2CuO_{4+\delta}$ inter-diffusion couples, annealed 100-600 h in ambient air at 950-1300 °C. Concentration profiles of the inter-diffusing cations were obtained by means of Electron Probe Micro Analysis (EPMA) from cross-sections. These profiles were fitted to the solution of Fick's second law for constant source and to Whipple-Le Claire's equation from which bulk and grain boundary diffusion coefficients, respectively, were derived. The diffusivity of A- and B-site cations in the grain interiors (bulk) are essentially comparable, while grain boundary diffusion of the B-site cations is enhanced, around 5 orders of magnitude at the investigated temperature range. Element mapping of the cross-sections of $La_2NiO_{4+\delta}$-$La_2CuO_{4+\delta}$ couples visualises the enhanced grain boundary diffusion of B-site cations. The activation energies are 275 ±12 kJ/mol for A-site bulk diffusion, and 450 ±20 and 125 ±24 kJ/mol for B-site bulk and grain boundary diffusion, respectively, based on the La and Ni profiles in their respective inter-diffusion couples.

Keywords: Bulk diffusion, Grain boundary diffusion, Cation inter-diffusion, Electron Probe Micro Analysis.

1. Introduction

$La_2NiO_{4+\delta}$ (LNO) exhibits mixed oxide ion-electron conduction which makes it attractive as potential cathode materials for solid oxide fuel cells (SOFCs) for intermediate temperatures and as membranes for oxygen separation [1].

LNO exhibits high flux when used as an oxygen separation membrane [2]. A number of studies have been devoted to the transport properties [2-10] and structure [11-20] of undoped and doped LNO. Above 150 °C, LNO has a tetragonal K_2NiF_4-type structure with space group I4/mmm and can be regarded either as alternating perovskite $LaNiO_3$ and rock salt LaO layers along the *c*-axis or stacking of La_2O_2 double layers and NiO_2 sheets [21]. The defect structure is predominated by oxygen interstitials, accommodated in the rock-salt layer, charge compensated by electron holes associated with Ni-sites as Ni^{3+} [22]. The oxygen interstitial concentration (δ) can reach values as high as 0.25 in LNO.

The difference in the partial pressure of oxygen (pO_2) across the membrane is the driving force for the diffusion of oxide ions and holes toward the side with lower oxygen chemical potential (low pO_2-side). However, such gradients also act as a driving force for migration of cations, in the opposite direction toward the higher chemical potential (high pO_2-side). As a result, morphological instability, kinetic demixing, and decomposition can occur [23]. Although cation diffusion of the membrane candidate material thus directly determines the lifetime of the membrane, data on this property for oxidic materials have so far been limited. This contribution is part of our efforts to understand and quantify cation diffusion in LNO systems.

Cation diffusion can be determined by a range of methods, including solid state reaction (SSR) [24-26], tracer diffusion [27, 28] and inter-diffusion [29]. Previously, we investigated cation diffusion in LNO by SSR [26], where we determined the apparent self-diffusion coefficient of Ni^{2+}, and by chemical tracer diffusion, determining the impurity diffusion coefficient of Pr, Nd and Co in undoped [28] and in doped [30] LNO. Herein we report inter-diffusion data of coupled samples of $La_2NiO_{4+\delta}$-$Nd_2NiO_{4+\delta}$ and $La_2NiO_{4+\delta}$-$La_2CuO_{4+\delta}$ and compare them with our previously reported data on cation diffusion in LNO. Inter-diffusion data were obtained by analysing diffusion couples after annealing in air in the temperature range 950-1300 °C by means of Electron Probe Micro Analysis

(EPMA). The results are analysed according to Fick's second law and interpreted based on the material's crystal structure and point defect structure.

2. Experimental

2.1 Sample preparation

$La_2NiO_{4+\delta}$ was synthesised by spray pyrolysis followed by calcination at 800 °C and ball milling (CerPoTech, Norway). $Nd_2NiO_{4+\delta}$ (NNO) and $La_2CuO_{4+\delta}$ (LCO) powders were synthesised in-house through a wet chemical route [31]. High purity powders of Nd_2O_3 (99.99 %, Unocal Molycorp, USA), $Ni(NO_3)_2 \times 6H_2O$ (99.9+% Ni, STREM Chemicals, USA), La_2O_3 (99.99 %, Unocal Molycorp, USA) and $Cu(NO_3)_2 \times 2.5H_2O$ (99.99+%, Sigma-Aldrich, USA) were used for synthesis of the respective compounds. To ensure correct stoichiometry of the Nd, Ni, La and Cu cations, the content of water in the raw materials was determined by Thermo-Gravimetric Analysis (TGA) (Perkin Elmer TGA7). In the first step of the synthesis of NNO and LCO, Nd_2O_3 or La_2O_3, respectively, was dissolved in diluted HNO_3 (65%) and then stoichiometric amounts of $Ni(NO_3)_2 \times 6H_2O$ or $Cu(NO_3)_2 \times 2.5H_2O$ were added. Citric acid in amounts corresponding to 3 moles per mole of metal cations was then added to the cation solution. After evaporation of the solvent (distilled water) and dehydration at 170 °C, a metal-organic xerogel crust was formed. This was then crushed and burned at 500 °C to remove residual organics. The precursor so formed was then annealed at 1100 °C for 20 hours. The powders after this calcination were single phases of NNO and LCO as confirmed by X-Ray Diffraction (XRD).

The synthesised NNO and LCO powders were ball milled for 1 hour in a planetary mill (agate (SiO_2) crucible and balls, Retsch, Germany), before a polyacrylate based binder (Paraloid B-60 and B-72, Kall-Nor AS, Norway) dissolved in ethyl-acetate was added. Uniaxial pressing at ~200 MPa in a cylinder 13 mm in diameter yielded green bodies of LNO and NNO that were sintered at 1350 °C for 4 hours, reaching relative densities for both materials >95%. The green bodies of LCO were sintered at 1300 °C for 4 hours also with relative density of >95% as a result. The sintered samples were mounted into a dissolvable resin (Demotec 33, Demotec, Germany) and polished using diamond abrasive down to 1/4 μm (DP-spray P, Struers, Denmark). Finally, the resin was dissolved in acetone and samples were joined into inter-diffusion couples.

2.2 Diffusion experiments and EPMA analysis

Inter-diffusion couples for determination of A-site and B-site diffusion coefficient were made by facing the polished surfaces of LNO and NNO samples and LNO and LCO samples, respectively, in a spring loaded sample holder. The LNO-NNO inter-diffusion couples were annealed for 100-500 hours in the temperature range 1000-1300 °C. LNO-LCO inter-diffusion couples were annealed for 250-600 hours in the temperature range 950-1200 °C. All the annealings were conducted in ambient air. After annealing, the couples were mounted into epoxy resin and cut perpendicular to the sample interface and polished down to 1/4 μm by diamond abrasive. The polished surfaces were then carbon coated (EMITECH K950X) and the cross-sections were analysed by means of EPMA (Cameca SX100) with 5 wavelength-dispersive spectrometers utilising 15 kV acceleration voltage and 20 nA focused electron beam current. Counting time per peak for all elements was 20 s (and 10 s on each background, on each side of the peak)). The calibration standards for the relevant elements were in-house synthesised and sintered $LaPO_4$ and $NdPO_4$, commercial NiO powder sintered by us, and Cu metal. Each inter-diffusion couple was analysed along 5-10 different lines perpendicular to the phase boundaries, determining the composition every 1 μm. Depending on annealing time and temperature, the analysed lines were 70-160 μm in length divided equally between two phases. The concentration profiles of La and Nd in the LNO/NNO solid solution were used to estimate A-site diffusion, and Ni and Cu in LNO/LCO solid solution for the estimation of B-site diffusion. In addition, cross-sections were also mapped by means of EPMA visualising diffusion paths into the materials. EPMA settings for the mapping were beam current of 50 nA and a dwell time of 50 ms.

We emphasise the uncertainties of the measurements arising from sample porosity, the detection limit of the instrument (~100 ppm), and the low average concentration of diffusants deep into the sample used to estimate grain boundary enhanced transport.

3. Results and discussion

3.1 Microstructure and concentration profiles

Figure 1 shows a backscatter electron micrograph of a polished cross-section of a LCO-LNO diffusion couple annealed for 300 h at 1150 °C in air. The phase boundary between

the two materials disappeared, indicating that materials inter-diffuse into each other and can be identified only by the difference in microstructure. Porosity on the upper part of the micrograph represents Kirkendall porosity, observed only in LCO-LNO diffusion couples. The phase boundary was also disappeared between NNO and LNO phases. In this diffusion couple the phases can be only differentiated by the original difference in microstructure.

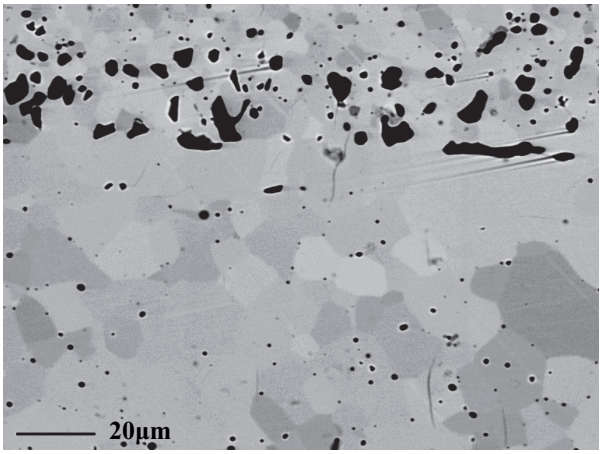

Figure 1. EPMA backscatter electron image of a diffusion couple annealed for 300 h at 1150 °C in air. The upper phase is LCO and the lower is LNO.

Pore formation, i.e., Kirkendall porosity, is a reliable evidence that the diffusion occurs via a vacancy mechanism. The formation of pores occurs as a consequence of the vacancy interaction with micro-cavity sinks in the diffusion zone [32]. Kirkendall porosity can also act as an inert marker, indicating the fastest moving species in a diffusion couple. On the other hand, the slowest moving species can be identified in the absence of such porosity [33], as demonstrated from the A-site diffusion couple in this work. These findings are in agreement with our results from previous SSR [26] and chemical tracer [28] experiments, where we observed that the B-site cation has higher effective diffusivity than the A-site.

Figures 2 and 3 represent mapping of the diffusing cations, i.e., Ni and Cu in LCO-LNO and La and Nd in NNO-LNO diffusion couples, respectively. Inter-diffusion can be clearly observed in both couples. In the LCO-LNO diffusion couple the bulk diffusion is predominant close to the phase boundary, and the grain boundary diffusion is clearly visible in the deeper regions of both materials (Figure 2). However, in the NNO-LNO diffusion couple, only bulk diffusion was observed (Figure 3). Based on this, one can

conclude that B-site cation transport (LCO-LNO couples) is enhanced along grain boundaries, while A-site cation transport (NNO-LNO couples) is dominated by bulk diffusion [34, 35].

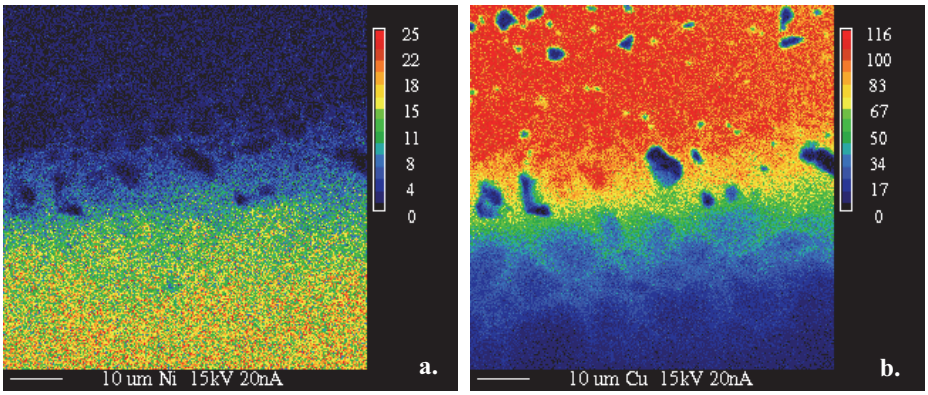

Figure 2. EPMA mapping of a. Ni and b. Cu in LCO-LNO diffusion couple annealed for 300 h at 1150 °C in air. Bright colours represent higher concentration of respective element.

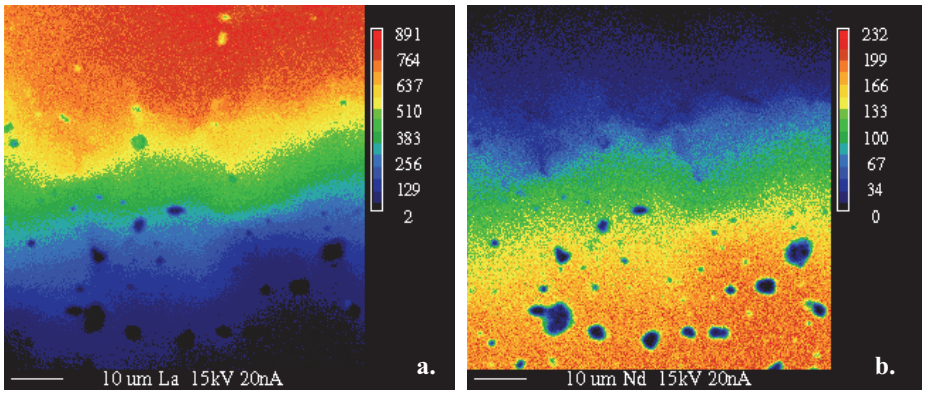

Figure 3. EPMA mapping of a. La and b. Nd in NNO-LNO diffusion couple annealed for 300 h at 1150 °C in air. Bright colours represent higher concentration of respective element.

Typical concentration profiles of Ni and Cu in LCO-LNO, and La and Nd in NNO-LNO diffusion couples are shown in Figure 4. The concentration profiles from different line scans at different positions in one diffusion couple overlap each other, showing that the position of the contact interface between materials could be determined correctly in each case (defined by 50% concentration). The continuous change in the concentration of the diffusing cations across the diffusion zone for both diffusion couples, reveals that they

substitute each other completely. In agreement with this, there is no evidence of an intermediate phase in Figures 1, 2 or 3.

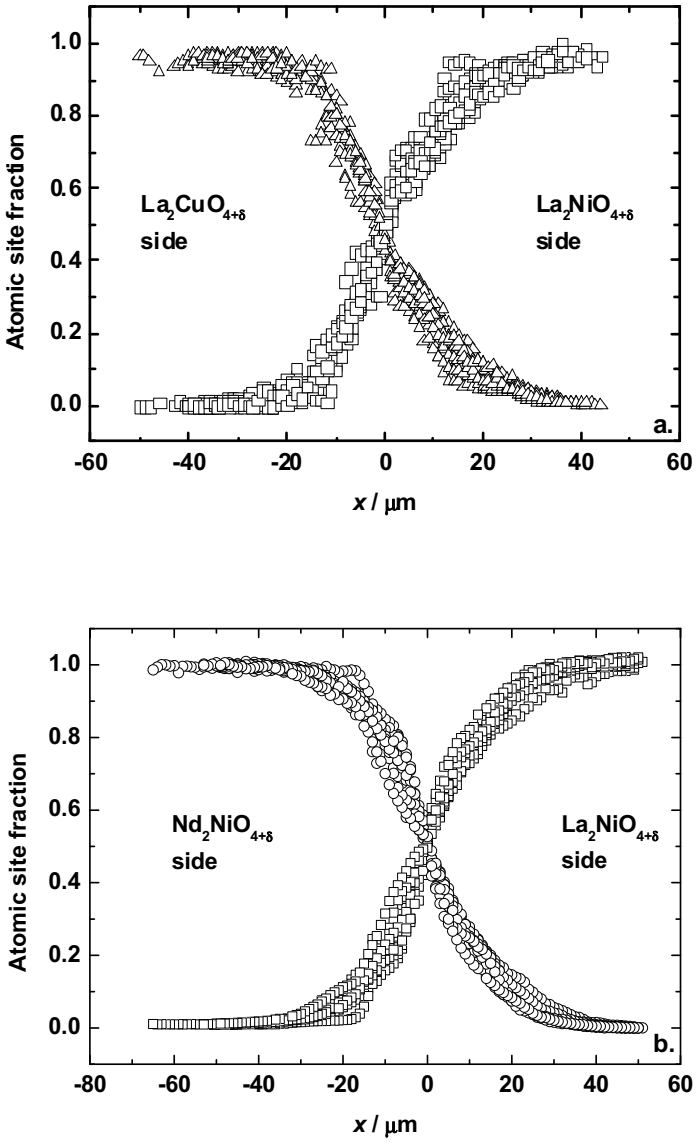

Figure 4. Inter-diffusion concentration profiles of a. Ni and Cu obtained in LCO-LNO and b. La and Nd obtained in NNO-LNO diffusion couples annealed for 500 h at 1100 °C and 171 h at 1200 °C, respectively, in air.

The fluxes of the inter-diffusing cations must balance each other, so that the extracted inter-diffusion coefficients reflect the properties of both cations in the material for which the profiles are analysed. The extracted inter-diffusion coefficient can thus be referred to as La/Nd or Ni/Cu diffusion coefficients in LNO/NNO or LNO/LCO solid solution, respectively. If inter-diffusion is higher in one material of the inter-diffusion couple than in the other, the phase boundary will move and complicate the analysis. In our study, however, the concentration cross-over points coincide with the change in microstructure, indicating that the inter-diffusivities in the two materials are sufficiently equal that the phase boundary can be taken as stationary.

3.2 Bulk and grain boundary diffusion coefficients

To derive diffusion coefficients from the concentration profiles, one can use the solution of Fick's second law for the case of a constant source [36]. The following expression was used for the estimation of bulk diffusion coefficient

$$c_b(x) = \frac{c_1 - c_2}{2}\,\mathrm{erfc}\frac{x}{2\sqrt{D_\mathrm{b}t}} + c_2 \qquad \mathbf{1}$$

where c_1 and c_2 are the beginning and ending concentration of the diffusion cations, x is the distance from the original interface (phase boundary), D_b is the bulk inter-diffusion coefficient, t is the annealing time, and erfc denotes the complementary error function.

To estimate the grain boundary diffusion coefficient D_gb one can use the Whipple-Le Claire approximate solution for the grain boundary diffusion from constant source [34, 37]

$$wD_\mathrm{gb} = 0.3292\sqrt{\frac{D_\mathrm{b}}{t}}\left(-\frac{\partial \log c}{\partial x^{6/5}}\right)^{-5/3} \qquad \mathbf{2}$$

where w is the grain boundary width. According to Eq. 2, D_gb can be calculated from the constant slope in a linear part of a plot of log c versus $x^{6/5}$ in deeper regions of the depth profile.

As the concentration of the diffusing cations at any distance from the phase boundary is the sum of the diffusant concentration in the bulk and along grain boundaries, one can write

$$\log(c(x)) = \log(c_b(x) + c_{gb}(x)) \quad \textbf{3}$$

In this work, Eq. 1 was used to determine bulk diffusion coefficient for bulk dominated kinetics (in LNO/NNO solid solution) (Figure 5a), while Eqs. 1, 2 and 3 were used for the estimation of bulk and grain boundary diffusion coefficient for kinetics enhanced along grain boundaries (in LNO/LCO solid solution) (Figure 5b).

Each inter-diffusion coefficient for the A-site cation can be determined from the concentration profile of La or of Nd for the LNO-NNO couple, and will in the following be referred to as $D_{La/Nd}$ and $D_{Nd/La}$, respectively. Similarly, we use $D_{Ni/Cu}$ and $D_{Cu/Ni}$ for the B-site inter-diffusion.

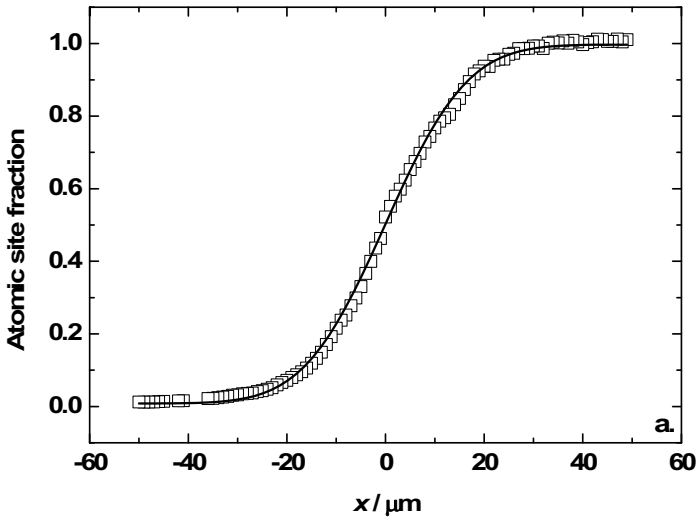

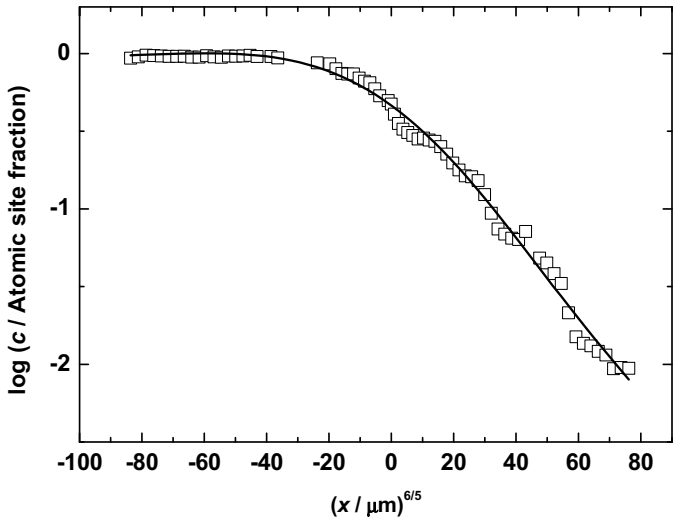

Figure 5. Examples for the determination of a. bulk inter-diffusion coefficient for the diffusion couple LNO-NNO annealed for 171 hours at 1200 °C; b. the grain boundary inter-diffusion coefficients for the LCO-LNO diffusion couple, annealed for 500 hours at 1100 °C.

The $D_{La/Nd}$ and $D_{Ni/Cu}$ inter-diffusion coefficients obtained from NNO-LNO and LCO-LNO diffusion couples are shown in Figure 6a and 6b, respectively. It is evident that the extracted inter-diffusion coefficients in the respective solid solutions (LNO/LCO and LNO/NNO) are effectively identical regardless of which of the two inter-diffusing cations is used in each case. This confirms that the diffusivities of cations in the two phases of each couple are virtually equal and that the phase boundaries can be taken as stationary.

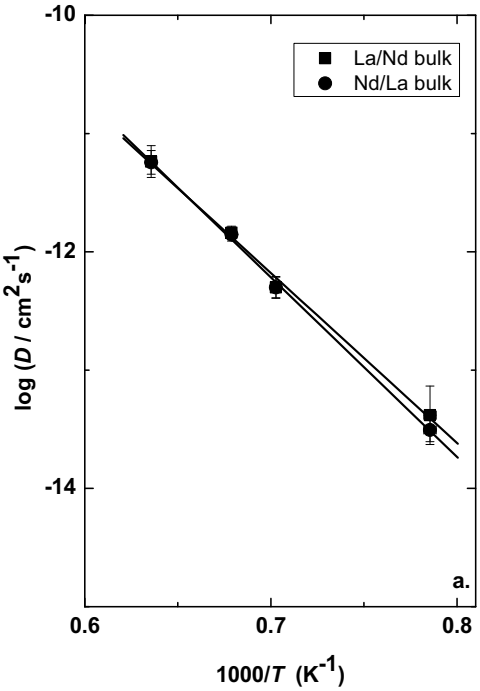
-10
-12
-14
0.6
0.7
0.8
log (D / cm2s-1)
1000/T (K-1)
La/Nd bulk
Nd/La bulk
a.

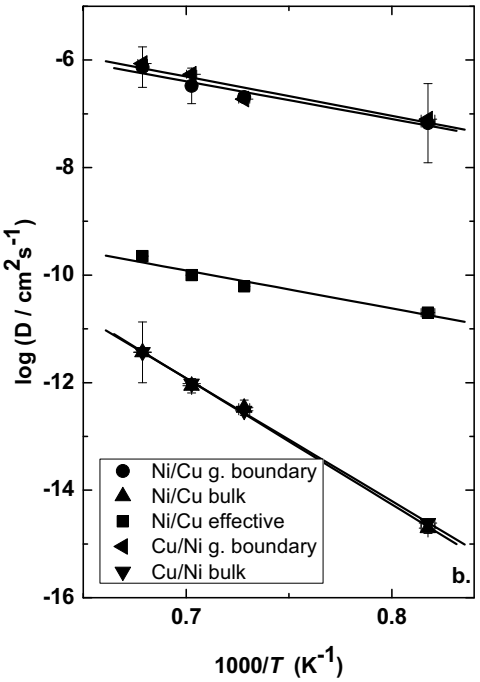

Figure 6. Arrhenius plot of comparison between a. bulk inter-diffusion coefficients $D_{La/Nd}$ and $D_{Nd/La}$ and b. grain boundary, bulk and effective inter-diffusion coefficients $D_{Ni/Cu}$ and $D_{Cu/Ni}$ obtained from NNO-LNO and LCO-LNO diffusion couples, respectively, annealed in air.

The inter-diffusion coefficients exhibit Arrhenius behaviour and the ones based on the concentration profiles of La and Ni may be expressed as

$$D_{\mathrm{La/Nd}}(\mathrm{cm^2/s}) = 10^{-2.1\pm0.4}\exp\left(-\frac{275\pm12\mathrm{kJ/mol}}{RT}\right) \quad \textbf{4}$$

$$D_{\mathrm{Ni/Cu_b}}(\mathrm{cm^2/s}) = 10^{4.5\pm0.6}\exp\left(-\frac{450\pm20\mathrm{kJ/mol}}{RT}\right) \quad \textbf{5}$$

$$D_{\mathrm{Ni/Cu_{gb}}}(\mathrm{cm^2/s}) = 10^{-1.5\pm0.8}\exp\left(-\frac{135\pm20\mathrm{kJ/mol}}{RT}\right) \quad \textbf{6}$$

$$D_{\mathrm{Ni/Cu_{eff}}}(\mathrm{cm^2/s}) = 10^{-4.9\pm0.8}\exp(-\frac{135\pm20\mathrm{kJ/mol}}{RT}) \quad \textbf{7}$$

The effective diffusion coefficient (Eq. 7) is related to the bulk and grain boundary diffusion coefficients by the Hart equation [38]:

$$D_{\mathrm{eff}} = gD_{\mathrm{gb}} + (1-g)D_{\mathrm{b}} \quad \textbf{8}$$

where g is given by the volume fraction of grain boundaries in the polycrystal ($g \approx 3(w/d)$) [39]. The calculated effective diffusion coefficient for Ni/Cu, assuming a grain boundary width (w) of 1 nm and grain size (d) of the order of 10 μm, is dominated by the grain boundary contribution within the present experimental temperature range. The effective and grain boundary diffusion coefficients thus have very similar activation energies, whereas the pre-exponential obviously gets a very different value due to the geometrical operation.

Figure 2a and b visualise the predominance of Ni/Cu diffusion along grain boundaries (in LNO/LCO solid solution) and negligible Ni/Cu bulk diffusion. This is supported by our finding of enhanced transport in the grain boundaries for B-site cations from a parallel experiment with Co chemical tracer in LNO [28].

B-site grain boundary diffusivity in the LNO/LCO diffusion couple is, for the present experimental temperature range, typically 5 orders of magnitude higher than its bulk diffusion, and has an activation enthalpy of only about one third of that of bulk diffusion. There are only limited studies on the relationships between bulk and grain boundary activation energies, but it is generally expected and observed – as in our case – that $\Delta E_{\mathrm{B}} > \Delta E_{\mathrm{GB}}$ [40].

3.3 Further analysis of the bulk diffusivities of the A- and B-site cations

The relations between the phenomenological self-diffusion coefficient D of an ion and the random diffusion coefficient D_{d} of a defect d (e.g. vacancies) of that ion, and their Arrhenius-type temperature dependencies can generally be expressed by

$$D = D_0\exp(-\frac{\Delta E_{\mathrm{a}}}{RT}) = [\mathrm{d}]D_{\mathrm{d}} = [\mathrm{d}]_0\exp(-\frac{\Delta H_{\mathrm{d}}^{\circ}}{RT})D_{\mathrm{m},0}\exp(-\frac{\Delta H_{\mathrm{m}}}{RT}) = [\mathrm{d}]_0 D_{\mathrm{m},0}\exp(-\frac{\Delta H_{\mathrm{d}}^{\circ}+\Delta H_{\mathrm{m}}}{RT}) \quad \textbf{9}$$

where [d] is the fractional concentration of defects, and the activation energy (ΔE_a) contains both a defect formation term (ΔH_d°) and defect mobility term (ΔH_m):

$$\Delta E_a = \Delta H_d^\circ + \Delta H_m \quad \textbf{10}$$

and the pre-exponential term also has two components: $D_0 = [d]_0 D_{m,0}$.

The experimentally obtained bulk diffusivities for the A- and B- sites are essentially in the same range, but the derived activation energy ΔE_a for A-site bulk diffusion is significantly lower than that of B-site (Figure 7). Accordingly, the pre-exponentials D_0 are different by 7 orders of magnitude. A similar behaviour was observed in our parallel experiments with Nd and Pr chemical tracers for A-site diffusion and Co tracer for B-site diffusion in LNO [28]. We will in the following analyse this in terms of the pre-exponentials of defect self-diffusion $D_{m,0}$ and concentration $[d]_0$.

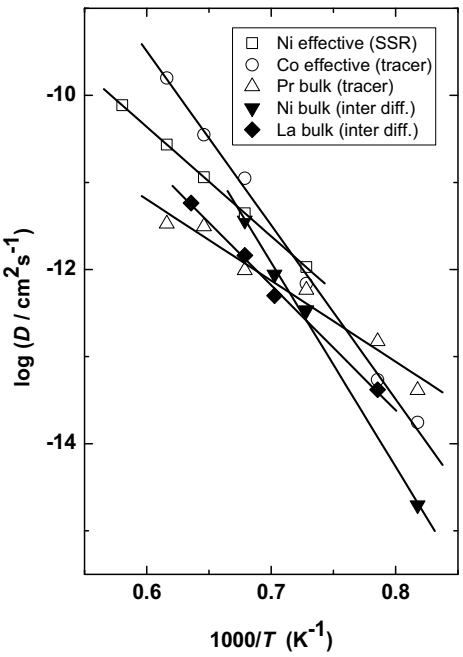

Figure 7. Comparison of bulk inter-diffusion coefficients $D_{La/Nd}$ and $D_{Ni/Cu}$ with the diffusion coefficients obtained by SSR [26] and chemical tracer techniques [28] in LNO system.

The pre-exponential of defect diffusion $D_{m,0}$ is given by

$$D_{m,0} = \gamma a^2 \nu \exp(\frac{\Delta S_m}{R}) \quad \textbf{11}$$

where a is the distance between two adjacent cation sites and γ is a structure-dependent constant which for vacancy mechanism may be assumed to be unity [41, 42]. ΔS_m is the activation entropy for the vacancy jump, usually unknown or assumed to be negligibly small. The vibration attempt frequency ν can be estimated via the enthalpy for the defect migration (ΔH_m) [41, 42]:

$$\nu = \frac{2}{\pi a}\sqrt{\frac{\Delta H_m}{M}} \quad \textbf{12}$$

where M is the molar mass. We shall return to actual estimates of ΔH_m and ν later, but it is clear that the pre-exponential of defect diffusion $D_{m,0}$ resulting from different activation energies cannot differ by more than within an order of magnitude, and can as such not account for the observed 7 orders of magnitude difference in D_0.

Next, we therefore consider defect concentrations. All the samples used in this inter-diffusion experiment were sintered at temperatures above the experimental window, and it is possible that defect concentrations are frozen in ([d] = constant) and that the total observed activation energy ΔE_a contains only the vacancy migration enthalpy ΔH_m. However, during long-term annealings, particularly at the higher end of the experimental temperature window, the defect concentrations may be at equilibrium. The latter is likely to apply to B-site vacancies that may equilibrate through fast B-site transport in grain boundaries [28]. According to this hypothesis, segregation of B-site cations (possibly precipitates of a secondary phase) may exist at grain boundaries due to the requirements that new unit cells should be created (or annihilated) during equilibration of defects. If the B-site defects reach equilibrium during diffusion couple annealing, the activation energy of B-site diffusion will be determined not only by the vacancy migration enthalpy, but also by the vacancy formation enthalpy. This may result in the higher apparent activation energy for diffusion of B-site cations than for A-site cations, which may have frozen in concentration of vacancies.

Under the simplified assumption that oxygen interstitials and electron holes are the major defects, the minority concentration of Ni vacancies in the bulk material can be shown to be:

$$[v_{Ni}^{//}] = 16^{7/9}\, pO_2^{2/9} \exp\left(\frac{\Delta S_S^\circ}{3R} - \frac{4\Delta S_{AF}^\circ}{3R} + \frac{4\Delta S_{Ox}^\circ}{9R}\right)\exp\left(-\left(\frac{\Delta H_S^\circ}{3RT} - \frac{4\Delta H_{AF}^\circ}{3RT} + \frac{4\Delta H_{Ox}^\circ}{9RT}\right)\right) \qquad \textbf{13}$$

where ΔS_S°, ΔS_{AF}° and ΔS_{Ox}° are standard entropies of the reaction of creation of cation and anion vacancies (Schottky disorder), oxygen defect pairs (anti-Frenkel disorder) and oxygen interstitials and electron holes (oxidation), respectively. ΔH_S°, ΔH_{AF}° and ΔH_{Ox}°, represent the standard enthalpies of the corresponding reactions. Other terms have their usual meanings. In order now to estimate effective energies and concentrations, we use values for entropies and enthalpies from literature [1, 3]. The estimate of the formation enthalpy of Ni vacancies, ΔH_d°, in this way becomes around 350 kJ/mol. It can thus explain a large part of the high activation energy for bulk diffusion in our LCO-LNO diffusion couples (450 kJ/mol), leaving – under all the assumptions made – around 100 kJ/mol of activation energy for vacancy defect diffusion. Values for enthalpy of migration of vacancies from the literature vary over a wide range, as they depend on and increase with the charge and size of the migrating cation [43-46]. Data for the enthalpy of migration of divalent cation defects in ternary oxides are rather limited, but it is of interest to note that De Souza *et al.* [43] found values from approximately 1.3 to 3.5 eV (~130-350 kJ/mol) for the enthalpy of migration for divalent cation dopant at the B-site in $LaGaO_3$ by modelling. The activation energy for the high B-site grain boundary diffusion of 135 kJ/mol is thus in the range expected for vacancy migration. This suggests that the concentration of B-site vacancies in the grain boundaries is high and constant – perhaps fixed by lattice mismatch or secondary phase equilibria.

The experimentally observed activation energy ΔE_a for diffusion of the A-site cation has a comparatively low value of 275 kJ/mol. The work of Smith *et al.* [29] on inter-diffusion between $LaFeO_3$ and $NdFeO_3$ report rather high activation energy values for grain boundary and bulk diffusion (610 and 600 kJ/mol, respectively) in this solid solution. De Souza *et al.* [43, 44] works on modelling of cation defects in $LaGaO_3$ and $LaMnO_3$ also reports high activation energy values (~480 and ~385 kJ/mol, respectively) for diffusion of A-site cations. Moreover, from what we have seen above, the enthalpy of formation of La vacancies – similar to that of the Ni vacancies – should be ~350 kJ/mol, and we should

expect that the activation energy for diffusion of La in the NNO-LNO diffusion couples should have a value significantly higher when the enthalpy of vacancy diffusion is added. Consequently, the lower observed activation energy (275 kJ/mol) may reflect frozen in La vacancies, i.e., that La vacancies did not reach equilibrium in our experimental temperature range.

If our assumptions above are correct, Ni diffusivity has a pre-exponential containing the pre-exponential terms of Eq. 13, a number not very different from unity. On the other hand, La diffusivity should contain instead simply the frozen-in concentration of La vacancies, which would, for instance, at a freezing-in temperature of 1350 °C come out as 5.9×10^{-13} (from an equation for La vacancies similar to that of Eq. 13 that differs just for the simple numerical factor). Within the expectancy of all the assumptions made, this credibly makes account of the observed 7 orders of magnitude in pre-exponentials of the two cation site diffusion coefficients.

Figure 7 compares data of bulk inter-diffusion obtained in this work with our previous results from SSR [26] and chemical tracer [28] studies. Considering the different experimental techniques, the obtained diffusivities are in relatively good agreement with each other: Effective B-site cation diffusion exhibits generally a higher diffusivity than the A-site due to the contribution from the faster grain boundary transport.

3.4 Comparison with data from literature on related oxide systems

The Arrhenius plot in Figure 8 shows the data for inter-diffusion coefficients for A- and B-site cations from this work, together with some previously reported data about cation diffusion in other similar perovskite systems. To the best of our knowledge there is only one report about cation diffusion for materials with K_2NiF_4-type structure up to now. Palcut *et al.* [47] reported a single parabolic rate constant (4×10^{-11} cm^2/s) for the reaction at 1300 °C between La_2O_3 and CoO, forming La_2CoO_4. It was concluded that it reflects the diffusion of Co^{2+} in La_2CoO_4.

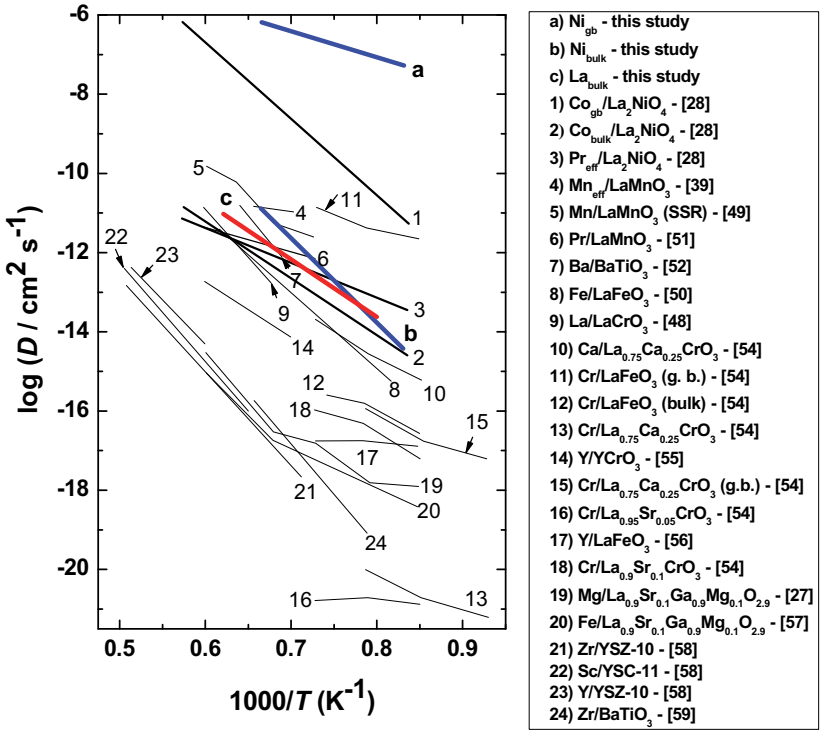

Figure 8. Values for the inter-diffusion coefficients of La/Nd and Ni/Cu in inter-diffusion couples of $La_2NiO_{4+\delta}$-related phases used in this study compared with data for cation diffusion coefficients of various perovskites and perovskite-related materials from the literature.

The data in the literature on cation diffusion in ABO_3 systems with A-site rare-earth and B-site transition metals show that B-site cations exhibit higher diffusivity than those of A-site. One exception to this is $LaCrO_3$ [48] where La has higher diffusivity. However, the A-site diffusivity in the LNO system is rather high even when compared with the relatively high diffusivities of B-site cations in the other perovskite systems. The same case is with the B-site diffusivity that is even higher than that of A-site in the LNO system due to grain boundary contributions. If we also compare the activation energies from this work with the ones from the literature (Figure 8), it is evident that they also exhibit the similar values to other perovskite-related materials. Nevertheless, the LNO system investigated in this work, together with some cobaltite [47], manganite [49] and ferrite [50] perovskites demonstrates rather high cation diffusivities.

4. Conclusions

$Nd_2NiO_{4+\delta}$-$La_2NiO_{4+\delta}$ and $La_2CuO_{4+\delta}$-$La_2NiO_{4+\delta}$ diffusion couples were investigated for cation inter-diffusion in the temperature range 950-1300 °C annealed in air up to 600 h. It is determined from the concentration profiles that A-site kinetics is dominated by bulk diffusion, while B-site by enhanced grain boundaries, all in accordance with our previous results from solid state reaction and chemical tracer experiments. The inter-diffusion coefficients $D_{La/Nd}$ and $D_{Ni/Cu}$ may be expressed as

$$D_{La/Nd}(cm^2/s) = 10^{-2.1\pm0.4}\exp(-\frac{275\pm12kJ/mol}{RT})$$

$$D_{Ni/Cu_b}(cm^2/s) = 10^{4.5\pm0.6}\exp(-\frac{450\pm20kJ/mol}{RT})$$

$$D_{Ni/Cu_{gb}}(cm^2/s) = 10^{-1.5\pm0.8}\exp(-\frac{135\pm20kJ/mol}{RT})$$

$$D_{Ni/Cu_{eff}}(cm^2/s) = 10^{-4.9\pm0.8}\exp(-\frac{135\pm20kJ/mol}{RT})$$

It is suggested that the higher apparent activation energy of B-site inter-diffusion is due to the effect of varying defect concentrations for this site, since it can equilibrate via fast grain boundary diffusion, contrary to the A-site, which may freeze above the experimental temperature range. The grain boundary diffusion of B-site cations in LNO/LCO solid solution is around 5 orders of magnitude higher than that of bulk at the temperatures studied here, contributing to higher effective diffusivity on the B-site than the A-site. All in all, cation diffusion in the $La_2NiO_{4+\delta}$ system exhibits rather high values when compared with other perovskite-related materials.

5. Acknowledgements

The authors are thankful for financial support under the project "162316 Demonstration of AZEP Reactor Module" of the Research Council of Norway (RCN) and Statoil and to Muriel M. L. Erambert at Department of Geosciences, University of Oslo for EPMA analyses.

6. References

[1] E.N. Naumovich, M.V. Patrakeev, V.V. Kharton, A.A. Yaremchenko, D.I. Logvinovich, F.M.B. Marques, Solid State Sci. 7 (2005) 1353-1362.

[2] J. B. Smith, T. Norby, J. Electrochem. Soc. 153(2) (2006) A233-A238.

[3] Z. Li, R. Haugsrud, J. B. Smith, T. Norby, Solid State Ionics 180 (2009) 1433-1441.

[4] Z. Li, R. Haugsrud, J. B. Smith, T. Norby, J. Electrochem. Soc. 159(9) (2009) B1039-B1044.

[5] S. J. Skinner, J. A. Kilner, Solid State Ionics, 135 (2000) 709-712.

[6] V. V. Vashook, I. I. Yushkevich, L. V. Kokhanovsky, L. V. Makhnach, S. P. Tolochko, I. F. Kononyuk, H. Ullmann, H. Altenburg, Solid State Ionics 119 (1999) 23-30.

[7] V. V. Vashook, S. P. Tolochko, I. I. Yushkevich, L. V. Makhnach, I. F. Kononyuk, H. Altenburg, J. Hauck, H. Ullmann, Solid State Ionics 110 (1998) 245-253.

[8] C. N. Munnings, S. J. Skinner, G. Amow, P. S. Whitfield, I. J. Davidson, Solid State Ionics 176 (2005) 1895-1901.

[9] V. V. Kharton, A. P. Viskup, E. N. Naumovich, F. M. B. Marques, J. Mater. Chem. 9 (1999) 2623-2629.

[10] F. Mauvy, E. Boehm, J. M. Bassat, J. C. Grenier, J. Fouletier, Solid State Ionics 178 (2007) 1200-1204.

[11] E. Boehm, J. M. Bassat, M .C. Steil, P. Dordor, F. Mauvy, J. C. Grenier, Solid State Sci. 5 (2003) 973-981.

[12] J. B. Goodenough, S. Ramasesha, Mat. Res. Bull. Vol. 17 (1982) 383-390.

[13] S. J. Skinner, Solid State Sci. 5 (2003) 419-426.

[14] A. Aguadero, M. Pérez, J. A. Alonso, L. Daza, J. Power Sources 151 (2005) 52-56.

[15] T. Ido, k. Magoshi, H. Eisaki, S. Uchida, Phys. Rev. B Vol. 44 (1991) 12094-12097.

[16] H. Ishikawa, Y. Toyosumi, K. Ishikawa, J. Alloys Compd. 408-412 (2006) 1196-1199.

[17] C. Frayret, A. Villesuzanne, M. Pouchard, Chem. Mater. 17 (2005) 6538-6544.

[18] W. Paulus, A. Cousson, G. Dhalenne, J. Berthon, A. Revcolevschi, S. Hosoya, W. Treutmann, G. Heger, R. Le Toquin, Solid State Sci. 4 (2002) 565-573.

[19] J. D. Jorgensen, B. Dabrowski, S. Pei, D. R. Richards, D. G. Hinks, Phys. Rev. B Vol. 40 (1989) 2187-2199.

[20] A. Aguadero, J. A. Alonso, M. J. Martinez-Lope, M. T. Fernández-Diaz, M. J. Escudero, L. Daza, J. Mater. Chem. 16 (2006) 3402-3408.

[21] M. Schroeder, M.-A. Dragan, J. Mater. Sci. 42 (2007) 1972-1983.

[22] M. S. D. Read, M. S. Islam, F. King, F. E. Hancock, J. Phys. Chem. B 103 (1999) 1558-1562.

[23] M. Martin, J. Chem. Thermodyn. 35 (2003) 1291-1308.

[24] C. Wagner, Z. Phys. Chem. Abt. B 33-34 (1936) 309.

[25] H. Schmalzried, Solid State Reactions, Chapter 6, Verlag Chemie, Weinheim/Bergstr., 1974.

[26] N. Čebašek, R. Haugsrud, Z. Li, J. Milošević, J. B. Smith, A. Magrasó, T. Norby, J. Electrochem. Soc. 159 (6) (2012) B702-B708.

[27] O. Schulz, M. Martin, C. Argirusis, G. Borchardt, Phys. Chem. Chem. Phys. 5 (2003) 2308-2313.

[28] N. Čebašek, R. Haugsrud, Z. Li, J. B. Smith, T. Norby, To be submitted.

[29] J. B. Smith, T. Norby, A. Fossdal, J. Am. Ceram. Soc. 89 (2006) 582-586.

[30] N. Čebašek, R. Haugsrud, Z. Li, T. Norby, To be submitted.

[31] A. Douy, P. Odier, Mat. Res. Bull. 24 (1989) 1119-1126.

[32] L.N. Partiskaya, Defect Diffus. Forum Vol. 249 (2006) 73-80.

[33] S. Gopalan, A. V. Virkar, J. Am. Ceram. Soc. 82 (1999) 2887-99.

[34] I. Kaur, Y. Mishin, W. Gust, Fundamentals of Grain and Interphase Boundary Diffusion, John Wiley & Sons LTD, Chichester, 1995.

[35] L.G. Harrison, Trans. Faraday Soc. 57 (1961) 1191-1199.

[36] J. Crank, Mathematics of Diffusion, Oxford University Press, 1979.

[37] C. Herzig, Y. Mishin, Diffusion in Condensed Matter, Methods, Materials, Models, editors P. Heitjans, J, Kärger, Springer, Berlin, 2005, p. 337.

[38] E. W. Hart, Acta Metall. 5 (1957) 597.

[39] S. Miyoshi, M. Martin, Phys. Chem. Chem. Phys. 11 (2009) 3063-3070.

[40] P. Kofstad, Nonstoichiometry, Diffusion, and Electrical Conductivity in Binary Metal Oxides, Wiley - Interscience, A Division of John Wiley & Sons, Inc., New York, London, Sidney, Toronto, 1972.

[41] C. Zener, J. Appl. Phys. Vol. 22, No. 4 (1951) 372-375.

[42] R. Haugsrud, T. Norby, J. Electrochem. Soc. 146 (3) (1999) 999-1004.

[43] R. A. De Souza, Phys. Chem. Chem. Phys. 5 (2003) 740-748.

[44] R. A. De Souza, M. S. Islam, E, Ivers-Tiffée, J. Mater. Chem. 9 (1999) 1621-1627.

[45] M. Kilo, M.A. Taylor, C. Argirusis, G. Borchardt, R.A. Jackson, O. Schulz, M. Martin, M. Weller, Solid State Ionics 175 (2004) 823-827.

[46] W.C. Mackrodt, P.M. Woodrow, J. Am. Ceram. Soc. 69 (3) (1986) 277-280.

[47] M. Palcut, K. Wiik, T. Grande, J. Phys. Chem. Vol. 111 (B 2007) 2299-2308.

[48] T. Akashi, M. Nanko, T. Maruyama, J. Electrochem. Soc. Vol. 145 No. 6 (1998) 2090-2094.

[49] M. Palcut, K. Wiik, T. Grande, J. Phys. Chem. 111 (C 2007) 813-822.

[50] J. B. Smith, T. Norby, Solid State Ionics 177 (2006) 639–646.

[51] M. Palcut, J. S. Christensen, K. Wiik, T. Grande, Phys. Chem. Chem. Phys. 10 (2008) 6544-6552.

[52] A. Kitahara, M. Nanko, K. Kawamura, T. Maruyama, Proceedings - Electrochemical Society 99-38 (High Temperature Corrosion and Materials Chemistry) (2000) 534-545.

[53] T. Horita, M. Ishikawa, K. Yamaji, N. Sakai, H. Yokokawa, M. Dokiya, Solid State Ionics 124 (1999) 301-307.

[54] N. Sakai, K. Yamaji, T. Horita, H. Negishi, H. Yokokawa, Solid State Ionics 135(1-4) (2000) 469-474.

[55] K. Kawamura, A. Saiki, T. Maruyama, K. Nagato, J. Electrochem. Soc. 142 (1995) 3073-3077.

[56] I. Wærnhus, N. Sakai, H. Yokokawa, T. Grande, M-A. Einarsrud, K. Wiik, Solid State Ionics 178 (2007) 907-914.

[57] O. Schulz, S. Flege, M. Martin, Proceedings - Electrochemical Society PV 2003-7 (Solid Oxide Fuel Cells VIII) (2003) 304-314.

[58] Y. M. Chiang, W. D. Kingery, J. Am. Ceram. Soc. 73 (1990) 1153-1158.

[59] S. Koerfer, R. A. De Souza, H. I. Yoo, M. Martin, Solid State Sci. 10 (2008) 725-734.

5.2 Paper II

Determination of Chemical Tracer Diffusion Coefficients for the La- and Ni-site in $La_2NiO_{4+\delta}$ Studied by SIMS.

Author: *Nebojša Čebašek*

Manuscript

Determination of Chemical Tracer Diffusion Coefficients for the La- and Ni-site in $La_2NiO_{4+\delta}$ Studied by SIMS

Nebojša Čebašek

[1]University of Oslo, Centre for Materials Science and Nanotechnology, FERMIO, Gaustadalleen 21, NO-0349 Oslo, Norway

Abstract

Chemical (impurity) tracer diffusion of Pr, Nd, and Co into polycrystalline $La_2NiO_{4+\delta}$ was done at 950-1350 °C in air, argon and intermediate pO_2 (5.5×10^{-3} atm O_2), and diffusion coefficients extracted from depth profiles determined by Secondary Ion Mass Spectrometry (SIMS). The Pr and Nd profiles have only one broad region, corresponding to bulk diffusion, whereas the Co tracer depth profile have two distinct regions with different slopes, where the outer shallow region represents bulk diffusion and the inner region with deep penetration depths represents grain boundary diffusion. It is thus concluded that the diffusivity on the Ni-site is enhanced by grain boundary diffusion. The bulk diffusion was evaluated using the solution of Fick's 2nd law for thin-film source, and the grain boundary diffusion was evaluated according to Whipple-Le Claire's equation. The average apparent activation energies for Pr and Nd bulk diffusion are 165±15 kJ/mol, for Co bulk diffusion 295±15 kJ/mol, and for Co grain boundary diffusion 380±20 kJ/mol. Qualitatively, the diffusivities and activation energies follow levels and trends in agreement with those from other experimental techniques. The apparent lack of - in fact reverse - correlation between activation energy and level of diffusivity is discussed in terms of a possibility that the faster species (Ni) exhibits equilibrium defect concentrations while the slower (La) is in effect frozen in.

Keywords: $La_2NiO_{4+\delta}$, cation diffusion, bulk diffusion, grain boundary diffusion, SIMS

1. Introduction

Mixed oxide ion and electron conductors with chemical stability over a wide range of oxygen partial pressures have technological potential as membranes in separation and purification of oxygen. When selecting materials for this application, high mixed oxide ion-electron conductivity is normally given primary focus. Under operation, however, the oxygen chemical potential gradient also induces cation transport across the membrane. Although cation diffusion is generally slow, degradation processes rate determined by cation transport, such as kinetic demixing and decomposition (into new phases) as well as morphological instability ("chemical creep", "walk-out") [1, 2] in principle determine the membrane durability and need accordingly to be addressed.

$La_2NiO_{4+\delta}$ (LNO) exhibits high mixed oxide ion and p-type electronic conductivity and represents, as such, a promising candidate for oxygen gas separation membranes [3-11]. Accordingly, the transport properties and the relation to the structure of undoped and doped LNO have been subject of extensive investigations. LNO crystallises according to a tetragonal unit cell with space group I4/mmm, above 150 °C in a layered structure where perovskite $LaNiO_3$ layers alternate with rock salt LaO layers along the *c*-axis. LNO is renowned to have large oxygen hyper-stoichiometry (δ), reaching as high as $\delta = 0.25$. Oxygen excess (interstitials, O_i'') compensated by electron holes ($h^\bullet$, representing mainly Ni^{3+}) are majority defects in LNO.

Cation diffusion in ternary oxides can be characterised and quantified by techniques comprising solid state reaction (SSR) [12-14], tracer diffusion [15] and inter-diffusion [16]. To the best of our knowledge there were no data on the cation diffusion in LNO until our effort to reach a basis for a firm evaluation of the long term durability of LNO by utilizing these techniques. In the present work we aim to characterise cation diffusion in LNO by means of Pr, Nd and Co chemical (impurity) tracer annealing followed by depth profiling with Secondary Ion Mass Spectrometry (SIMS).

2. Experimental

LNO powder was manufactured by spray pyrolysis followed by calcination at 800 °C and ball milling (CerPoTech, Norway). A polyacrylate binder (Paraloid B-60 and B-72, Kall–Nor AS, Norway) was added to the powder which was then uniaxially cold-pressed at 200

MPa in a cylindrical die of diameter 13 mm. Sintering at 1350 °C for 4 hours yielded ceramic discs with a relative densities >98%. These were mounted into a dissolvable resin (Demotec 33, Demotec, Germany), ground using Al_2O_3 grinding paper, and finally polished down to 1/4 μm using diamond abrasive (DP-spray P, Struers, Denmark).

The microstructure was studied by Scanning Electron Microscopy (SEM) (Quanta FEG 200, FEI), and the grain size was measured by means of Electron Backscatter Diffraction (EBSD) (camera CD-200 Nordiff, EDAX software, Orientation Imaging Microscopy v5 Analysis 5.2). The composition of the samples was analysed by Energy-dispersive X-ray Spectroscopy (EDX) (Ametek EDAX, EDX, GENESIS Spectrum Ver. 5.11 software).

As Pr, Nd and Co sources, a few droplets of 0.05M water solution of the respective nitrate were applied on the polished LNO surface, and the discs were heated at 120 °C to evaporate the solvent. Relatively uniform, 1-2 μm thick surface layers of the nitrates were formed. For some samples, Co tracer was applied by Atomic Layer Chemical Vapour Deposition (ALCVD) ("F-120 Sat" reactor (ASM Microchemistry)) forming thin (~100 nm) dense films of CoO_x. Procedures for Co-ALCVD can be found elsewhere [17].

Choosing Pr, Nd and Co as chemical (impurity) tracers in this experiment was due to their similar ionic radii and similar valence under the specific reaction conditions; $r(Pr^{3+})$ = 112.6 pm and $r(Nd^{3+})$ = 110.9 pm compared to $r(La^{3+})$ = 116 pm, all 8-coordinated; and 6-coordinated $r(Co^{2+})$ = 65 pm, $r(Co^{3+})$ = 54.5 pm compared to $r(Ni^{2+})$ = 69 pm and $r(Ni^{3+})$ = 56 pm, respectively (according to Shannon [18]).

Two sets of annealing were performed. In the first set the diffusion annealing was performed in ambient air at 950, 1000, 1100, 1200, 1275 and 1350 °C, at each temperature for 10, 5, 3, 1 and 0.2 hours with Pr and Co tracers (Co tracer applied by ALCVD). In the second set the annealing was performed with Pr, Nd and Co tracers, also in air, but for longer periods; 50, 40, 30 and 20 hours at 950, 1100, 1200 and 1300 °C, respectively. Fast heating and cooling rates, 800 $°Ch^{-1}$ were used to avoid uncertainties introduced from diffusion during the temperature ramping. Moreover, to determine possible effects of pO_2 on the diffusion, some samples were annealed in argon and in intermediate pO_2 (5.5×10^{-3} atm O_2) obtained by mixing oxygen with argon.

As surface roughness may cause uncertainties in deconvolution of the profiles, the residual chemical tracer layers were removed by lightly polishing the surface, controlled by checking the surface with optical microscope and cross-section with SEM.

The concentrations of the Pr, Nd and Co tracers along with the host metals La and Ni in the depth-profiles were measured by SIMS using a CAMECA IMS7f micro-analyser. 10 keV O^{2+} ions were used as a primary beam rastered over a surface area of 150 × 150 μm, where the secondary ions were collected from the central 32 μm of the craters using an optical gate. In addition, electronic gating (80%) was also applied in order to reinforce the optical gate. Crater depths were measured with a Dektak 8 stylus profilometer, and the erosion rate was assumed to be constant when converting sputtering time to sample depth. The crater profiles revealed uniform crater bottoms more than 90 and 80 μm wide for crater depths above 30 and 45 μm, respectively. Moreover, some samples were examined by a variable electronic gating possibility of the Cameca IMS7f. When applying a 94% gating, i.e., excluding 94% of the image and extracting data from the central 6% of the examined region, the obtained profiles confirmed previous measurements with a lower restriction on the electronic gating.

Evolution of SIMS profiles for Pr and Co chemical tracers as a function of temperature for different annealing times are displayed in Figure 1a (Pr) and b (Co). The initial steep part of the concentration profiles is due to the drop in tracer concentration at the surface, and irregularities that appear in some of the profiles in the same region may come from surface and instrument artefacts. Anyhow, this part does not influence significantly the estimation of the diffusion coefficient, which is based on the deeper parts of the profiles. The SIMS signal intensity of each element is proportional to its concentration, and the depth is calculated from the crater profiles (Figure 2a and b).

Figure 3 shows the logarithm of the Nd signal intensity (proportional to the concentration), normalised towards the La intensity, as a function of the square of the depth, x^2. Figure 4a and b present the log of the Co signal intensity normalised with respect to the Ni matrix signal as a function of x^2 in the outer region, and $x^{6/5}$ in the deep region, respectively, in order to estimate bulk and grain boundary diffusion coefficients from the obtained slopes. Note that these are the same data as plotted over the entire profile in Figure 1.

Cross-sections of some samples were mapped by Electron Probe Micro Analysis (EPMA) (Cameca SX100) for tracer distribution, in order to visualise diffusion paths.

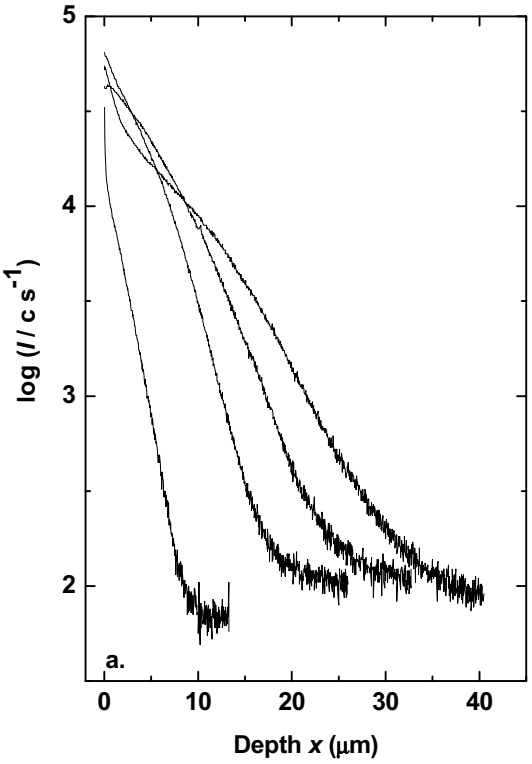

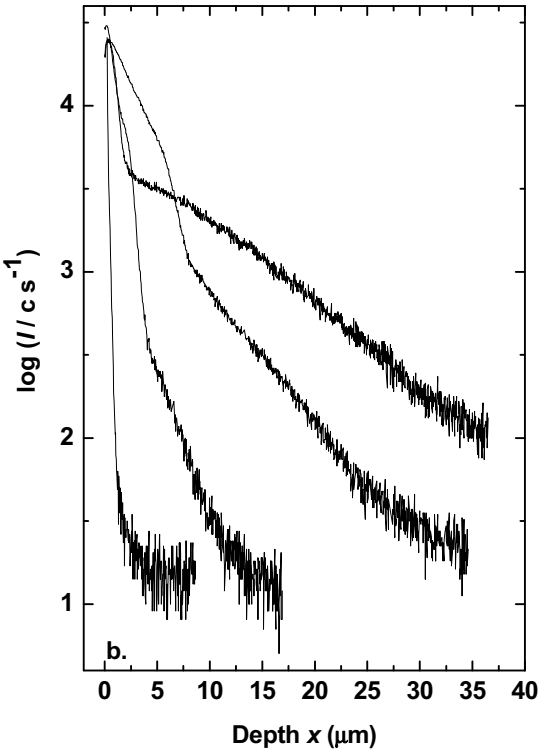

Figure 1. (a.) Pr and (b.) Co chemical (impurity) tracers depth profile evolution, after annealing at 950, 1100, 1200 and 1300 °C for 50, 40, 30 and 20 hours, respectively.

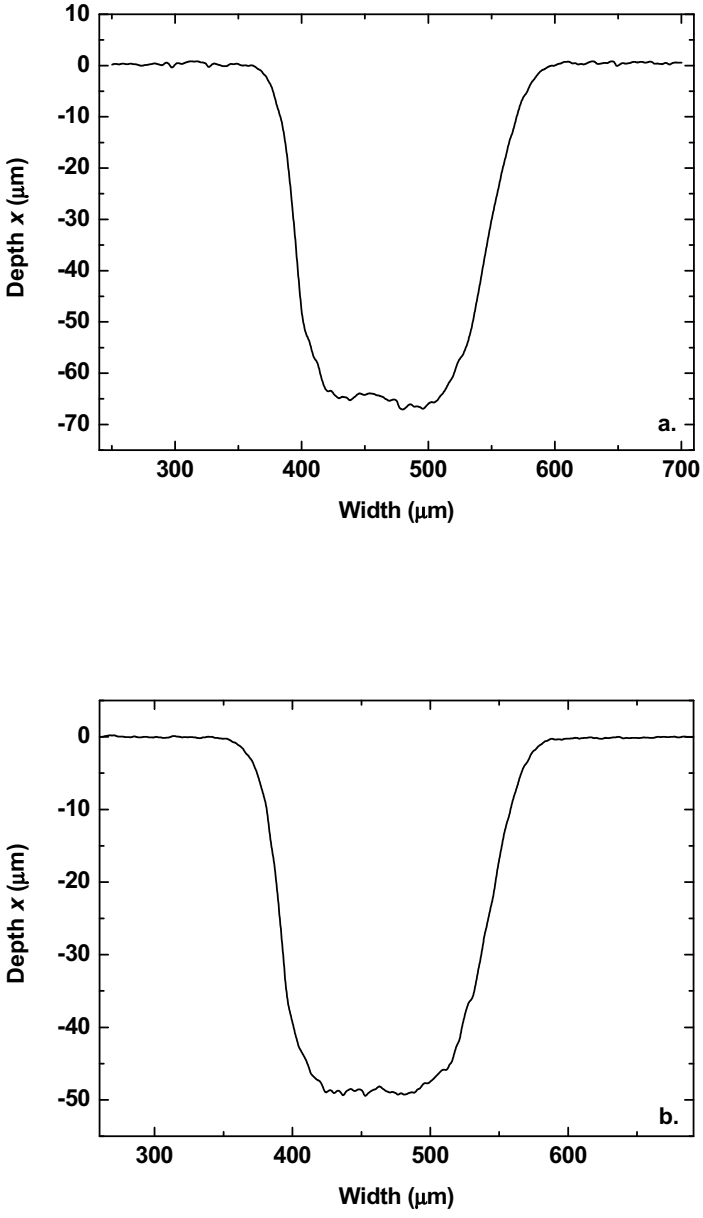

Figure 2. Crater depth profiles after ion sputtering samples with Nd (a.) and Co (b.) chemical tracers.

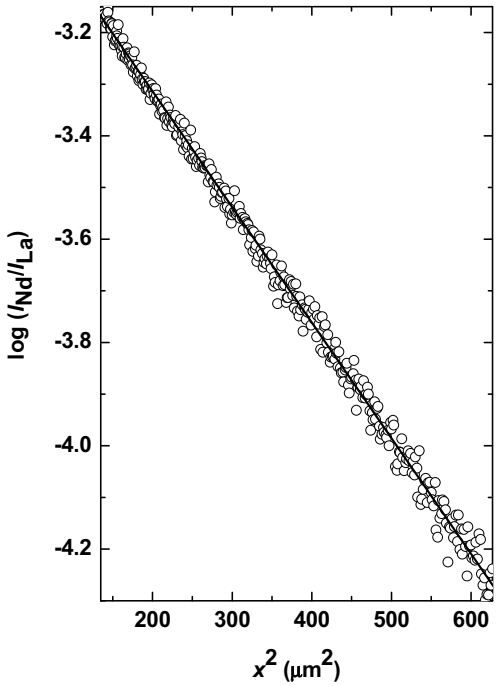

Figure 3. Depth profiles for Nd tracer in LNO and extracted fitting for the bulk (log (I_{Nd}/I_{La}) versus x^2) diffusion, for the sample annealed at 1300 °C for 20 hours.

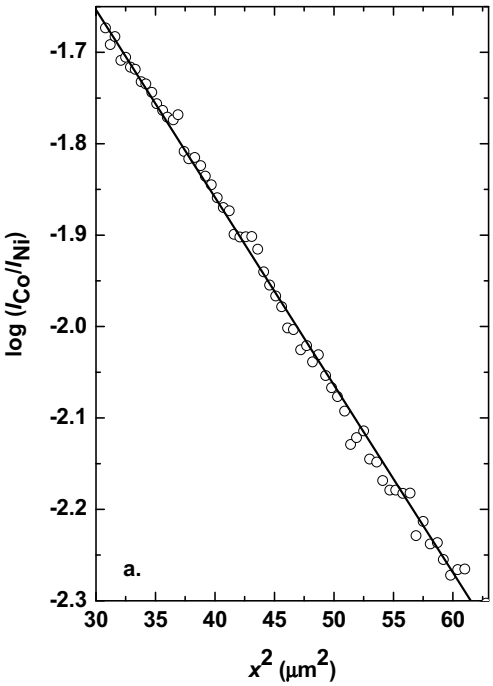
-1.7
-1.8
-1.9
-2.0
-2.1
-2.2
-2.3
log (I_Co/I_Ni)
a.
30
35
40
45
50
55
60
x^2 (μm^2)

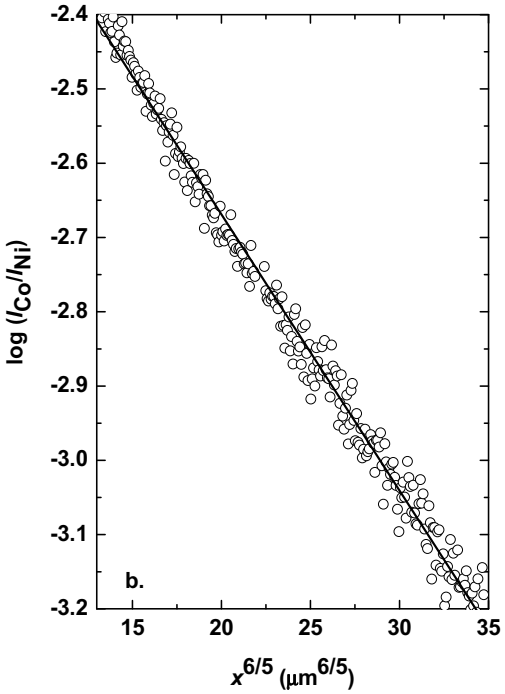

Figure 4. Depth profile for Co tracer in LNO for the sample annealed at 1200 °C for 30 hours. The data are the same as shown as one graph in Fig. 3b, but here plotted in two regions for extraction of (a.) the bulk diffusion coefficient (log (I_{Co}/I_{Ni}) versus x^2) and (b.) the grain boundary diffusion coefficient (log (I_{Co}/I_{Ni}) versus $x^{6/5}$).

3. Results and Discussion

3.1 Qualitative overview of experimental results

Figure 5 shows the SEM image of a cross-sectional fracture of a sintered LNO sample. No open porosity is observed, and 'false grain boundary diffusion' caused by open porosity [19] can be excluded. The average grain size after sintering is ~10 μm, as determined from the EBSD micrograph in Figure 6 and corrected for the flat plane observation by a factor of 1.35. The grain size was observed to increase by 20 – 30 % during the diffusion annealing at the highest temperatures.

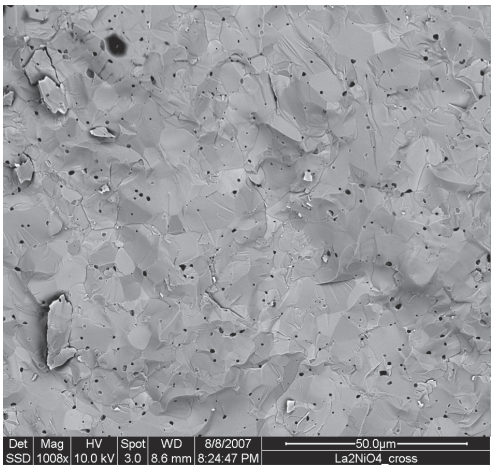

Figure 5. SEM image of a fracture surface, showing microstructure of the sample interior.

Due to the polycrystalline nature of the LNO samples, both bulk and grain boundaries contribute as modes of transport. Nevertheless, the depth profiles of the Pr and Nd chemical tracers show only one broad region that corresponds to simultaneous bulk and grain boundary diffusion (cf. Figure 1a). This is in contrast to the Co depth profiles where two regions are clearly distinguishable (cf. Figure 1b): The near-surface sharp decrease in the diffusant signal represents the short penetration depth via grain interior diffusion and the tail-like deeper penetration where the concentration decreases less steeply reflects transport along grain boundaries.

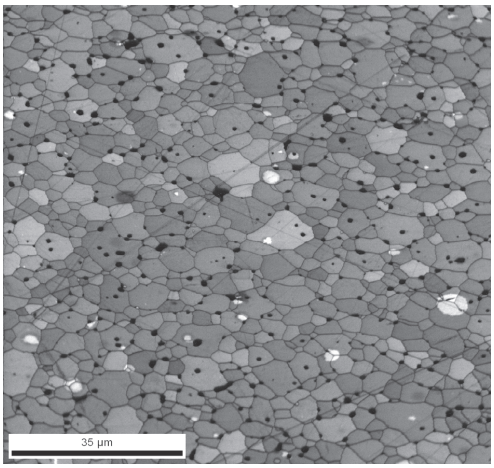

Figure 6. EBSD micrograph of a polished surface of sintered LNO. The black spots are areas that EBSD could not characterise. The straight lines are marks from polishing. Observed average grain size is ~10 µm.

Figure 7 shows an EPMA cross-sectional tracer mapping of the region close to the surface of samples coated with Pr (a) and Co (b) after annealing at 1350 °C for 20 and 5 hours, respectively. High intensity signal of the Pr tracer is observed only near the surface of the sample in Figure 7a, while that of Co appears also deeper into the bulk material with a pattern that reflects essentially the grain boundaries of the material, Figure 7b. Both these observations are in qualitative agreement with the conclusions above based on the depth profiles from SIMS.

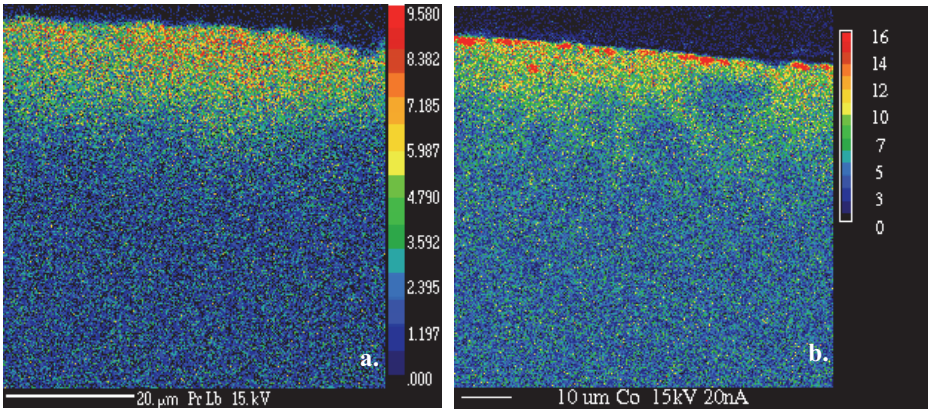

Figure 7. EPMA maps of Pr (a.) and Co (b.) chemical tracers, annealed for 20 and 5 hours at 1350 °C, respectively.

3.2 Analysis and interpretation of SIMS profiles

Cation transport in a polycrystalline material can be represented by the so-called effective diffusion coefficient, D_{eff} defined by Hart [20] as

$$D_{\text{eff}} = gD_{\text{GB}} + (1-g)D_{\text{B}} \quad \textbf{1}$$

D_{eff} represents, as such, the apparent diffusion coefficient, while D_{GB} and D_{B} are the grain boundary and bulk diffusion coefficients, respectively [21]. g is given by the volume fraction of grain boundaries in the polycrystal [22]:

$$g \approx 3\frac{w}{d} \quad \textbf{2}$$

where w is the grain boundary width and d is the grain diameter. Harrison differentiated [23], depending on the relative influence of grain interior and grain boundary diffusion, between “A”-, “B”- and “C”-type kinetic regimes. These three regimes result in different typical SIMS profiles of in-diffusing elements, such as for the chemical tracers in this work [23, 24]. In an “A”-type regime the inward penetration depth of the diffusant is considerably larger than the grain size resulting in essentially uniform in-diffusion. “B”-type regime covers situations where diffusion along grain boundaries is enhanced as compared to bulk of the material, whereas “C”-type diffusion reflects the rare case of pure grain boundary diffusion.

Different mathematical treatments are required to derive diffusion coefficients from profiles of the three regimes. Since under the “A”-type regime a homogenous diffusion front results, the concentration profiles follow solutions of Fick’s second law [25]. Under the boundary conditions for a thin-film source, the concentration of the diffusant at position x at time t, $C(x,t)$ is then given as:

$$C(x,t) = C_0(t)\exp(-\frac{x^2}{4Dt}) \quad \textbf{3}$$

where D here represents D_{eff}, which is essentially equal to D_{B} for the “A”-type kinetic. C_0 is the surface concentration of the diffusant. For “B”-type kinetics, the full mathematical solution becomes complex. One usually divides the concentration depth profile graphically

into the outer shallow part where the lateral concentration is essentially uniform and treats this part similarly as for "A"-type. The tail-like deeper penetration that represents a combination of in-diffusion along the grain boundaries and lateral leakage from the boundaries into the grains, can be approximated by Whipple-Le Claire's equation [23, 26]

$$swD_{\mathrm{GB}} = 0.3292\sqrt{\frac{D_{\mathrm{eff}}}{t}}\left(-\frac{\partial \log C}{\partial x^{6/5}}\right)^{-5/3} \quad \textbf{4}$$

where s is the segregation factor, t is annealing time and x is penetration depth. Now turning back to the depth profiles (representative examples are shown in Figure 1), the La-site (Pr and Nd) profiles yield only one region and represents as such "A"-type kinetics. The Ni-site (Co) profiles include the two regions typical for "B"-type kinetics. According to Eqs. 3 and 4, bulk and grain boundary diffusion coefficients can be estimated from the slopes obtained by plotting the logarithm of SIMS signal intensity (proportional to the concentration) as a function of x^2 and $x^{6/5}$, respectively (cf. Figures 3 and 4).

The diffusion coefficients extracted from the fitting, under the assumption that the grain boundary width w is 1 nm and s is unity, are presented in Table 1 and plotted in Arrhenius representations in Figure 8. From these, the diffusion coefficients for the different elements and transport modes in LNO can be represented as in the following.

For La site bulk diffusion, Fig. 8a, we have:

$$D_{\mathrm{Pr}}^{\mathrm{1st}}(\mathrm{cm}^2/\mathrm{s}) = 10^{-5.6\pm0.6}\exp\left(-\frac{178\pm17\mathrm{kJ/mol}}{RT}\right) \quad \textbf{5}$$

$$D_{\mathrm{Pr}}^{\mathrm{2nd}}(\mathrm{cm}^2/\mathrm{s}) = 10^{-6.3\pm0.4}\exp\left(-\frac{147\pm15\mathrm{kJ/mol}}{RT}\right) \quad \textbf{6}$$

$$D_{\mathrm{Nd}}(\mathrm{cm}^2/\mathrm{s}) = 10^{-5.7\pm0.4}\exp\left(-\frac{167\pm13\mathrm{kJ/mol}}{RT}\right) \quad \textbf{7}$$

where R is the gas constant and T the absolute temperature. These show reasonable consistency with respect to magnitude and within the statistical errors also with respect to pre-exponential factor and activation energy. It is evident that Pr and Nd diffusivities are similar and we arrive at an average activation energy for La-site bulk diffusion of 165 ± 15 kJ/mol.

For Ni-site diffusion of Co as diffusant we have, for annealing in air, Figs. 8b and c:

$$D_{\mathrm{Co_B}}^{\mathrm{1st}}(\mathrm{cm^2/s}) = 10^{-1.5\pm0.9}\exp(-\frac{299\pm24\mathrm{kJ/mol}}{RT}) \quad \textbf{8}$$

$$D_{\mathrm{Co_B}}^{\mathrm{2nd}}(\mathrm{cm^2/s}) = 10^{-1.7\pm0.4}\exp(-\frac{290\pm12\mathrm{kJ/mol}}{RT}) \quad \textbf{9}$$

$$D_{\mathrm{Co_{GB}}}^{\mathrm{1st}}(\mathrm{cm^2/s}) = 10^{6.4\pm0.4}\exp(-\frac{402\pm10\mathrm{kJ/mol}}{RT}) \quad \textbf{10}$$

$$D_{\mathrm{Co_{GB}}}^{\mathrm{2nd}}(\mathrm{cm^2/s}) = 10^{4.9\pm0.4}\exp(-\frac{360\pm23\mathrm{kJ/mol}}{RT}) \quad \textbf{11}$$

We assign average apparent activation energies of 295±15 kJ/mol and 380±20 kJ/mol for diffusion of Co tracers in bulk and grain boundaries, respectively, presumably on Ni-site.

Table 1. The bulk and grain boundary diffusion coefficients and the critical parameters α and β for ^{59}Co, ^{141}Pr, and ^{144}Nd chemical (impurity) tracers.

T (K)	D_B (cm^2 s^{-1})		D_{GB} (cm^2 s^{-1})		α (1st)	β (1st)
^{59}Co	1st set	2nd set	1st set	2nd set		
1223	7.98×10^{-15}	7.26×10^{-15}	1.60×10^{-11}	5.76×10^{-11}	0.0063	132.63
1273	1.39×10^{-14}	-	6.71×10^{-11}	-	0.0065	33.46
1373	1.09×10^{-13}	1.41×10^{-13}	9.68×10^{-10}	1.48×10^{-09}	0.0033	165.16
1473	5.29×10^{-13}	1.13×10^{-12}	1.77×10^{-08}	2.57×10^{-08}	0.0029	240.78
1548	1.64×10^{-12}	-	5.61×10^{-08}	-	0.0025	269.17
1573	-	3.67×10^{-12}	-	1.25×10^{-07}	-	-
1623	1.51×10^{-11}	-	2.39×10^{-07}		0.00035	33.09
^{141}Pr	1st set	2nd set				
1223	4.12×10^{-14}	2.33×10^{-13}	-	-	-	-
1273	1.49×10^{-13}	-	-	-	-	-
1373	5.84×10^{-13}	7.98×10^{-13}	-	-	-	-
1473	9.78×10^{-13}	2.44×10^{-12}	-	-	-	-
1548	3.12×10^{-12}	-	-	-	-	-
1573	3.35×10^{-12}	5.78×10^{-12}	-	-	-	-
1623	4.12×10^{-14}	-	-	-	-	-
^{144}Nd						
1223	1.72×10^{-13}	-	-	-	-	-
1373	7.29×10^{-13}	-	-	-	-	-
1473	2.38×10^{-12}	-	-	-	-	-
1573	6.73×10^{-12}	-	-	-	-	-

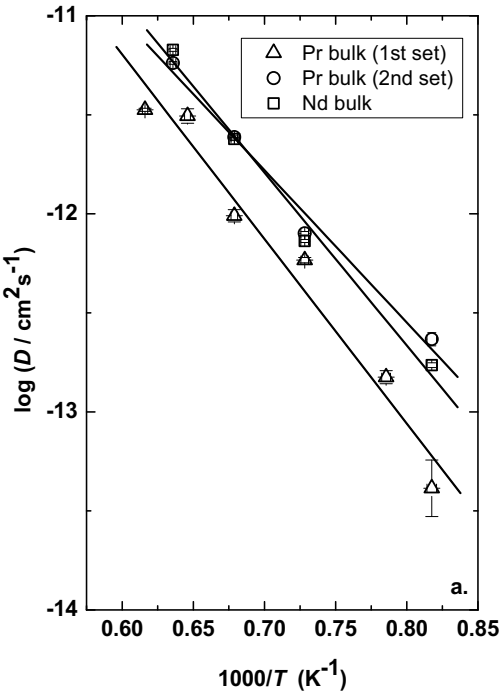
Pr bulk (1st set)
Pr bulk (2nd set)
Nd bulk
a.
log (D / cm2s-1)
1000/T (K-1)
-11
-12
-13
-14
0.60
0.65
0.70
0.75
0.80
0.85

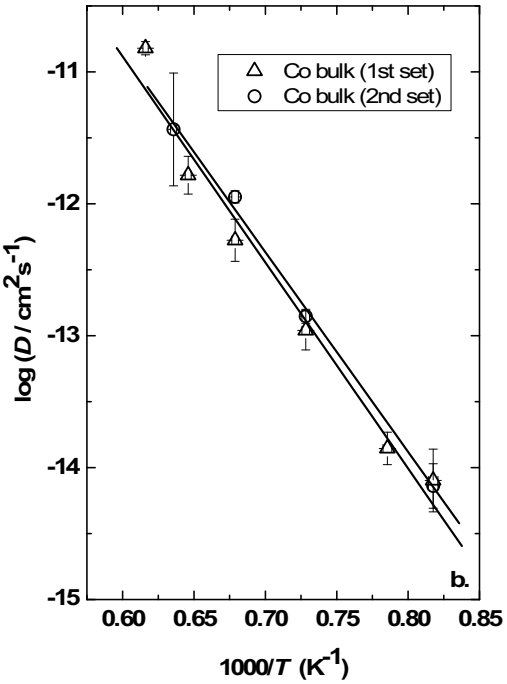
Co bulk (1st set)
Co bulk (2nd set)
b.
log (D / cm²s⁻¹)
1000/T (K⁻¹)
-11
-12
-13
-14
-15
0.60
0.65
0.70
0.75
0.80
0.85

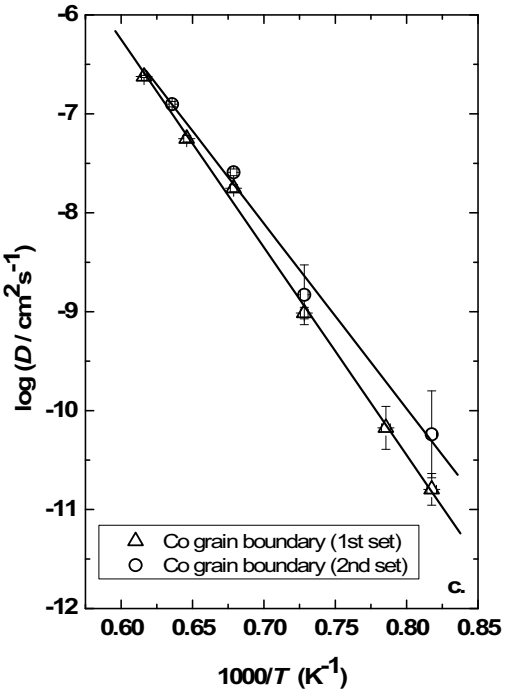
-6
-7
-8
-9
-10
-11
-12
log (D / cm2s-1)
0.60
0.65
0.70
0.75
0.80
0.85
1000/T (K-1)
Co grain boundary (1st set)
Co grain boundary (2nd set)
c.

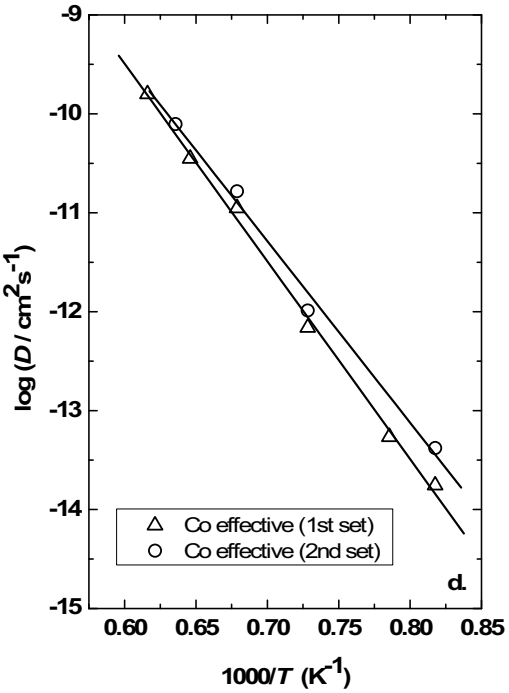

Figure 8. The diffusion coefficients of (a.) bulk Pr (1st and 2nd set) and Nd, and (b.) bulk, (c.) grain boundary and (d.) effective Co (1st and 2nd set) chemical tracers in LNO annealed in air.

The data show consistently higher diffusivities, higher pre-exponentials, and higher activation energies for grain boundary diffusion as compared to bulk, and for Ni-site bulk diffusion as compared to La-site bulk diffusion of Pr and Nd. These trends are all the same as established also by inter-diffusion experiments [27].

From D_B and D_{GB}, critical values α and β can be calculated using the following equations

$$\alpha = \frac{sw}{2\sqrt{D_B t}} \qquad \textbf{12}$$

$$\beta = \frac{swD_{GB}}{2D_B\sqrt{D_B t}} \qquad \textbf{13}$$

α and β represent the ratio of the bulk and grain boundary diffusion to the apparent, effective diffusion coefficient, respectively and they are also presented in Table 1. β values larger than 10 are required to apply Eq. 4 (Whipple-Le Claire) for the determination of D_{GB} [23] – a criterion met within the present experimental window.

The effective diffusion coefficient (Eq. 1) for the Co chemical tracer can in the present experimental window and for a grain size of 10 μm be approximated by (Fig. 8d):

$$D^{1st}_{Co_{eff}}(cm^2/s) = 10^{2.5\pm0.4}\exp(-\frac{383\pm10 kJ/mol}{RT}), \quad \textbf{14}$$

$$D^{2nd}_{Co_{eff}}(cm^2/s) = 10^{1.5\pm0.4}\exp(-\frac{351\pm22 kJ/mol}{RT}), \quad \textbf{15}$$

Effects of the oxygen partial pressure (pO_2) on the Co chemical (impurity) tracer diffusion coefficient were investigated at 1100 °C by annealing in Ar (pO_2 ~10 ppm), air, and in the intermediate pO_2 (5.5×10^{-3} atm O_2). The pressure dependences for the bulk and grain boundary coefficients are presented in Figures 9 and 10, which, moreover, compare the temperature dependences in Ar and air in the temperature range 1000 to 1350 °C. The functional oxygen pressure dependence is essentially the same for both bulk and grain boundary transport and does not seem to change within the present temperature window. The diffusion coefficients are roughly proportional to $pO_2^{-1/5.6}$ for bulk diffusion and $pO_2^{-1/5.0}$ for grain boundary diffusion. This is the opposite sign of the slope of what is expected for diffusion by cation vacancies. Thus, it may be that cation interstitials are in fact involved as the mobile species, or as limiting part of a complex jump mechanism involving more than one defect, as proposed by De Souza *et al*. [28]. It may be noted that the predominance of the vacancy mechanism is indeed confirmed in our inter-diffusion experiment by formation of the Kirkendall porosity [27]. Another possibility is that the unexpected pO_2-dependency may reflect an effect of the reduction in oxidation state and less covalent bonding of the Co diffusant as pO_2 decreases, or it may reflect a steric effect on cation vacancy mobility by the changing oxygen excess and lattice parameters of the oxide.

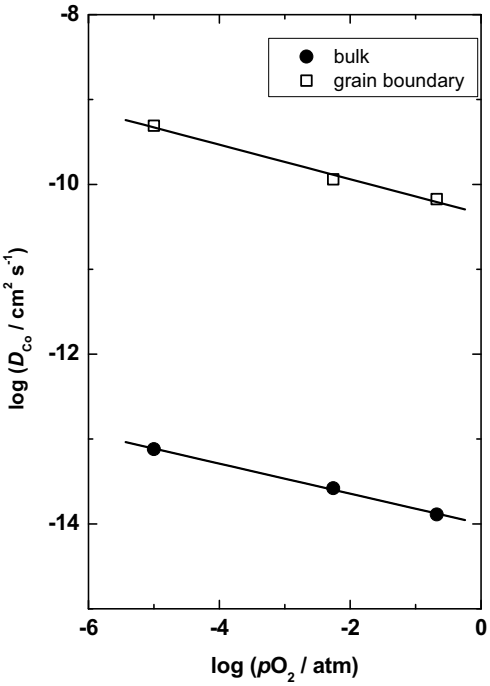

Figure 9. pO_2 dependency of the Co chemical tracer diffusion into LNO. The samples with the Co tracer were annealed in air, intermediate pO_2 and in argon, at 1100 °C.

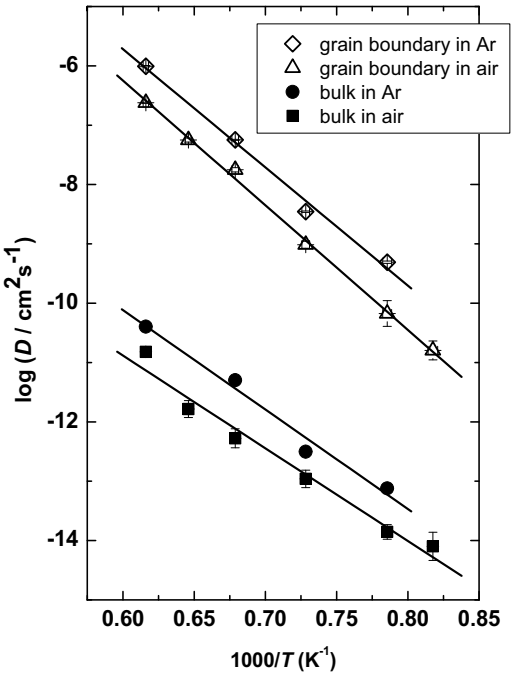

Figure 10. Comparison between diffusion coefficients of Co chemical (impurity) tracer annealed in air and argon.

3.3 Comparison with data from literature

Although cation diffusion is important to the overall durability of oxidic membranes, there is surprisingly little data and fundamental studies of these transport phenomena. In Figure 11 we compare data for cation diffusion on ternary oxides. There is so far only one other study of cation diffusion in K_2NiF_4-type materials: Palcut *et al.* [41] showed by SSR between La_2O_3 and CoO at 1300 °C that growth of La_2CoO_4 is determined by Co diffusion across the product layer. This coincides with observation from our SSR investigations for LNO [29] and Ni and Co diffusivity in these two K_2NiF_4-type materials were of similar magnitude. In a comparison of K_2NiF_4-type perovskite-related materials with ABO_3 perovskites we first notice that Palcut *et al.* [41] observed rather similar Co diffusivities in $LaCoO_3$ as encountered here for LNO. Unfortunately, there are no data on cation diffusion

in $LaNiO_3$. Anyhow, in ABO_3 perovskite materials, the B-site cation is most commonly encountered as the faster moving ion, except for $LaCrO_3$ [14]. When comparing the activation energies for cation diffusion in the LNO system from the present study with those for the ABO_3 perovskites, we find that they exhibit similar values. In comparison with a number of rare-earth manganites [30], cobaltites [41] and ferrites [33] as well as perovskites (cf. Figure 11), the magnitude of the diffusivities of Pr, Nd and Co chemical tracers in LNO are on the high side.

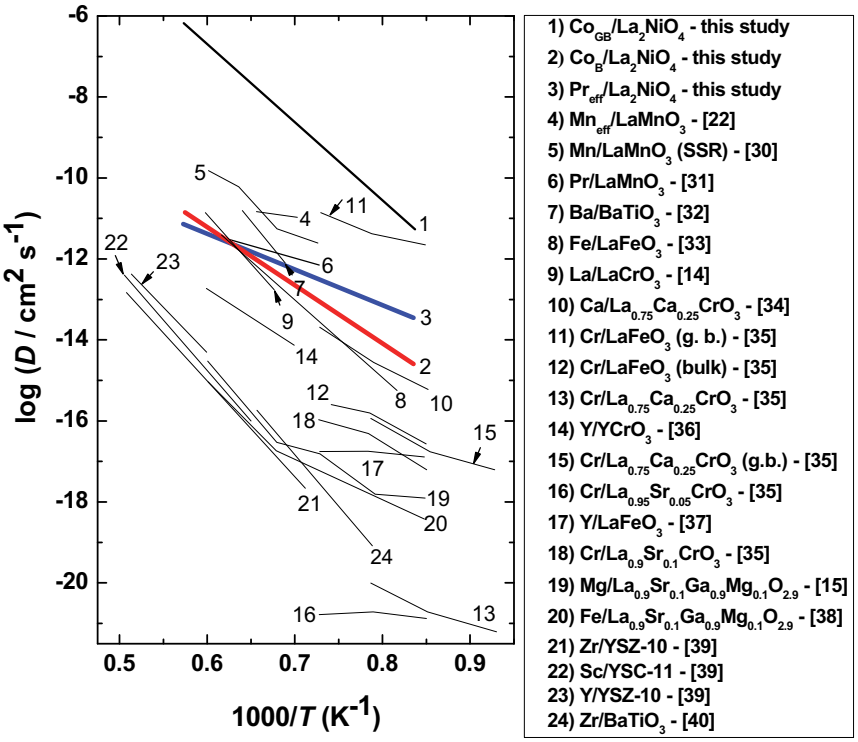

Figure 11. Values for the diffusion coefficient of Co and Pr chemical (impurity) tracers compared with data for cation diffusion coefficients of various perovskite and perovskite-related materials from the literature.

3.4 Analysis of bulk diffusion

From Figures 8a and b we may notice that the bulk diffusivities for La- and Ni-site are of similar magnitude. However, although similar in diffusivity, the activation energies for diffusion coefficients of the chemical tracers in the bulk are rather low. This is particularly so, if the experimental values from these data should represent both formation and migration enthalpies of the La and Ni vacancies. One may speculate that this may reflect a correlation in the attempt jump frequency, different defect chemistries, or statistical uncertainty in the measurements. Going into detail on the differences on the La- and Ni-site diffusion data for this system, one should also note the ~4 orders of magnitude difference between pre-exponentials (the same behaviour was observed in our inter-diffusion experiment [27]).

Next, we will consider vacancy concentration. Based on experimental and computational thermodynamic parameters for the defect reactions (anti-Frenkel disorder, oxygen intercalation, i.e., oxidation, and Schottky disorder [42, 43, 44]) the energy of formation of cation vacancies is estimated to be in the order of ~350 kJ/mol (per defect). The literature values for the energy of migration of A-site cations are similarly high (in order of > 400 kJ/mol [16, 28, 45]). Our experimentally obtained small activation energy for the La-site then suggests that the concentration of the La-site defects (normally presumed to be vacancies) is essentially constant. In contrast, our higher activation energies for Ni-site bulk diffusion suggest that Ni-sites activation energy may comprise both enthalpy terms – for formation and migration of defects, i.e., that the defect concentration equilibrates. Equilibration of defects requires creation (or annihilation) of new unit cells, so one my anticipate formation of secondary phase segregation along grain boundaries. Such a difference in defect chemistry (frozen versus equilibrium) would explain the orders of magnitude difference between the pre-exponentials of the La- and Ni-site diffusivities.

4.3 Analysis of grain boundary diffusion

Now turning to grain boundary diffusion of the Co chemical tracer, which activation energy is considerably higher than the bulk values, which is rather counter-intuitive. However, such high activation energies for grain boundary diffusion have also been observed by Waller *et al.* [46] for Mn diffusion in YSZ and by Kilo *et al.* [47] for Ca, Y and Zr in Ca and Y doped zirconia. It was speculated that the mixed oxidation state of the

respective cations and/or the formation of a secondary inter-granular phase caused this behaviour.

We may in any case suggest that because of equilibration of Ni-site defects, the high activation energy of the grain boundary diffusion coefficients may contain enthalpies of both formation and migration of the defects.

4. Concluding remarks

Pr, Nd and Co chemical (impurity) diffusion was studied in polycrystalline LNO by annealing in the temperature range from 950 to 1350 °C for durations from 0.2 to 50 hours. Depth profiles of the chemical tracer concentration were determined by means of SIMS.

From the shape of the concentration profiles and supported by EPMA mapping, the La- and Ni-site tracer diffusion in LNO were according to the Harrison's classification concluded to follow "A"-type (Pr and Nd), i.e., bulk diffusion and "B"-type (Co) diffusion kinetics, i.e., enhanced grain boundary diffusion. Consequently, only the bulk (effective) diffusion coefficient could be determined for Pr and Nd, whereas for Co, both bulk and grain boundary diffusion coefficients could be extracted from the measurements.

The determined average apparent activation energies for the respective processes are 165±15 kJ/mol for La-site bulk diffusion, 295±15 kJ/mol for Ni-site bulk diffusion, and 380±20 kJ/mol for Ni-site grain boundary diffusion. The rather low activation energies for the bulk diffusion for the Pr and Nd chemical tracers are suggested to be due to the constant concentration of La-site vacancies, i.e., the activation energy for the Li-site bulk diffusion coefficient reflects the enthalpy of migration only. It is suggested that the concentration of Ni-site vacancies is equilibrated through enhanced grain boundary transport, with segregation of secondary phases along grain boundaries. This may explain the higher activation enthalpies and orders of magnitude higher pre-exponentials especially for grain boundary diffusion, but also bulk diffusivity on the Ni-site.

Overall, the results obtained in this work on the chemical tracers, are comparable with our results from SSR and inter-diffusion techniques [27, 29].

5. Acknowledgements

Financial support under the project "162316 Demonstration of AZEP Reactor Module" of the Research Council of Norway (RCN) and Statoil is acknowledged. Dr. L. Vines (MiNa Lab, Centre for materials science and nanotechnology (SMN), University of Oslo (UiO)) is thanked for SIMS analyses, Dr. A. Magrasó (FERMiO, SMN, UiO) is thanked for help with EBSD, and M.M.L. Erambert (Dept. Geosciences, UiO) is thanked for EPMA analyses. Assoc. Prof. R. Haugsrud, Prof. T. Norby, and Dr. Zuoan Li (FERMiO, SMN, UiO) are thanked for reading the manuscript and for valuable discussions.

7. References

[1] M. Martin, *J. Chem. Thermodynamics*, 2003, 35, 1291-1308.

[2] J. Wolfenstine, *Solid State Ionics*, 1999, 126, 293-298.

[3] V. V. Kharton, E. V. Tsipis, E. N. Naumovich, A. Thursfield, M. V. Patrakeev, V. A. Kolotygin, J. C. Waerenborgh, I. S. Metcalfe, *J. Solid State Chem.*, 2008, 181, 1425-1433.

[4] J. B. Smith, T. Norby, *J. Electrochem. Soc*., 2006, 153(2), A233-A238.

[5] J. B. Goodenough, *Mat. Res. Bull.*, 1982, Vol. 17, 383-390.

[6] C. N. Munnings, S. J. Skinner, G. Amow, P. S. Whitfield, I. J. Davidson, *Solid State Ionics*, 2005, 176, 1895-1901.

[7] S. J. Skinner, J. A. Kilner, *Solid State Ionics*, 2000, 135, 709-712.

[8] X. Dong, Z. Wu, X. Chang, W. Jin, N. Xu, *Ind. Eng. Chem. Res.*, 2007, 46, 6910-6915.

[9] H. Ishikawa, Y. Toyosumi, K. Ishikawa, *J. Alloys Compd.*, 2006, 408-412, 1196-1199.

[10] V. V. Vashook, N. E. Trofimenko, H. Ullmann, L.V. Makhnach, *Solid State Ionics*, 2000, 131, 329-336.

[11]V. V. Kharton, A. P. Viskup, E. N. Naumovich, F. M. B. Marques, *J. Mater. Chem.*, 1999, 9, 2623-2629.

[12] C. Wagner, *Z. Phys. Chem.*, 1936, Abt. B 33-34, 309.

[13] H. Schmalzried, *Solid State Reactions*, Chapter 6, Verlag Chemie, Weinheim/Bergstr., 1974.

[14] T. Akashi, M. Nanko, T. Maruyama, *J. Electrochem. Soc.*, 1998, Vol. 145, No. 6, 2090-2094.

[15] O. Schulz, M. Martin, C. Argirusis, G. Borchardt, *Phys. Chem. Chem. Phys.*, 2003, 5, 2308-2313.

[16] J. B. Smith, T. Norby, *J. Am. Ceram. Soc.*, 2006, 89, 582-586.

[17] K.B. Klepper, O. Nilsen, H. Fjellvåg, *Thin Solid Films*, 2007, 515, 7772–7781.

[18] D. Shannon, *Acta Cryst.*, 1976, A32, 751-767.

[19] A. Atkinson, R. I. Taylor, *Philos. Mag. A*, 1981, vol. 43, no. 4, 979-998.

[20] E. W. Hart, *Acta Metall.*, 1957, 5, 597.

[21] J. H. Harding, *Interface Science*, 2003, 11, 81-90.

[22] S. Miyoshi, M. Martin, *Phys. Chem. Chem. Phys.*, 2009, 11, 3063-3070.

[23] L. G. Harrison, *Trans. Faraday Soc.*, 1961, 57, 1191-1199.

[24] I. Kaur, Y. Mishin, W. Gust, *Fundamentals of Grain and Interphase Boundary Diffusion*, John Wiley & Sons LTD, Chichester, 1995.

[25] J. Crank, *Mathematics of Diffusion*, Oxford University Press, 1979.

[26] C. Herzig, Y. Mishin, *Diffusion in Condensed Matter, Methods, Materials, Models*, editors P. Heitjans, J, Kärger, Springer, Berlin, 2005, p. 337.

[27] N. Čebašek, R. Haugsrud, T. Norby, *submitted to Sold State Ionics*.

[28] R. A. De Souza, M. S. Islam, E, Ivers-Tiffée, *J. Mater. Chem.*, 1999, 9, 1621-1627.

[29] N. Čebašek, R. Haugsrud, J. Milošević, Z. Li, J. B. Smith, A. Magrasó, T. Norby, *J. Electrochem. Soc.*, 2012, 159 (6), B702-B708.

[30] M. Palcut, K. Wiik, T. Grande, *J. Phys. Chem. C*, 2007, 111, 813.

[31] M. Palcut, J. S. Christensen, K. Wiik, T. Grande, *Phys. Chem. Chem. Phys.*, 2008, 10, 6544-6552.

[32] A. Kitahara, M. Nanko, K. Kawamura, T. Maruyama, *Proceedings - Electrochemical Society*, 2000, 99-38 (High Temperature Corrosion and Materials Chemistry), 534-545.

[33] J. B. Smith, T. Norby, *Solid State Ionics*, 2006, 177, 639–646.

[34] T. Horita, M. Ishikawa, K. Yamaji, N. Sakai, H. Yokokawa, M. Dokiya, *Solid State Ionics*, 1999, 124, 301-307.

[35] N. Sakai, K. Yamaji, T. Horita, H. Negishi, H. Yokokawa, *Solid State Ionics*, 2000, 135(1- 4), 469-474.

[36] K. Kawamura, A. Saiki, T. Maruyama, K. Nagato, *J. Electrochem. Soc.*, 1995, 142, 3073-3077.

[37] I. Wærnhus, N. Sakai, H. Yokokawa, T. Grande, M-A. Einarsrud, K. Wiik, *Solid State Ionics*, 2007, 178, 907-914.

[38] O. Schulz, S. Flege, M. Martin, *Proceedings - Electrochemical Society*, 2003, PV 2003-7 (Solid Oxide Fuel Cells VIII), 304-314.

[39] Y. M. Chiang, W. D. Kingery, *J. Am. Ceram. Soc.*, 1990, 73, 1153-1158.

[40] S. Koerfer, R. A. De Souza, H. I. Yoo, M. Martin, *Solid State Science*, 2008, 10, 725-734.

[41] M. Palcut, K. Wiik, T. Grande, *J. Phys. Chem.* B 2007, Vol. 111, 2299-2308.

[42] M. Read, S. Islam, F. King, F. Hancock, *J. Phys. Chem.*, B 1999, 103, 1558-1562.

[43] N. Naumovich, M. V. Patrakeev, V. V. Kharton, A. A. Yaremchenko, D. I. Logvinovich, F. M. B. Marques, *Solid State Science*, 2005, 7, 1353-1362.

[44] Z. Li, R. Haugsrud, J. B. Smith, T. Norby, *Solid State Ionics*, 2009, 180, 1433–1441.

[45] R. A. De Souza, *Phys. Chem. Chem. Phys.*, 2003, 5, 740-748.

[46] D. Waller, J. D. Sirman, J. A. Kilner, *Electrochemical Proceedings*, 1997, 97-40, 1140-1149.

[47] M. Kilo, M. A. Taylor, C. Argirusis, G. Borchardt, B. Lesage, S. Weber, S. Scherrer, H. Scherrer, M. Schroeder, M. Martin. *J. Appl. Phys*, 2003, 94, 7547-7552.

5.3 Paper III:

Determination of the Self-Diffusion Coefficient of Ni^{2+} in $La_2NiO_{4+\delta}$ by the Solid State Reaction Method

Authors: *Nebojša Čebašek, Reidar Haugsrud, Jovan Milošević, Zuoan Li, Jens B. Smith, Anna Magrasó, Truls Norby*

Journal of the Electrochemical Society, 159 (6) B702-B708 (2012)

5.4 Paper IV

Kinetic Decomposition of a $La_2NiO_{4+\delta}$ Membrane under an Oxygen Potential Gradient

Authors: *Nebojša Čebašek, Truls Norby, Zuoan Li*

Accepted in the *Journal of the Electrochemical Society*

Kinetic Decomposition of a $La_2NiO_{4+\delta}$ Membrane under an Oxygen Potential Gradient

Nebojša Čebašek, Truls Norby, Zuoan Li

University of Oslo, Department of Chemistry, Centre for Materials Science and Nanotechnology, FERMIO, Gaustadalleen 21, NO-0349 Oslo, Norway

Abstract

A dense ceramic $La_2NiO_{4+\delta}$ membrane was annealed under an oxygen potential difference $\Delta\mu_{O_2}$ between flowing O_2 and Ar at 1000 °C for 800 h. The membrane was afterwards analysed by means of SEM, EPMA, XPS and XRD. SEM and XPS analyses showed that NiO was segregated and randomly spread as new decomposition phase on the high pO_2 side. Pores had formed on the low pO_2 side without detectable phase change. The critical $\Delta\mu_{O_2}$ to initialise the decomposition of the LNO membrane was derived and expressed by kinetic and thermodynamic parameters. Based on the calculated critical $\Delta\mu_{O_2}$ and the observed experimental results, the ratio of effective diffusivities D_{La}/D_{Ni} in the ceramic material at 1000 °C was estimated to be slightly lower than 0.5. The oxygen flux remained mainly constant after an initial decrease during the annealing. Results from this work are in good agreement with our findings on cation diffusivity in $La_2NiO_{4+\delta}$ material obtained by solid state reaction, chemical tracer diffusion and inter-diffusion.

Keywords: $La_2NiO_{4+\delta}$; kinetic decomposition; cation diffusion; oxygen potential gradient.

1. Introduction

Lanthanum nickelate, $La_2NiO_{4+\delta}$ (LNO), as the first member in Ruddlesden-Popper's (RP) series ($A_{n+1}B_nO_{3n+1}$), is a mixed oxide ion and electron hole conductor with K_2NiF_4-type structure, and has attracted a lot of interests for its potential applications as cathodes of solid oxide fuel cells (SOFCs) at intermediate temperatures and as oxygen separation membranes at high temperatures.[1-4]

LNO transport properties and structure have been extensively studied for undoped and doped systems.[5-17] LNO crystallizes in tetragonal structure at temperatures above 150 °C, which can be visualised as layers of rock-salt (LaO) and perovskite ($LaNiO_3$) alternating along the *c*-axis,[11] or as stacking of La_2O_2 double layers and NiO_2 sheets.[18]

The undoped LNO was reported to exhibit a high oxygen flux.[19] Under practical operating conditions involving large oxygen potential gradients and temperatures of typically 1000 °C, oxygen is transported through LNO membrane via oxygen interstitials charge compensated by a simultaneous flow of electron holes. Structurally, oxygen interstitials are transported through rock-salt layer, while electron holes are formed in the perovskite layer as Ni^{3+}.[20] The oxygen potential gradient across the membrane not only drives oxygen transport, but also induces an opposite cation potential gradient and causes a movement of cations in the opposite direction than oxygen, i.e., they are moving towards the side with higher pO_2.[21-23] This can cause a membrane "walkout" (chemical creep, crystal shift) after a period of operation. Moreover, different diffusivities of cations may cause an initially homogeneous oxide to demix (e.g. $Co_{1-\delta}Mg_\delta O$),[24] or decompose (e.g. Ni_2SiO_4)[25] when the phase boundary is exceeded. This can cause a severe threat to materials' stability and lifetime when it comes to applications at high temperatures.[21-23] LNO can stand a considerable range of oxygen partial pressures at high temperatures when there is no oxygen gradient. However, the LNO stability has not been explored in an oxygen potential gradient at high temperatures to the best of our knowledge. Here we perform a long-term annealing in such a gradient and discuss the results in view of our earlier investigations on cation diffusion in LNO by solid state reaction (SSR), chemical tracer diffusion, and inter-diffusion.[26-28]

2. Experimental

The LNO powder was obtained from CerPoTech, Norway, who had prepared it by spray pyrolysis followed by calcination at 800 °C. The single phase of LNO powder was confirmed by X-ray diffraction (XRD). A polyacrylate binder was added to the powder and a disk pressed uniaxially in a 25 mm cylindrical die at ~120 MPa. After sintering at 1350 °C for 4 h, the obtained relative density was higher than 98%. The disk was then ground using Al_2O_3 paper and polished down to 1/4 μm on both sides, using diamond abrasive with suitable lubricants (DP-Lubricant Green/Red, Struers, Denmark). The final thickness of the disk was 0.9 mm.

The disk was mounted in a ProboStat^{TM} sample holder cell (NorECs, Norway) (schematically presented in Figure 1) and enclosed with an outer quartz tube. A gold gasket was used for sealing the disk as a membrane to the alumina support tube at 1058 °C using the cell's spring load system. The temperature was controlled using a type S thermocouple in the vicinity of the membrane. The gases were supplied directly to the membrane surfaces using the gas supply system of the ProboStat^{TM} cell. The sealing process was monitored by feeding the two sides of the membrane with He and Ar gases and monitoring the outlets using a Balzers QMG 421 quadrupole mass spectrometer (MS) with a secondary electron multiplier detector. When the sealing was satisfactory, the temperature was lowered rapidly to 1000 °C. At this temperature, the LNO membrane was annealed for 800 h under an oxygen gradient between flowing O_2 and flowing Ar.

After annealing the LNO membrane was examined by means of Scanning Electron Microscopy (SEM) (Quanta FEG 200, FEI) with EDAX Energy-dispersive X-ray Spectroscopy (EDX) (Ametek EDAX), Electron Probe Micro Analysis (EPMA) (Cameca SX100), X-ray Photoelectron Spectroscopy (XPS) (Kratos Axis Ultra^{DLD}) and XRD.

The EPMA instrument had a 15 kV 20 nA focused electron beam and 5 wavelength-dispersive spectrometers. Counting time per peak was 20 s plus 10 s on the background at each side of the peak. The calibration standards used were synthetic $LaPO_4$ for La Lα and NiO for Ni Kα. Before the EPMA measurement, the LNO membrane was mounted in epoxy resin and cut perpendicular to the surfaces. The cross-section of the membrane was analysed by 3 different line scans perpendicular to the membrane surface in the immediate

vicinity of the surfaces at each side of the membrane and in length of around 10 μm from the surfaces. The composition was measured approximately every 0.5 μm.

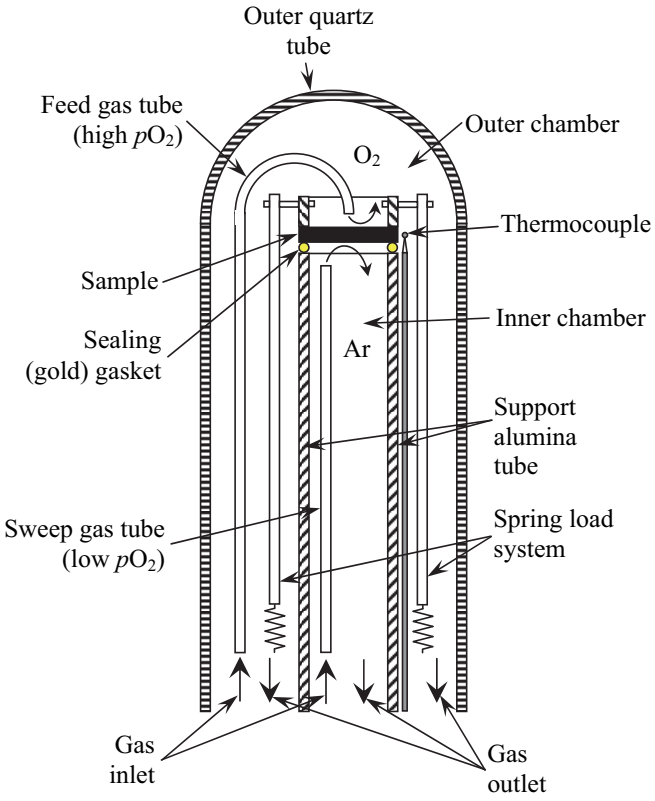

Figure 1. The scheme of the ProboStat™ setup for the decomposition experiment. The LNO membrane and gold gasket are located between the spring load system and the alumina support tube.

XPS spectra were recorded using monochromatic Al Kα X-ray radiation. The analyser pass energy was set to 40 eV, giving a resolution of 0.68 eV as determined by the full width at half maximum of the Ag $3d_{5/2}$ peak of pure silver. The energy scale was calibrated to better than 0.05 eV based on standard binding energy values for Au $4f_{7/2}$, Ag $3d_{5/2}$ and Cu $2p_{3/2}$.[29] The base pressure during the analyses was below 8×10^{-7} Pa.

In order to see more clear effect of the decomposition, EPMA and XPS measurements were also performed on a sample without annealing under an oxygen gradient (reference sample).

3. Results

The SEM image of the polished membrane surface before annealing is shown in Figure 2. Figures 3 and 4 present high and low pO_2 sides of the LNO membrane, respectively, after annealing under an O_2-Ar gradient. Spots of darker contrast at the backscattered image (lighter elemental composition) have seemingly appeared from the bulk on the high pO_2 side (Figure 3), while only pores can be observed on the low pO_2 side (Figure 4). By comparing EDX analysis of dark spots at the backscattered image with that of the rest of the sample (see Figure 5), it can be concluded that they are NiO. The particles of the new (NiO) segregated phase are randomly spread at the whole high pO_2 surface. Moreover, SEM investigation of the cross-section of the broken membrane after annealing does not show any phase segregation in the bulk material (cf. Figure 6).

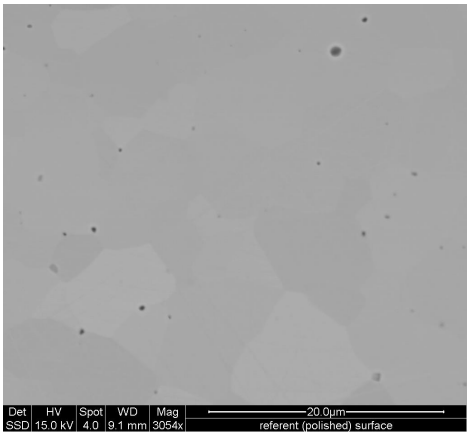

Figure 2. SEM micrograph of the polished membrane surface before annealing.

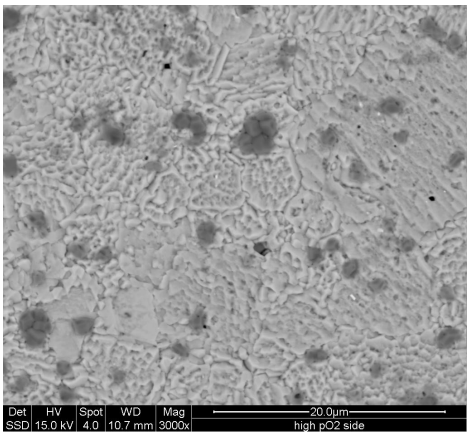

Figure 3. SEM backscattered image of the high pO_2 side of the LNO membrane after annealing at 1000 °C for 800 h. Dark spots represent the decomposition product (NiO).

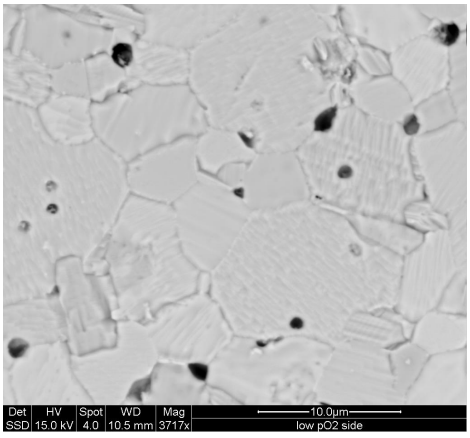

Figure 4. SEM backscattered image of the low pO_2 side of the LNO membrane after annealing at 1000 °C for 800 h. No phase change was detected at the low pO_2 side.

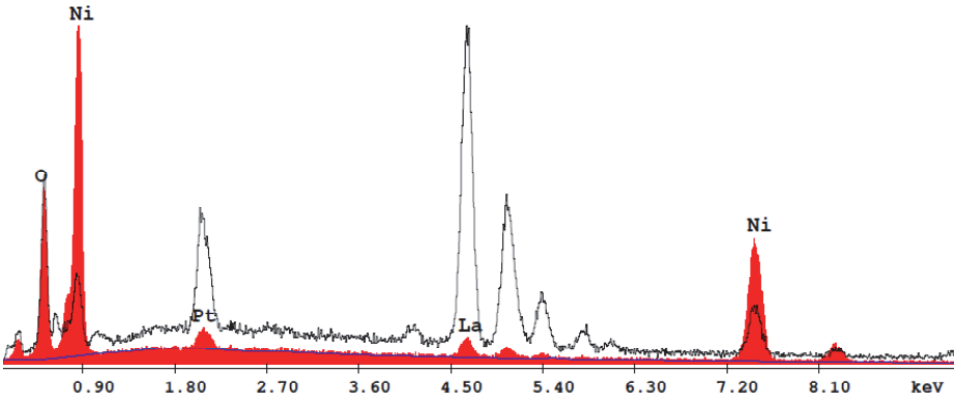

Figure 5. Comparison of EDX spectra between regions with dark colour at the backscattered image (red spectra) and the rest of the LNO membrane (colourless spectra) from Figure 3. The detected traces of Pt at the high pO_2 side of the membrane may be from the spring load system.

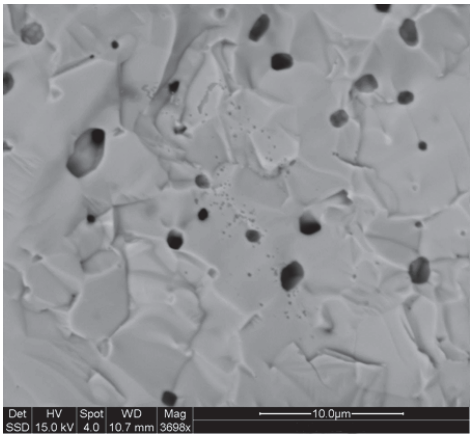

Figure 6. SEM backscattered image of the cross-section of broken LNO membrane, after annealing at 1000 °C for 800 h. No phase segregation was observed.

XPS spectra can be used to analyse the Ni concentration on the surface after the signal was normalised on La4d peak area with Shirley background subtraction. It confirms our findings from EDX analysis. Figure 7 shows the increase in binding energy of the Ni3p peak for the high pO_2 side of the LNO membrane, indicating the increasing Ni concentration. The high peak next to the Ni3p peak is Pt4f, showing traces of platinum on the high pO_2 side, which may originate from our spring load system connected and

fastened by platinum. Since no higher order RP phases were observed by XRD measurements of the annealed sample (Figure 8), we can exclude the catalytic effect of Pt on oxidizing LNO in this work, as found by Sayers *et al.*[30] Furthermore, such catalytic effect only happens in the case of direct contact between LNO and Pt, which is not our case. Therefore, the Pt contamination would most probably take place after the annealing measurement.

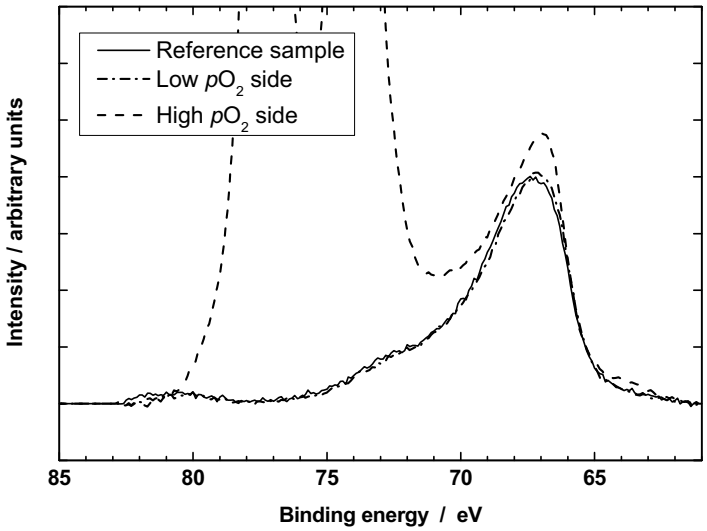

Figure 7. XPS spectra, indicating an increase in Ni concentration on the high pO_2 side, as compared to the low pO_2 side and the reference sample. Signals are normalised after La4d peak area with Shirley background subtraction.

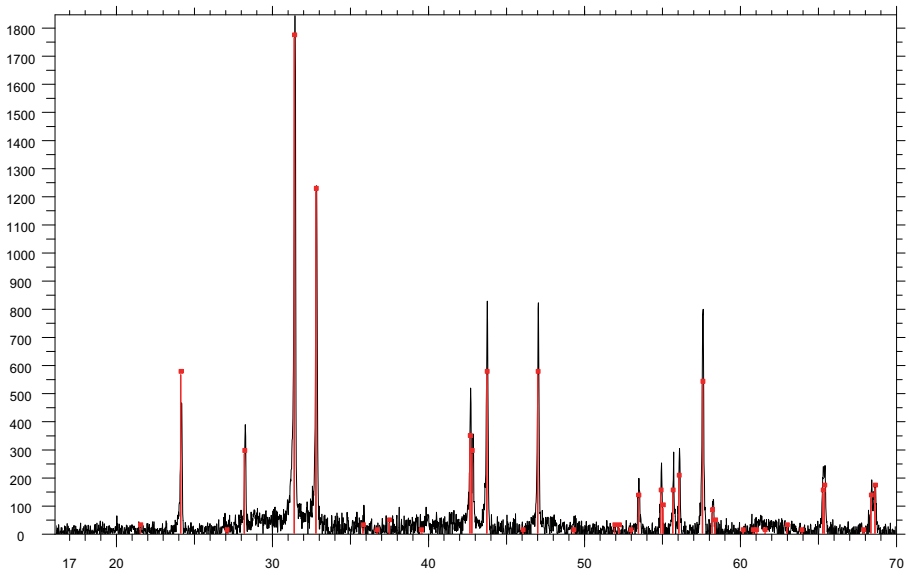

Figure 8. XRD pattern of the LNO membrane (high pO_2 side) after annealing at 1000 °C for 800 h.

The La concentration was also analysed in a similar way and the obtained spectra show that the high pO_2 side has less La than the low pO_2 side and the reference sample. As far as the low pO_2 side is concerned, neither XPS nor EDX shows any significant change in the concentration of both La and Ni on the surface.

The EPMA line scans of the LNO membrane cross-section in the immediate vicinity of both the high and low pO_2 sides are plotted in Figures 9 and 10. As compared to the reference sample and considering the detection limit, the concentration of both La and Ni does not show any variation in the bulk, indicating that no significant kinetic demixing occurs during the annealing. Therefore, the following discussion will mainly limit itself to kinetic decomposition of the LNO membrane.

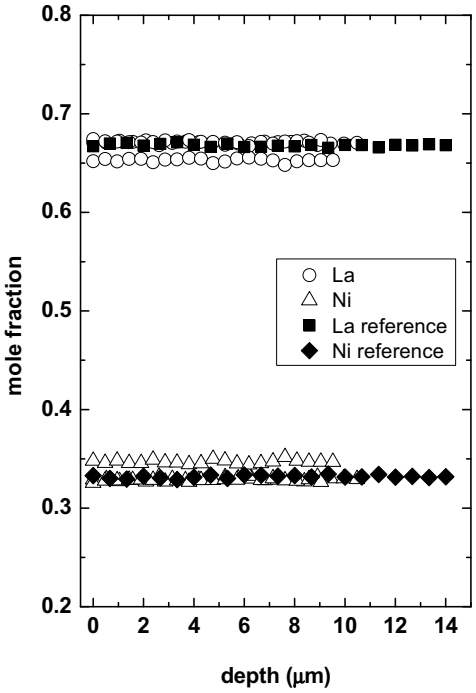

Figure 9. Atomic fraction of La and Ni among total cations versus depth on the high pO_2 side determined by EPMA.

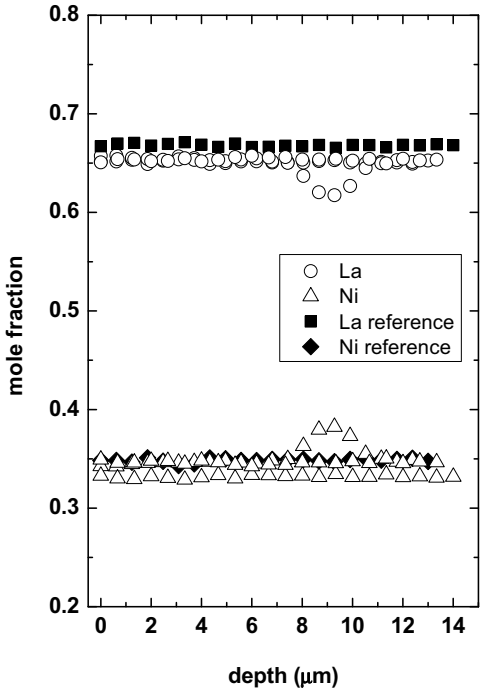

Figure 10. Atomic fraction of La and Ni among total cations versus depth on the low pO_2 side determined by EPMA.

4. Discussion

When an isothermal oxygen potential gradient is applied to the LNO membrane, it induces oppositely directed gradients in the chemical potentials of cations. As a result, the cations are transported in the direction of the high pO_2 side. Figure 11 schematically demonstrates the direction of fluxes and the shift of the LNO membrane after exposure to the oxygen potential gradient.

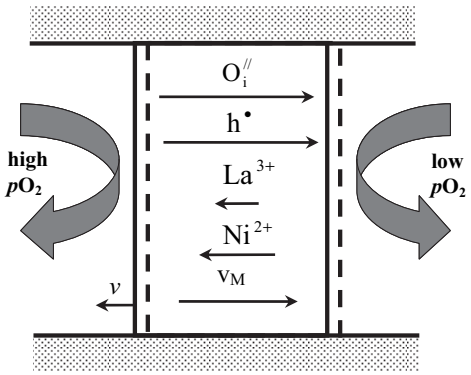

Figure 11. Fluxes of cations, $La^{3+}$and Ni^{2+}, cation vacancies v_M, oxygen interstitials, $O_i^{//}$, electron holes, $h^{\bullet}$, and shift *v* of the crystal surface when exposed to an oxygen potential gradient.

By applying the thermodynamics of kinetic decomposition developed by Schmalzried *et al.*,[24] the mathematical expression of decomposition with respect to temperature, diffusivities of cations, and thermodynamic parameters can be derived for the LNO system, and consequently the critical oxygen potential differences to initialise the decomposition at certain temperature can be calculated.

The mathematical models for kinetic decomposition were mainly developed for and applied to systems where the oxygen lattice is regarded as immobile,[21,31] i.e., oxide ions are slower than the cations. However, the treatment also applies to, and has been applied to oxides[32] in which the oxide ions are faster than the cations, and we do the same here.

The driving forces governing the motion of cations are the gradients of their electrochemical potentials, $\eta_i = \mu_i + z_i F\varphi$, where μ_i is the chemical potential, z_i the charge number, F Faraday's constant, and φ the electric potential. The fluxes for cations (Ni^{2+} and La^{3+}) in LNO are

$$j_{Ni^{2+}} = -\frac{c_{Ni} D_{Ni}}{RT} \nabla\left(\mu_{Ni^{2+}} + 2F\varphi\right) \quad \textbf{1}$$

$$j_{La^{3+}} = -\frac{c_{La} D_{La}}{RT} \nabla\left(\mu_{La^{3+}} + 3F\varphi\right) \quad \textbf{2}$$

where c and D are the concentration and diffusivity of cations, respectively, and other terms have their usual meanings. By assuming the local thermodynamic equilibrium, the

chemical potential of cations can be written in terms of the chemical potential of neutral chemical entities and electrons,[21,24] leading to

$$j_{\mathrm{Ni}^{2+}} = -\frac{c_{\mathrm{Ni}} D_{\mathrm{Ni}}}{RT}\left(\nabla\mu_{\mathrm{NiO}} - \frac{1}{2}\nabla\mu_{\mathrm{O}_2}\right) \quad \textbf{3}$$

$$j_{\mathrm{La}^{3+}} = -\frac{c_{\mathrm{La}} D_{\mathrm{La}}}{RT}\left(\frac{1}{2}\nabla\mu_{\mathrm{La_2O_3}} - \frac{3}{4}\nabla\mu_{\mathrm{O}_2}\right) \quad \textbf{4}$$

When steady state is achieved, the two cations will move at the same velocity v_s, i.e.:

$$v_s = j_{\mathrm{Ni}^{2+}} / c_{\mathrm{Ni}} = j_{\mathrm{La}^{3+}} / c_{\mathrm{La}} \quad \textbf{5}$$

Based on this condition, Eqs. 3 and 4 can be related and simplified as

$$D_{\mathrm{Ni}}\nabla\mu_{\mathrm{NiO}} = \left(\frac{1}{2}D_{\mathrm{Ni}} - \frac{3}{4}D_{\mathrm{La}}\right)\nabla\mu_{\mathrm{O}_2} + \frac{1}{2}D_{\mathrm{La}}\nabla\mu_{\mathrm{La_2O_3}} \quad \textbf{6}$$

According to the Gibbs-Duhem relation for the binary NiO-La_2O_3 system, the chemical potential gradients of NiO and La_2O_3 are related through

$$\nabla\mu_{\mathrm{NiO}} = -\nabla\mu_{\mathrm{La_2O_3}} \quad \textbf{7}$$

With this relation and through integration, Eq. 6 can be transformed to

$$\Delta\mu_{\mathrm{NiO}} = \frac{1 - \frac{3}{2}\frac{D_{\mathrm{La}}}{D_{\mathrm{Ni}}}}{2 + \frac{D_{\mathrm{La}}}{D_{\mathrm{Ni}}}}\Delta\mu_{\mathrm{O}_2} \quad \textbf{8}$$

The maximum (or critical) $\Delta\mu_{\mathrm{NiO}}$ that the LNO can withstand without decomposing into its corresponding binary oxides, can be estimated as

$$\Delta\mu_{\mathrm{NiO}}{}^{\max} = -\Delta G_T^{\circ}(\mathrm{LNO}) \quad \textbf{9}$$

where $\Delta G_T°(\mathrm{LNO})$ is the standard Gibbs free energy change at the experimental temperature (T) for the reaction $\mathrm{NiO(s) + La_2O_3(s) = La_2NiO_4(s)}$.[33] Inserting Eq. 9 into Eq. 8 and introducing oxygen partial pressures, we obtain

$$\ln\left(\frac{p\mathrm{O}_2^{//}}{p\mathrm{O}_2^{/}}\right)^{\mathrm{critical}} = -\frac{2+\frac{D_{\mathrm{La}}}{D_{\mathrm{Ni}}}}{1-\frac{3}{2}\frac{D_{\mathrm{La}}}{D_{\mathrm{Ni}}}} \times \frac{\Delta G_T°(\mathrm{LNO})}{RT} \qquad \textbf{10}$$

where $p\mathrm{O}_2^{//}$ and $p\mathrm{O}_2^{/}$ represent the high and low $p\mathrm{O}_2$, respectively.

As can be seen from the above equation, the critical ratio of the oxygen partial pressures that the LNO membrane can withstand without decomposition depends on both thermodynamic and kinetic parameters (diffusivities of cations). A graphical representation of Eq. 10 at 1000 °C is plotted in Figure 12 as a function of the ratio of $D_{\mathrm{La}}/D_{\mathrm{Ni}}$. Figure 12 clearly shows that the smaller the ratio of $D_{\mathrm{La}}/D_{\mathrm{Ni}}$ is (Ni more mobile than La), the smaller the oxygen partial pressure difference is needed to kinetically initialise the decomposition of the LNO membrane. In the case of $D_{\mathrm{La}}/D_{\mathrm{Ni}} = 2/3$, a decomposition due to the kinetic reasons is not possible however large the oxygen potential difference applied to the LNO membrane is. Since NiO was found on the high $p\mathrm{O}_2$ side (cf. Figure 3), we must have $D_{\mathrm{La}}/D_{\mathrm{Ni}} < 2/3$ in the LNO system.

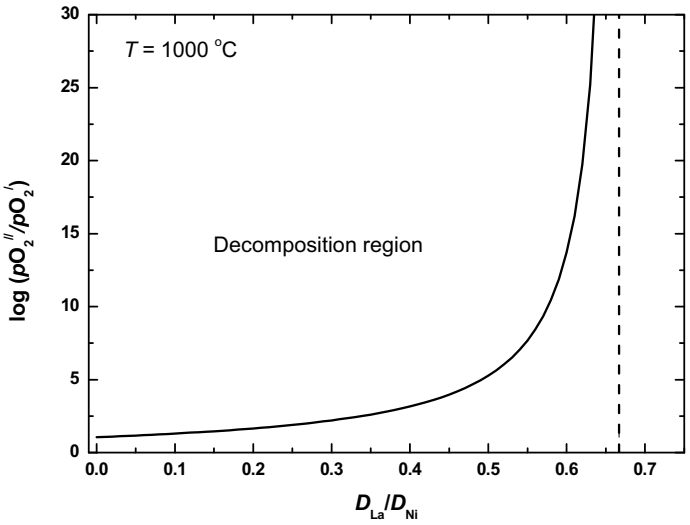

Figure 12. Critical log ($pO_2^{//}/pO_2^{/}$) versus D_{La}/D_{Ni} at 1000 °C. The dashed line stands for the theoretical limit ratio, where kinetic decomposition is impossible in the LNO system.

In the present investigation, pure oxygen and argon were used to create the oxygen potential gradient along the LNO membrane, and thus log ($pO_2^{//}/pO_2^{/}$) can be approximated as 5. Without taking into account the surface exchange that leads to a drop in the oxygen potential, the ratio of D_{La}/D_{Ni} should be smaller than 0.5 to initialise the decomposition according to Figure 12. This can be partly verified by our previous solid state reaction between NiO and La_2O_3,[26] in which Ni was determined to be the fastest moving cation in LNO. However, the SSR can only give the diffusivity of the fastest cation, and D_{La} and detailed diffusion mechanisms can not be obtained through such a technique. Considering the high diffusivity of Ni in ceramic LNO as compared to those of other perovskite-related oxides,[26] it is surprising that no continuous NiO layer was formed on the high pO_2 side after such long-term annealing; instead small particles of NiO were spread over the surface. This indicates that the difference in mobility between Ni and La at 1000 °C may not be very big. Similar behaviour was also observed in $BaTiO_3$ due to comparable diffusivities between two cations.[32] Meanwhile, we have not found any La_2O_3 on the low pO_2 side (cf. Figure 4), which is contradictory to the mass conservative law. To find more detailed information regarding cation diffusion in the LNO system, impurity Pr, Nd and Co

tracers have been selected to study transport properties on La- and Ni- sites, respectively.[27] The obtained results have revealed that both sites have comparable diffusivities, while Ni-site is a little bit faster due to the enhancement by the grain boundary diffusion as compared to La-site which is dominated by the bulk diffusion. Similar behaviour was also observed from inter-diffusion measurements.[28] Since Ni mainly diffuses through the fast diffusion path along grain boundaries, the decomposition of the LNO takes place by taking NiO from the grain boundaries at the low pO_2 side, eating LNO from pores growing along those grain boundaries, and leaving La_2O_3 along grain boundaries and in the pores, not detectable by the present experimental techniques. This will have a great influence on the distribution of oxygen potential as will be discussed below.

Based on the above analyses, the imposed oxygen potential gradient over the LNO membrane in the present investigation appears to be higher than its critical value – causing decomposition of the LNO membrane. The decomposition products – NiO and La_2O_3 – may take up some of the imposed $\Delta\mu_{O_2}$ so that the gradient over the LNO decreases, and a steady state is reached where it stops decomposing. We believe it may be the La_2O_3 because it may have formed a thin blocking layer on the low pO_2 side inside the pores, while the NiO is not a dense layer. The blocking effect of the La_2O_3 layer is in accord with the oxygen fluxes decreasing initially, then stabilizing (as shown in Figure 13) because the layer stops growing after a while when steady state is achieved.

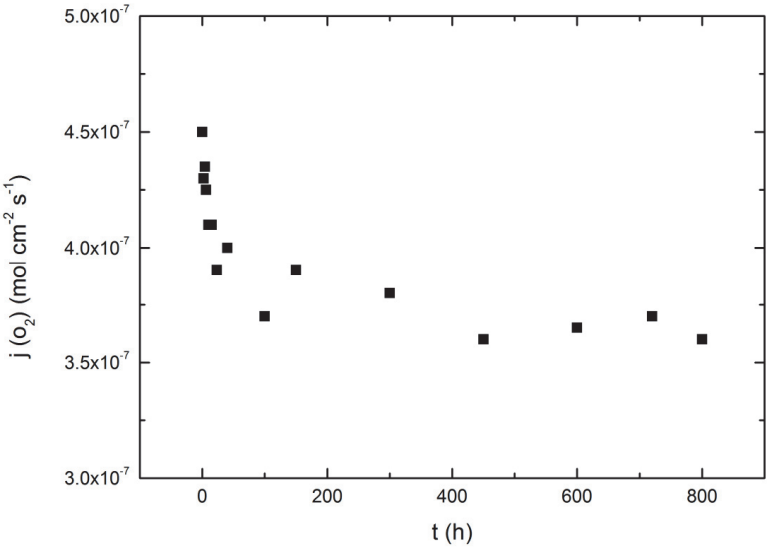

Figure 13. Oxygen flux of the LNO membrane versus time when exposed to an oxygen gradient between O_2 and Ar at 1000 °C.

At this point one may ask whether NiO and La_2O_3 are the expected sole products of decomposition. There are a few recent reports about long-term stability of LNO, revealing a decomposition into higher-order RP phases with higher Ni oxidation states, notably $La_3Ni_2O_{7-\delta}$ and $La_4Ni_3O_{10-\delta}$, at moderate temperatures and high pO_2.[30,34-36] Moreover, the stability of RP phases decreases in the order: LNO > $La_3Ni_2O_7$ > $La_4Ni_3O_{10}$ > $LaNiO_3$, with increasing temperature.[34,35,37,38] In accord with this, our work in the present investigation at relatively high temperatures did not lead to detection of any other phases than LNO.

The bubble-like pores observed close to the low pO_2 side (see Figure 14) are partly due to the removal of Ni during the decomposition stage and partly due to the shift of the bulk LNO towards the high pO_2 side under the steady state. The bulk movement of the LNO membrane occurs by the diffusion of Ni and La away from the low pO_2 side and simultaneous release of oxygen to the gas phase. The porosity on the low pO_2 side can cause a great challenge to the stability of LNO in real applications because of the short

diffusion length, large gradient, and fast migration of cations from pore tips, which may penetrate the membrane.

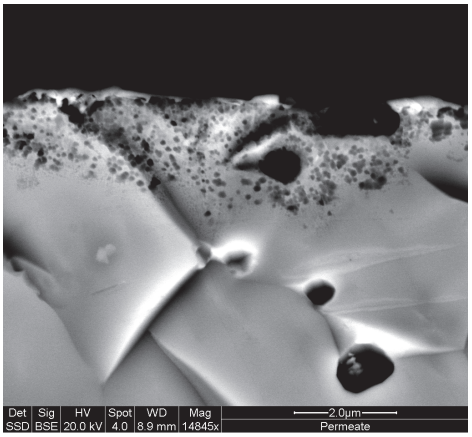

Figure 14. SEM micrograph of the fracture surface of the low pO_2 side, showing the formation of bubble-like porosity in the immediate vicinity of the surface.

Furthermore, to the best of our knowledge, only very limited experimental results have been reported on kinetic demixing or decomposition of oxygen separation membranes. Lein *et al*.[39] annealed $La_{0.5}Sr_{0.5}Fe_{0.5}Co_{0.5}O_{3-\delta}$ (LSFC) in an O_2/N_2 gradient at 1150 °C for one month. They found similar result as ours: CoO was precipitated on the primary side (high pO_2); No phase separation was found on the secondary side (low pO_2); The oxygen flux was almost unchanged with time after the decrease at the initial stage of annealing, but no explanation was given. Moreover, kinetic demixing was also observed in the shallow region near the surfaces due to doping on both sites. In the case of $La_{0.3}Sr_{0.7}CoO_{3-\delta}$,[40] only SrO was observed on the surface of oxygen lean-side (low pO_2), and no oxygen flux variation was noticed during the annealing, which was attributed to the highly porous nature of the SrO layer. It is surprising that the phase separation in all these cases was found either on the high pO_2 side or the low pO_2 side rather than on both sides, indicating that a secondary phase may be segregated along grain boundaries or inside pores as suggested in the present investigation.

5. Conclusions

In this work we investigated effects of exposure of the LNO membrane to an oxygen gradient (1 atm O_2 versus Ar) for 800 h at 1000 °C. On the high pO_2 side we observed formation of NiO, while on the low pO_2 side pores were created, but without detectable formation of La_2O_3 or other change in composition. The undetected La_2O_3 was suggested to remain along the grain boundaries to form a layer offsetting the oxygen gradient, which is in good agreement with the stable, lower oxygen flux after an initial decrease. Based on the derived critical $\Delta\mu_{O_2}$, it was concluded that the ratio of D_{La}/D_{Ni} should be slightly smaller than 0.5 to initialise the decomposition of the LNO membrane under the present experimental window. The decomposition products on either side will eventually retard the kinetic decomposition, and only steady state "walk-out" will remain. Both this and the decomposition constitute serious threats to the stability of thin LNO membranes in practical operations for oxygen separation.

6. Acknowledgements

We are grateful for support under the projects *Kinetics of High-Temperature Oxide Ion and Proton Conductors* (*KINOXPRO*) (*RENERGI 190901/S60)* from the Research Council of Norway (RCN) and *Demonstration of AZEP Reactor Module (162316)* from RCN and Statoil. We are grateful to Muriel M. L. Erambert at Dept. Geosciences, University of Oslo (UiO) for EPMA and Martin F. Sunding of Dept. Physics, UiO, for XPS.

7. References:

1. E. N. Naumovich, M. V. Patrakeev, V. V. Kharton, A. A. Yaremchenko, D. I. Logvinovich and F. M. B. Marques, *Solid State Sci.*, **7**, 1353-1362 (2005).

2. V. V. Kharton, A. P. Viskup, A. V. Kovalevsky, E. N. Naumovich and F. M. B. Marques, *Solid State Ionics*, **143**, 337-353 (2001).

3. V. V. Vashook, I. I. Yushkevich, L. V. Kokhanovsky, L. V. Makhnach, S. P. Tolochko, I. F. Kononyuk, H. Ullmann and H. Altenburg, *Solid State Ionics*, **119**, 23-30 (1999).

4. V. V. Kharton, A. P. Viskup, E. N. Naumovich and F. M. B. Marques, *J. Mater. Chem.*, **9**, 2623-2629 (1999).

5. Z. Li, R. Haugsrud, J. B. Smith and T. Norby, *Solid State Ionics*, **180**, 1433-1441 (2009).

6. Z. Li, R. Haugsrud, J. B. Smith and T. Norby, *J. Electrochem. Soc.*, **159**(9), B1039-B1044 (2009).

7. S. J. Skinner and J. A. Kilner, *Solid State Ionics*, **135**, 709-712 (2000).

8. V. V. Vashook, S. P. Tolochko, I. I. Yushkevich, L. V. Makhnach, I. F. Kononyuk, H. Altenburg, J. Hauck and H. Ullmann, *Solid State Ionics*, **110**, 245-253 (1998).

9. C. N. Munnings, S. J. Skinner, G. Amow, P. S. Whitfield and I. J. Davidson, *Solid State Ionics*, **176**, 1895-1901 (2005).

10. F. Mauvy, E. Boehm, J. M. Bassat, J. C. Grenier and J. Fouletier, *Solid State Ionics*, **178**, 1200-1204 (2007).

11. E. Boehm, J. M. Bassat, M .C. Steil, P. Dordor, F. Mauvy and J. C. Grenier, *Solid State Sci.*, **5**, 973-981 (2003).

12. J. B. Goodenough and S. Ramasesha, *Mater. Res. Bull.*, Vol. **17**, 383-390 (1982).

13. S. J. Skinner, *Solid State Sci.*, **5**, 419-426 (2003).

14. A. Aguadero, M. Pérez, J. A. Alonso and L. Daza, *J. Power Sources*, **151**, 52-56 (2005).

15. H. Ishikawa, Y. Toyosumi and K. Ishikawa, *J. Alloys Compd.*, **408-412**, 1196-1199 (2006).

16. W. Paulus, A. Cousson, G. Dhalenne, J. Berthon, A. Revcolevschi, S. Hosoya, W. Treutmann, G. Heger and R. Le Toquin, *Solid State Sci.*, **4**, 565-573 (2002).

17. J. D. Jorgensen, B. Dabrowski, S. Pei, D. R. Richards and D. G. Hinks, *Phys. Rev. B*, Vol. **40**, 2187-2199 (1989).

18. M. Schroeder and M. -A. Dragan, *J. Mater. Sci.*, **42**, 1972-1983 (2007).

19. J. B. Smith and T. Norby, *J. Electrochem. Soc.*, **153**, A233-A238 (2006).

20. M. S. D. Read, M. S. Islam, F. King and F. E. Hancock, *J. Phys. Chem. B*, **103**, 1558-1562 (1999).

21. M. Martin, *J. Chem. Thermodyn.*, **35**, 1291-1308 (2003).

22. J. Wolfenstine, *Solid State Ionics*, **126**, 293-298 (1999).

23. R. De Souza, S. M. Islam and E. Ivers-Tiffee, *Fortschr. Deutsch. Keram. Ges.*, **15**, 305-317 (2000).

24. H. Schmalzried and W. Laqua, *Oxid. Met.*, **15**, 339-353 (1981).

25. K. T. Jacob, A. K. Shukla, *J. Mater. Res.*, **2**, 338-344 (1987).

26. N. Čebašek, R. Haugsrud, Z. Li, J. Milošević, J. B. Smith, A. Magrasó and T. Norby, *J. Electrochem. Soc.*, **159** (6), B702-B708 (2012).

27. N. Čebašek, R. Haugsrud, Z. Li, J. B. Smith and T. Norby, *to be submitted.*

28. N. Čebašek, R. Haugsrud, T. Norby, *submitted in Solid State Ionics*.

29. International Organization for Standardization. ISO 15472:2001(E) "*Surface chemical analysis – X-ray photoelectron spectrometers – Calibration of energy scales*", *International Organization for Standardization*, Geneva, 2001.

30. R. Sayers and S. J. Skinner, *J. Mater. Chem.*, **21**, 414-419 (2011).

31. H. Schmalzried, *Chemical Kinetics of Solids, Solid State Reactions*, Chapter 8, Verlag Chemie, Weinheim/Bergstr., 1974.

32. H. -I. Yoo, C. -E. Lee, R. A. De Souza and M. Martin, *Appl. Phys. Lett.*, **92**, 252103 (2008).

33. O. M. Sreedharan, M. S. Chandrasekharaiah and M. D. Karkhanavala, *High Temp. Sci.*, **8**, 179-183 (1976).

34. M. Zinkevich, N. Solak. H. Nitsche, M. Ahrens and F. Aldinger, *J. Alloys Compd.*, **438**, 92-99 (2007).

35. N. Gauquelin, T. E. Weirich, M. Ceretti, W. Paulus and M. Schroeder, *Monatsh. Chem.*, **140**, 1095-1102 (2009).

36. G. Amow, I. J. Davidson and S. J. Skinner, *Solid State Ionics*, **177**, 1205-1210 (2006).

37. M. Zinkevich and F. Aldinger, *J. Alloys Compd.*, **375**, 147-161 (2004).

38. M. Greenblatt, *Curr. Opin. Solid State Mater. Sci.*, **2**, 174-183 (1997).

39. H.L. Lein, K. Wiik and T. Grande, *Solid State Ionics*, **177**, 1587-1590 (2006).

40. R. H. E. van Doorn, H. J. M. Bouwmeester and A. J. Burggraaf, *Solid State Ionics*, **111**, 263-272 (1998).

6. Summary of results and unanswered questions

In this Chapter, I will summarise the findings from this first comprehensive study of cation diffusion in LNO. I will start with properties and interpretations that can be evaluated with reasonable safety. Then I move to more ambiguous data and interpretations and finally the remaining questions under discussion.

- According to the experimental work and the discussions of the results in included papers it can be essentially summarised that: The A-site cation diffusion proceeds mainly through the bulk.
- The B-site cation has diffusion enhanced along grain boundaries – typically by 5 orders of magnitude.
- The B-site cation is thus the fastest moving cation in polycrystalline LNO, with effective diffusion coefficients typically one to two orders of magnitude above A-site cation diffusion.
- LNO-based materials exhibit relatively fast cation diffusion as compared with other perovskite-related materials.

The quantitative results on the cation diffusion coefficients obtained by fitting experimental data are as follows:

- Chemical (impurity) tracer diffusion coefficients into LNO (from two sets of measurements) are:
  - $D_{\mathrm{Pr}}^{\mathrm{1st}}(\mathrm{cm}^2/\mathrm{s}) = 10^{-5.6\pm0.6}\exp(-\frac{178\pm17\mathrm{kJ/mol}}{RT})$

- $D_{Pr}^{2nd}(cm^2/s) = 10^{-6.3\pm0.4}\exp(-\frac{147\pm15kJ/mol}{RT})$
- $D_{Nd}(cm^2/s) = 10^{-5.7\pm0.4}\exp(-\frac{167\pm13kJ/mol}{RT})$
- $D_{Co_B}^{1st}(cm^2/s) = 10^{-1.5\pm0.9}\exp(-\frac{299\pm24kJ/mol}{RT})$
- $D_{Co_B}^{2nd}(cm^2/s) = 10^{-1.7\pm0.4}\exp(-\frac{290\pm12kJ/mol}{RT})$
- $D_{Co_{GB}}^{1st}(cm^2/s) = 10^{6.4\pm0.4}\exp(-\frac{402\pm10kJ/mol}{RT})$
- $D_{Co_{GB}}^{2nd}(cm^2/s) = 10^{4.9\pm0.4}\exp(-\frac{360\pm23kJ/mol}{RT})$

- The average apparent activation energies for Pr and Nd bulk diffusion are 165±15 kJ/mol, for Co bulk diffusion 295±15 kJ/mol, and for Co grain boundary diffusion 380±20 kJ/mol.
- Inter-diffusion coefficients between LNO/$La_2CuO_{4+\delta}$ and LNO/$Nd_2NiO_{4+\delta}$ diffusion couples are :
  - $D_{La/Nd}(cm^2/s) = 10^{-2.1\pm0.4}\exp(-\frac{275\pm12kJ/mol}{RT})$
  - $D_{Ni/Cu_B}(cm^2/s) = 10^{4.5\pm0.6}\exp(-\frac{450\pm20kJ/mol}{RT})$
  - $D_{Ni/Cu_{GB}}(cm^2/s) = 10^{-1.5\pm0.8}\exp(-\frac{135\pm20kJ/mol}{RT})$

Fig. 6.1 presents the abovementioned diffusion coefficients.

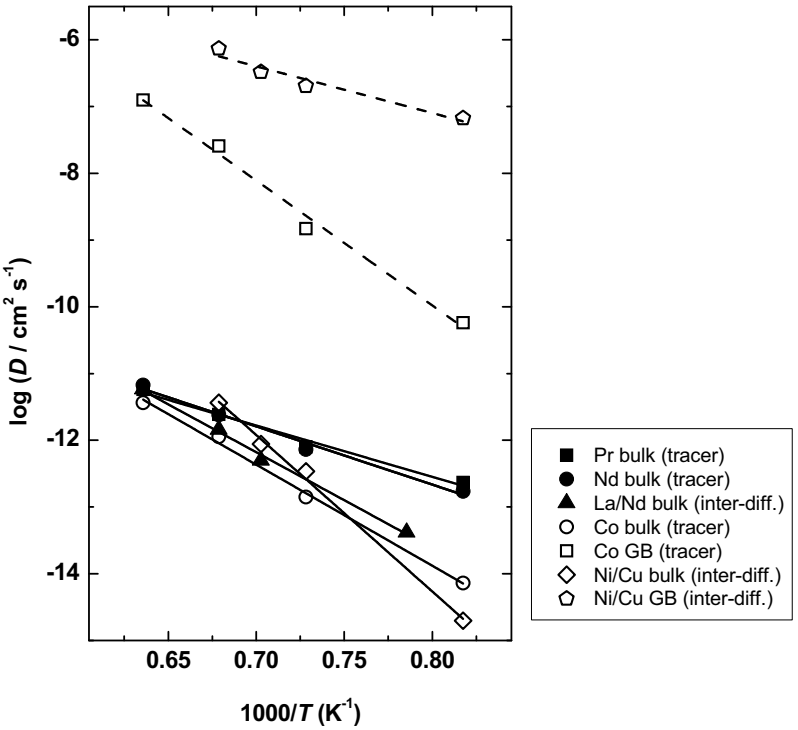

Figure 6.1. Comparison between the diffusion coefficients for the A- and B-site cations in LNO, obtained by the chemical tracer diffusion and inter-diffusion techniques.

We first notice that bulk diffusivities of A- and B-site cations are quite similar. However, B-site bulk diffusion seems to have higher activation energies, compensated by higher pre-exponentials. This may reflect statistical uncertainty in the measurements, a correlation in the attempt jump frequency, and different defect chemistries. A reason for such difference, as we suggested in the papers, is that the concentration of A-site vacancies is frozen in from the high sintering temperature, while the concentration of B-site vacancies to a larger extent equilibrates through short-circuit paths, e.g. grain boundaries or dislocations. According to this hypothesis, the activation energy for diffusion of A-site cation would comprise only the enthalpy of migration, while the activation energy for B-site diffusion would comprise enthalpies for both creation and migration of defects. As the equilibration of defects (vacancies) requires creation (or annihilation) of new unit cells, the presence of secondary phase or segregation along grain boundaries would be expected.

To continue with grain boundaries issue; from the plot (cf. Figure 6.1) we observe that grain boundary diffusion for B-site cations is ~5 orders of magnitude higher than bulk. The higher grain boundary diffusivity of Ni/Cu compared to that of Co tracer is left largely unexplained at this stage. However, we will later on briefly report that preliminary results indicate that Cu substitution of LNO increases cation diffusion, so that this may have an influence also on grain boundary diffusion in Ni/Cu solid solution. Nevertheless, the activation energies for grain boundary diffusion in Ni/Cu inter-diffusion couples and Co impurity tracer appear to be similar to or higher than for B-site bulk diffusion.

Overall, the influence of the grain boundary diffusion on B-site cation is evident if we calculate effective diffusion coefficients and compare it with the A-site bulk diffusion; such calculated B-site apparent diffusivity is always higher than the A-site bulk in the experimental temperature range, and its activation energy is dominated by the grain boundary activation energy, as presented in the Papers.

Now let us move to the solid state reaction (SSR) results. The calculated apparent self-diffusion coefficients of the Ni^{2+} ions are presented as the interval between two extreme cases, determined by the activity of reactant La_2O_3, at the two interfaces between reaction layer and reactants, and can be expressed as

- $$D_{\mathrm{Ni}^{2+}}(\mathrm{cm}^2/\mathrm{s}) = k_{\mathrm{p}}\left(1-\exp\left(\frac{\Delta G_T^{\circ}}{RT}\right)\right)^{-1} a_{\mathrm{La_2O_3}}$$

where $a_{\mathrm{La_2O_3}}$ may have value 1 and $\exp(\Delta G_T^{\circ}/RT)$ at the La_2O_3/LNO and NiO/LNO interfaces, respectively. It is important to repeat the fact from the Paper III that in the SSR experiment it is not possible to separate bulk and grain boundary diffusion. However, based on the above knowledge we now have about B-site diffusion, we may conclude that the apparent self-diffusion of the Ni^{2+} ions for a large part reflects grain boundary diffusion. Figure 6.2 compares bulk diffusion coefficients of A- and B-site cations from chemical tracer and inter-diffusion experiment with the apparent Ni^{2+} self-diffusion coefficient from the SSR study. As expected the diffusion coefficient from the SSR is higher than the majority of the others, but not very much. We attribute the modest difference to relatively large grains and hence few grain boundaries in the LNO layers grown in the SSR experiments.

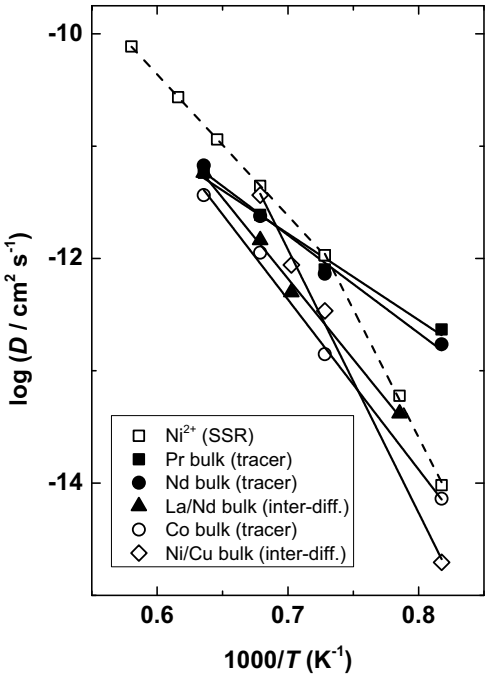

Figure 6.2. Comparison of the bulk diffusion coefficients for the A- and B-site cations in LNO, obtained by the chemical tracer diffusion and inter-diffusion techniques with the apparent self-diffusion coefficient of Ni^{2+} from the SSR study.

To verify the results obtained from chemical tracer, inter-diffusion and SSR, we exposed a LNO membrane to a gradient of pO_2 at high temperatures. After long-term annealing, we observed decomposition, i.e., precipitation of a Ni rich phase (NiO) on the high pO_2 side of membrane. This confirmed our finding that the effectively fastest moving cation in polycrystalline LNO is Ni^{2+}. Moreover, the absence of a continuous blocking layer and instead a randomly spread NiO phase at the high pO_2 side show that segregation of secondary phase may have occurred where the grain boundaries were intercepted by the surface. This indirectly confirmed, once again, the conclusion on dominant fast grain boundary diffusion of the B-site cation.

After the above conclusions, there are still some open questions that need further attention. One of those issues is the non-Arrhenius downward bending of the temperature

dependency of the Ni^{2+} self-diffusion coefficient at the low experimental temperature regime. Several options were suggested in Paper III and our primary explanation is that the concentration of Ni vacancies exhibits a temperature dependency in this lower temperature range, i.e., concentration of Ni vacancies reaches equilibrium, as in the growing LNO reaction layer oxygen diffusion has a lower activation energy for diffusion to establish non-stoichiometry than cation diffusion to grow the layer. At the higher experimental temperature range Ni vacancies are not in equilibrium with the surrounding atmosphere because the layer now grows fast compared to the oxygen diffusion, which is confirmed by the pO_2 independency of the reaction layer growth at 1350 °C.

The next issue is the higher activation energy for grain boundary diffusion than that of bulk for B-site cations in the chemical tracer experiment. In the literature there are very few data the shed light on this phenomenon. Possible explanations comprise temperature dependent change of oxidation state of the chemical tracer (Co) and segregation of secondary phase along grain boundaries.

The chemical tracer experiment has one more peculiarity; the pO_2 dependency of B-site cation diffusion in LNO is opposite than expected for diffusion by cation vacancies. In Paper II we proposed explanations for this phenomenon: interstitial diffusion mechanism, complex mechanism of diffusion involving more than one defect, change in oxidation state of the diffusant (impurity tracer) or steric effect due to change in LNO oxygen stoichiometry. However, this issue requires further investigation beyond the scope of the possibilities of the present Thesis project.

By comparing the obtained results from this work with cation diffusion of perovskites from literature, it is evident that cation diffusion in LNO exhibits relatively high values. Such high diffusivities and walk-out caused by steady state diffusion of cations will create severe problems for the technological applications of the LNO membranes for oxygen separation.

In order to stabilise the LNO structure for use in oxygen permeation membranes, some experiments have been performed with Sr and Cu doped LNO. These experiments are still under way, but it seems from preliminary analyses that doping in fact increases the diffusivities of both A- and B-site cations and thus may worsen the degradation from kinetic decomposition.

7. Conclusions and outlook

The research work described in this thesis has investigated diffusion of cations and related degradation phenomena in $La_2NiO_{4+\delta}$ (LNO) as oxygen separation membrane. Experimental methods used in this research were solid state reaction, chemical (impurity) tracer and inter-diffusion technique, including decomposition of LNO membrane under a gradient of pO_2.

The obtained results showed that A- and B-site cation diffusion in bulk are of equal magnitude, and B-site exhibits enhanced diffusion along grain boundaries at temperatures between 950 and 1450 °C in air atmosphere. The cation diffusivities in LNO are among the higher for cations in perovskite-related materials reported so far. In order to reduce the oxygen non-stoichiometry, defect ordering, and phase instability, LNO was doped on A- and B-site with Sr and Cu, respectively. It was of hope that this would not increase cation diffusivity. Since cation diffusivity was not previously investigated, this study thus started with the undoped material. Preliminary results on the Sr and Cu doping showed increase of the diffusivities of A- and B-site cations, but with similar activation energies to those of the undoped LNO.

The experiment on degradation of LNO membrane showed that decomposition will eventually stop at certain point due to the establishment of steady state diffusion of cations. Due to high diffusivities of La and Ni under the pO_2 gradient, membrane walk-out is still inevitable, creating serious threats to the stability of thin LNO membranes in practical operations for oxygen separation.

As the nominally pure LNO oxygen separation membrane exhibits the highest oxygen permeation and as our preliminary results with doped LNO show that the dopants actually enhance cation diffusion, it can be suggested that LNO should be used in technological

applications as nominally unsubstituted. The lifetime of the LNO oxygen separation membrane will largely depend on the applied gradient in oxygen potential, so another suggestion for technological application in order to increase its lifetime would be the application of nominally pure LNO in relatively small oxygen potential gradients at the lowest possible temperatures that still facilitate acceptable oxygen separation.

8. Appendices

Appendix I. Derivation for the expression of the concentration of majority and minority defects in $La_2NiO_{4+\delta}$

As the oxygen interstitials and electron holes are major defects in $La_2NiO_{4+\delta}$ (LNO), two major defect reactions (the anti-Frenkel and the reaction of oxygen intercalation, i.e., oxidation) can be taken as the starting point for the further derivation of defect concentration

$$O_O^x = v_o^{\bullet\bullet} + O_i^{//} \quad \textbf{8.1}$$

$$\frac{1}{2}O_{2(g)} = O_i^{//} + 2h^{\bullet} \quad \textbf{8.2}$$

Following the law of mass action, we can write the corresponding equilibrium constants for Eqs. 8.1 and 8.2

$$K_{AF} = [v_O^{\bullet\bullet}][O_i^{//}] \quad \textbf{8.3}$$

$$K_{Ox} = [O_i^{//}]p^2 pO_2^{-1/2} \quad \textbf{8.4}$$

From Eqs. 8.3 and 8.4 and the electroneutrality condition in Eq. 8.5 (below)

$$2[O_i^{//}] = p \quad \textbf{8.5}$$

we can write the following expressions for the concentration of oxygen interstitials, electron holes and oxygen vacancies

$$[O_i^{//}] = (\frac{1}{4})^{1/3} K_{Ox}^{1/3} pO_2^{1/6} \quad \textbf{8.6}$$

$$p = 2^{1/3} K_{Ox}^{1/3} pO_2^{1/6} \quad \textbf{8.7}$$

$$[v_O^{\bullet\bullet}] = (\frac{1}{4})^{-1/3} K_{AF} K_{Ox}^{-1/3} pO_2^{-1/6} \quad \textbf{8.8}$$

If we assume that the creation of the minority defect, i.e., the cation vacancies occurs through the Schottky disorder, we can write

$$0 = v_{Ni}^{//} + 2v_{La}^{///} + 4v_O^{\bullet\bullet} \quad \textbf{8.9}$$

and the corresponding equilibrium constant is

$$K_S = [v_{Ni}^{//}]\left[\frac{[v_{La}^{///}]}{2}\right]^2 \left[\frac{[v_O^{\bullet\bullet}]}{4}\right]^4 \quad \textbf{8.10}$$

If we now assume that for the creation of every Ni vacancy, two La vacancies are created, Eq. 8.11 (below)

$$\frac{1}{2}[v_{Ni}^{//}] = [v_{La}^{///}] \quad \textbf{8.11}$$

the equilibrium constant for the Schottky disorder if we are calculating the Ni vacancies can be written as

$$K_S = \frac{[v_{Ni}^{//}]^3 [v_O^{\bullet\bullet}]^4}{2^4 4^4} \quad \textbf{8.12}$$

and from this Eq. 8.12, the concentration of Ni vacancies can be written as

$$[v_{Ni}^{//}] = 2^4 K_S^{1/3} [v_O^{\bullet\bullet}]^{-4/3} \quad \textbf{8.13}$$

If we derive the expression for the La vacancies from Eqs. 8.11 and 8.12 we can write

$$[v_{La}^{///}] = 2^{1/3} 4^{4/3} K_S^{1/3} [v_O^{\bullet\bullet}]^{-4/3} \quad \textbf{8.14}$$

And, finally, if we substitute Eq. 8.8 for the concentration of oxygen vacancies into Eqs. 8.13 and 8.14, the expressions for the concentration of Ni and La vacancies are as follows

$$[\mathrm{v}_{\mathrm{Ni}}^{//}] = 2^4 (\frac{1}{4})^{4/9} K_{\mathrm{S}}{}^{1/3} K_{\mathrm{AF}}{}^{-4/3} K_{\mathrm{Ox}}{}^{4/9} p\mathrm{O}_2{}^{2/9} \quad \textbf{8.15}$$

$$[\mathrm{v}_{\mathrm{La}}^{///}] = 2^{1/3} 4^{4/3} (\frac{1}{4})^{4/9} K_{\mathrm{S}}{}^{1/3} K_{\mathrm{AF}}{}^{-4/3} K_{\mathrm{Ox}}{}^{4/9} p\mathrm{O}_2{}^{2/9} \quad \textbf{8.16}$$

We know from thermodynamics that the equilibrium constant can be written as

$$K = \exp(\frac{\Delta S^\circ}{\mathrm{R}}) \exp(-\frac{\Delta H^\circ}{\mathrm{R}T}) \quad \textbf{8.17}$$

where ΔS° and ΔH° represent the standard entropy and enthalpy, for the corresponding defect reaction (anti-Frenkel, oxidation and the Schottky disorder). If we now substitute Eq. 8.17 into Eqs. 8.6, 8.7, 8.8, 8.15 and 8.16, we can express the concentration of oxygen interstitials, electron holes and vacancies of oxygen, Ni and La as follows

$$[\mathrm{O}_{\mathrm{i}}^{//}] = (\frac{1}{4})^{1/3} p\mathrm{O}_2{}^{1/6} \exp(\frac{\Delta S_{\mathrm{Ox}}{}^\circ}{3R}) \exp(-\frac{\Delta H_{\mathrm{Ox}}{}^\circ}{3RT}) \quad \textbf{8.18}$$

$$\mathrm{p} = 2^{1/3} p\mathrm{O}_2{}^{1/6} \exp(\frac{\Delta S_{\mathrm{Ox}}{}^\circ}{3R}) \exp(-\frac{\Delta H_{\mathrm{Ox}}{}^\circ}{3RT}) \quad \textbf{8.19}$$

$$[\mathrm{v}_{\mathrm{O}}^{//}] = (\frac{1}{4})^{-1/3} p\mathrm{O}_2{}^{-1/6} \exp(\frac{\Delta S_{\mathrm{AF}}{}^\circ}{R} - \frac{\Delta S_{\mathrm{Ox}}{}^\circ}{3R}) \exp(-\frac{\Delta H_{\mathrm{AF}}{}^\circ}{RT} + \frac{\Delta H_{\mathrm{Ox}}{}^\circ}{3RT}) \quad \textbf{8.20}$$

$$[\mathrm{v}_{\mathrm{Ni}}^{//}] = 16^{7/9} p\mathrm{O}_2{}^{2/9} \exp(\frac{\Delta S_{\mathrm{S}}{}^\circ}{3R} - \frac{4\Delta S_{\mathrm{AF}}{}^\circ}{3R} + \frac{4\Delta S_{\mathrm{Ox}}{}^\circ}{9R}) \exp(-(\frac{\Delta H_{\mathrm{S}}{}^\circ}{3RT} - \frac{4\Delta H_{\mathrm{AF}}{}^\circ}{3RT} + \frac{4\Delta H_{\mathrm{Ox}}{}^\circ}{9RT})) \quad \textbf{8.21}$$

$$[\mathrm{v}_{\mathrm{La}}^{///}] = 2^{19/9} p\mathrm{O}_2{}^{2/9} \exp(\frac{\Delta S_{\mathrm{S}}{}^\circ}{3R} - \frac{4\Delta S_{\mathrm{AF}}{}^\circ}{3R} + \frac{4\Delta S_{\mathrm{Ox}}{}^\circ}{9R}) \exp(-(\frac{\Delta H_{\mathrm{S}}{}^\circ}{3RT} - \frac{4\Delta H_{\mathrm{AF}}{}^\circ}{3RT} + \frac{4\Delta H_{\mathrm{Ox}}{}^\circ}{9RT})) \quad \textbf{8.22}$$

The corresponding standard entropy and enthalpy values can be found in literature and the defect concentration can be calculated.

Appendix II. List of abbreviations

a	Lattice parameter
A, B	Position of atoms (cations) in compounds with the general formula A_2BO_4 or ABO_3
"A", "B", "C"	Harrison's classification of diffusion kinetics
B, b (index)	Bulk
B	Mechanical mobility (Beweglichkeit)
c	Concentration
C_0	Integration constant
d	Grain diameter, defect
D	Diffusion coefficient
e	Elementary charge
E	Energy, activation energy
F	Driving force, Faraday's constant
g	Atomic site fraction
GB, gb (index)	Grain boundary
G	Gibbs energy
H	Enthalpy
i	Current density
j	Flux density
k_B	Boltzmann constant
k_p	Parabolic rate constant
K	Equilibrium constant
Ln	Lanthanide elements
M	Transition elements
N, n, x	Molar fractions
N_A	Avogadro constant
p	Partial pressure
p	Concentration of electron holes
ppb	Parts per billion
ppm	Parts per million

P	Potential
R	Gas constant
S	Entropy
t	Time, transport number
T	Absolute temperature
u	Charge mobility
v	Migration or drift velocity
v	Vacancy
V_m	Molar volume
w	Grain boundary width
X, x	Thickness
x, y, z	Coordinates
z	Species charge
δ	Non-stoichiometry (hyper or hypo)
γ	Geometry factor
μ	Chemical potential
ν	Vibration frequency
η	Electrochemical potential
φ	Electrical potential
Φ	Thermodynamic factor
σ	Conductivity